
Setup of a UHV System for the Production of Tungsten TES

Dissertation
der Mathematisch-Naturwissenschaftlichen Fakultät
der Eberhard Karls Universität Tübingen
zur Erlangung des Grades eines
Doktors der Naturwissenschaften
(Dr. rer. nat.)

vorgelegt von
Jurek Loebell
aus Hamburg

Tübingen
2016

Gedruckt mit Genehmigung der Mathematisch-Naturwissenschaftlichen Fakultät der
Eberhard Karls Universität Tübingen.

Tag der mündlichen Qualifikation:

20.12.2016

Dekan:

Prof. Dr. Wolfgang Rosenstiel

Berichterstatter 1:

Prof. Dr. Josef Jochum

Berichterstatter 2:

Prof. Dr. Tobias Lachenmaier

Abstract

Humanity has concerned itself with the question of the basic elements of nature over thousands of years. The technological evolution of the last hundred years improved our understanding of the particle nature of matter. However, this is only true for particles, that reveal themselves to us by participating at electromagnetic interactions, or, like neutrinos, are closely related to an electromagnetically interacting partner. Large scale gravitation studies concluded, that these known forms of matter only account for about a sixth of the overall gravitationally interacting matter in the universe. Due to its invisibility to electromagnetic particles, the missing mass is referred to as *dark matter*. While gravitation still remains inaccessible to us on particle scales, technical evolution opened up the field of particle studies based on the weak interaction force, which is a promising field for dark matter studies, since reasonable suspicion exists, that dark matter is also weakly interacting.

Low interaction cross sections and small signals are making particle detection via weak interaction challenging and require sophisticated technology. The CRESST experiment (Cryogenic Rare Event Search with Superconducting Thermometers) and SuperCDMS (Super Cryogenic Dark Matter Search) are aiming to directly detect dark matter particles and investigate their properties by taking advantage of TES (transition edge sensors) to measure the small signals. These TES's are manufactured from thin tungsten films, that are thermally coupled to absorber crystals. To also meet the detection requirements for low interaction rates, a large numbers of detectors, and thus a large numbers of TES are needed.

In order to achieve the required sensitivity, tuning the superconductive properties of the tungsten films is essential. The transition temperature defines the sensitivity range of the TES and the slope of the transition edge their sensitivity. In particular the low superconductive transition of about 15 mK in bulk material makes tungsten the favored material in cryogenic particle detection. However, it is challenging to grow thin tungsten films with such a low transition. The quantum effect of superconductivity is very sensitive to even small changes in the material properties, resulting from varying deposition conditions. Therefore, it is crucial to investigate and understand the influences of differing deposition conditions in order to grow TES of reproducible properties. In thin films especially crystal structure, grain size, impurities and film stress are known to influence superconductivity.

In the framework of this thesis, a production facility for thin tungsten films, that is capable of mass production has successfully been set up. It proved to be capable of producing films with transition temperatures of 15 mK, meeting the requirements of the CRESST experiment. However, due to a lack of reliable transition curve measurements, influences of the deposition conditions on the superconductive properties and their reproducibility could not be investigated. Instead several analysis techniques for investigations of the crystal phase, impurity inclusions, surface morphology, electrical resistance and film stress have been performed. These techniques provide knowledge about film properties, that are known to affect superconductivity. Especially the influence of the substrate temperature during deposition on these film properties were studied. The results of the analysis techniques are specific to the deposition system that has been set up for this work and might differ quantitatively for other deposition systems.

Zusammenfassung

Die Frage nach dem Aufbau der Materie beschäftigt die Menschen schon seit Jahrtausenden. Technologische Fortschritte der letzten hundert Jahre ermöglichen ein immer tiefer gehendes Verständnis des Teilchencharakters von Materie. Allerdings betraf dies ausschließlich Materienteilchen, die direkt oder, wie im Falle des Neutrinos, indirekt über einen elektromagnetischen Partner über den Elektromagnetismus zugänglich sind. Untersuchungen von Gravitationseffekten auf astronomischen Skalen führten zu der Erkenntnis, dass die bekannten, elektromagnetisch zugänglichen Materieformen nur in etwa ein Sechstel der gesamten Masse im Universum ausmachen. Aufgrund der Unsichtbarkeit der unbekannten Materie gegenüber Lichtteilchen wird sie als *Dunkle Materie* bezeichnet. Während Gravitation auf Teilchenebene noch immer unverstanden ist, haben technische Entwicklungen es ermöglicht, Materienteilchen auch über die schwache Wechselwirkung zu studieren. Der begründete Verdacht, dass Dunkle Materie auch an der schwachen Wechselwirkung teilnimmt, macht diese zu einem vielversprechenden Feld für die direkte Detektion Dunkler Materie.

Die kleinen Wechselwirkungsquerschnitte und die kleinen Energieüberträge sind eine große Herausforderung für die Teilchendetektion durch die schwache Wechselwirkung und bedürfen hoch sensitiver Messtechniken. Das CRESST-Experiment (Cryogenic Rare Event Search with Superconducting Thermometers), ebenso wie SuperCDMS (Super Cryogenic Dark Matter Search), versuchen sich an der direkten Detektion Dunkler Materie und der Untersuchung ihrer Teilcheneigenschaften basierend auf Transmission Edge Sensors (TES) zum Nachweis kleinster Energiedepositionen. Die verwendeten TES sind aus dünnen Wolframfilmen gefertigt und thermisch an das eigentliche aktive Detektormaterial – einen Absorberkristall gekoppelt. Um auch den kleinen Wechselwirkungsquerschnitten gerecht zu werden, sind große Stückzahlen von Detektoren und damit auch TES vonnöten.

Um die benötigte Sensitivität zu erreichen ist die Kontrolle der Supraleitungseigenschaften der TES unerlässlich. Sie wird bestimmt durch die Temperatur des Supraleitungsübergangs und seines Anstiegs. Insbesondere die niedrige Sprungtemperatur von etwa 15 mK macht Wolfram zum Material der Wahl für TES Anwendungen und der Dunklen Materie Detektion. Allerdings ist es schwierig solch niedrige Übergangstemperaturen auch in dünnen Wolframfilmen zu erreichen. Der Quanteneffekt Supraleitung ist äußerst sensitiv gegenüber kleinsten Veränderungen der Depositionsbedingungen. Um TES mit gleichbleibenden Eigenschaften herzustellen, ist es daher wichtig die Einflüsse der Depositionsbedingungen zu untersuchen und

zu verstehen. In dünnen Wolframfilmen bestimmen insbesondere die Kristallstruktur, Korngröße, Verunreinigungen und Filmstress beeinflussen bekanntermaßen die Supraleitung.

Im Rahmen dieser Arbeit wurde eine Produktionsanlage für die Massenproduktion von Wolframfilmen aufgebaut und in Betrieb genommen. Mit ihr konnten Supraleitungsübergänge im Bereich von 15 mK realisiert werden, entsprechend der Anforderungen des CRESST-Experiments. Da die Messung von Übergangskurven sehr zeitaufwändig ist, führte ein Mangel an verlässlichen Übergangskurven dazu, dass die Einflüsse der Produktionsbedingungen auf die Supraleitungseigenschaften und deren Reproduzierbarkeit nicht untersucht werden konnten. Stattdessen wurden unterschiedliche Analysemethoden der Kristallstruktur, chemischen Zusammensetzung, Oberflächenmorphologie, elektrischen Leitfähigkeit und des Filmstresses durchgeführt. Mit diesen Techniken lassen sich Filmeigenschaften bestimmen, die bekanntermaßen die Supraleitung beeinflussen. Insbesondere der Einfluss der Substrattemperatur während des Aufdampfens wurde studiert. Die Ergebnisse dieser Analysen sind gekoppelt an die innerhalb dieser Arbeit aufgebaute Aufdampfanlage und können bei anderen Anlagen quantitativ abweichen.

Contents

1	Introduction	1
1.1	Missing Mass on Galactic Scales	1
1.2	Missing Mass on Scales of Galaxy Clusters	3
1.3	Missing Mass on Cosmological Scales	4
1.4	WIMPs	7
1.5	Direct Detection	7
1.6	Cryogenic Particle Detection	9
2	The CRESST Experiment	11
2.1	The Experiment Setup	11
2.2	CRESST-II Detector Modules	13
2.2.1	The Phonon Detector	14
2.2.2	The Light Detector	16
2.2.3	The Phonon-Light Technique	17
2.2.4	Background Discrimination	17
2.2.5	Readout Electronics	19
2.3	Current Status of the CRESST Experiment	20
3	SuperCDMS	23
4	Tungsten Film Properties	25
4.1	General Tungsten Properties	25
4.2	Crystal Phases of Tungsten	26
4.3	Superconductivity in Tungsten Thin Films	28
4.3.1	Phase Composition and Grain Size	28
4.3.2	Magnetic Impurities	29
4.3.3	Film Stress	29
4.4	Film Growth and Microstructure Evolution	32
5	Setup of the Electron Beam Deposition System and Film Production	35
5.1	Requirements on The Film Deposition System	35
5.2	The Ultra High Vacuum System	36
5.3	The Electron Beam Source	37
5.4	The Substrate Holder	38
5.5	Radiation Shielding	42
5.6	Growth Rate Monitoring	45
5.7	The Residual Gas Analyzer	47

5.8	Film Production	49
5.9	Mass Production	51
6	Results on Superconductivity	53
6.1	Results of R(T) Measurements	53
7	Film Analysis	58
7.1	Microstructure Analysis	58
7.1.1	Surface Morphology	58
7.1.2	Crystal Structure Mapping	62
7.1.3	Atomic Composition	64
7.1.4	Microstructure	65
7.1.5	Summary and Interpretation of the Microstructure Analysis	70
7.2	Specific Resistivity	71
7.3	Strain Determination Using X-ray Diffraction	77
7.4	Annealing of Cold Deposited Films	87
8	Summary	89

1 Introduction

Over the last 100 years, physics provided a better and better insight in the particle nature of matter. Today we have a good understanding of how particles interact in the strong, the weak and the electromagnetic interaction. However, how matter interacts gravitationally on particle scales remained in the dark. Comparing gravitational and electromagnetic interaction of a proton and an electron reveals a difference in strength of a factor 10^{39} , making it impossible to study gravitation on particle scales. Only for big masses composed of baryonic matter, where electromagnetism plays a minor role, gravitation reveals itself to us.

In 1933 Fritz Zwicky applied the virial theorem to a cluster of galaxies and discovered that the luminous matter could not account for the total mass of the cluster [1]. He introduced the term *dark matter* for the invisible, because not electromagnetically interacting mass. Later observations on different astronomical scales confirmed the existence of dark matter. Some of these observations, that are exemplary for three different length scales, will be discussed in this chapter. Moreover, Weakly Interacting Massive Particles as possible dark matter particle candidates will be introduced as well as a general direct dark matter detection method.

1.1 Missing Mass on Galactic Scales

One of the most striking arguments for the occurrence of dark matter on galactic scales is derived from radial velocity distributions in galaxies. Due to Newtonian dynamics, stars and dust in spiral galaxies were assumed to rotate with a radial velocity, that increases from the galactic center to the edge of the visible disc, and drops for even bigger radii, following the Keplerian law

$$v(r) = \sqrt{G \frac{M(r)}{r}}. \quad (1.1)$$

Redshift measurements of the 21 cm hydrogen line revealed that the velocity versus radius curves do not exhibit such a drop off at the edge of the visible disc, but show a rather flat behavior (see figure 1.1). Since the radial mass distribution was derived from the mass-to-light ratio [2], e.g. strong dust absorption in the outer regions [3], a vast amount of exotic, non-luminous stars [4] and “*new dynamical considerations*” [5] were suggested to be the cause. Only in the 1979’s the observed

1.1 Missing Mass on Galactic Scales

anomalies were brought into context with a possible unknown non-luminous kind of matter. Originally galaxies form from clouds of hydrogen and helium that collapse in a manner that conserves angular momentum, forming a disc like structure. The collapse is due to the gravitational force and the fact, that baryonic matter can loose energy via radiation. Without the ability of electromagnetic interaction, dark matter can not collapse that easily and is therefore assumed to enclose the galaxy in a huge halo, that, in agreement with the rotation curve data, extends far beyond the edges of the luminous disc.

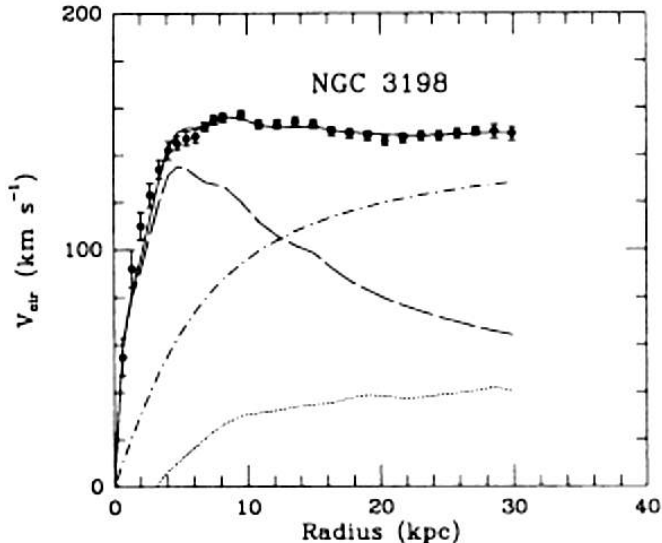


Figure 1.1: Rotation curve of the galaxy NGC 3198. The stellar component (dashed line) and the galactic gas (dotted line) alone can not account for the mass needed to explain the flat behavior of the rotation curve in a scenario of Newtonian dynamics. The dash dotted line shows the contribution of a possible dark matter halo that could explain the data [6].

A second, still pursued attempt to account for the flat behavior in radiation curves is to consider modified Newtonian dynamics, also referred to as the MoND theory [7]. It introduces a scaling factor to the second Newtonian law, that adapts the theory to the measured data without assuming a dark matter halo

$$\mathbf{F} = m \cdot \mu(a/a_0) \cdot \mathbf{a}. \quad (1.2)$$

For $a \gg a_0$ the unspecified function μ takes on a value of ~ 1 maintaining the Newtonian law, whereas for $a \ll a_0$ μ becomes a/a_0 , weakening the gravitational force for small accelerations. Although the MoND theory can explain rotation curves, like Newtonian gravitation it has a limited scope, as we will see in the next section.

1.2 Missing Mass on Scales of Galaxy Clusters

Unlike Newtonian dynamics general relativity describes not only the interaction between masses, but also gravitational effects on massless particles like photons. In general relativity, gravitation is caused by concentrations of mass that bend space-time and deflect the paths of light. Therefore, high mass astronomical objects can have a focussing effect on light, similar to glass lenses. The degree of deflection particularly depends on the mass concentration, enabling a mathematical reconstruction of mass distributions after observation of gravitational lensing.

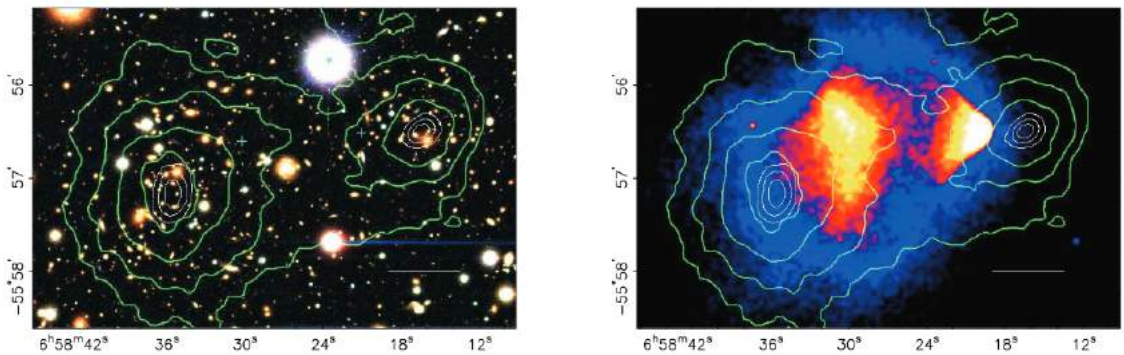


Figure 1.2: The merging cluster 1E 0657-558 in visible light (left) and X-rays (right). The green contours are equipotential lines, determined by weak gravitational lensing. The white contours encircle the centers of mass with one, two and three sigma confidence level. The plus signs mark the centers of mass of the hot gas component. The white bar indicates a length scale of 200 kpc [8].

Figure 1.2 shows the combined observations in visible light (Hubble Space Telescope), X-rays (Chandra) and derived from gravitational lensing of the so called bullet cluster. It is the observation of two galaxy clusters, that ran into each other about 100 million years ago. Both consist of galaxies and a hot plasma component, visible in the X-ray regime. The stars within the two clusters passed each other, showing no sign of interaction, whereas after the collision, the plasma seems to have fallen behind, trailing after the stellar components, due to interactions between the two plasma clouds. As the equipotential lines indicate, the centers of mass do not coincide with the gas clouds, but with the stellar components. However, Clowe et al. [8] reported a mass ratio that strongly favors a big plasma component. To bring these two facts in agreement, a third so far unknown matter component is needed, that spatially coincides with the galaxy clusters. The MoND theory does not provide any satisfactory explanation to this observations, while excluding dark matter.

1.3 Missing Mass on Cosmological Scales

One of the major accomplishments of the big bang theory was the prediction of the cosmic microwave background (CMB). It formed when baryonic matter went through the transition from plasma to gas, due to expansion cooling of the universe. A plasma has a continuous perfect black body emission spectrum, but at the time of the transformation into gas, it turned to a characteristic spectrum, so the gas stopped interacting with photons, that didn't match its emission lines. These photons that decoupled from matter interactions became free to travel through the universe and can be detected today as black body spectrum of a temperature corresponding to the temperature of decoupling at ~ 3000 K, multiplied by roughly 10^{-3} to account for expansion red shift. Since the decoupling happened everywhere, the CMB is filling the universe uniformly. Small angular temperature fluctuations are caused by oscillations of local densities that were caused by the counter play of gravitational contraction power and the out driving radiation pressure of photons. The fluctuations are often referred to as "seeds" of structure formation, since gravitation leads to an exponential density growth. Therefore, the map of the CMB is essential for the understanding of structure formation in the early universe and is probably the most informative measurement in cosmology until today.

CMB radiation was detected for the first time rather coincidentally in 1969 by Arno Penzias and Robert Wilson with a ground based microwave antenna [9]. Later measurements at different wave lengths confirmed the black body shape of the spectrum [10].

Satellite and balloon missions from the late 1980's on revealed a more and more precise picture of temperature fluctuations on small angles. The most recent data were published by the Planck satellite collaboration. The all sky temperature map is shown in figure 1.3. The warmer red regions are related to relative over densities of about 10^{-5} whereas the cooler spots shown in blue represent regions of densities below average. The anisotropies are usually written as spherical harmonic expansion

$$\frac{\delta T}{T}(\vartheta, \varphi) = \sum_{l=2}^{\infty} \sum_{m=-l}^{+l} a_{lm} Y_{lm}(\vartheta, \varphi) \quad (1.3)$$

The variance C_l of the amplitudes a_{lm} is given by

$$C_l = \langle |a_{lm}|^2 \rangle = \frac{1}{2l+1} \sum_{m=-l}^l |a_{lm}|^2 \quad (1.4)$$

The information contained by 1.3 is compressed into this so called power spectrum C_l . As in figure 1.4, usually plotted is $l(l+1)C_l/2\pi$. The cosmological model that can account best for this data is the Λ CDM model, that is often referred to as standard model of cosmology. It is based on the assumption of the universe being born in a big bang and describes its evolution under the impact of an accelerating expansion driven by dark energy, represented by the cosmological constant Λ and the influence of cold dark matter (CDM). Six of its parameters are free and can be used to adapt the model to the observations. The best fit to the latest data of the CMB suggests an energy share of 68.3 % dark energy, 4.9 % baryonic matter and a dark matter contribution of 26.7 % [11].

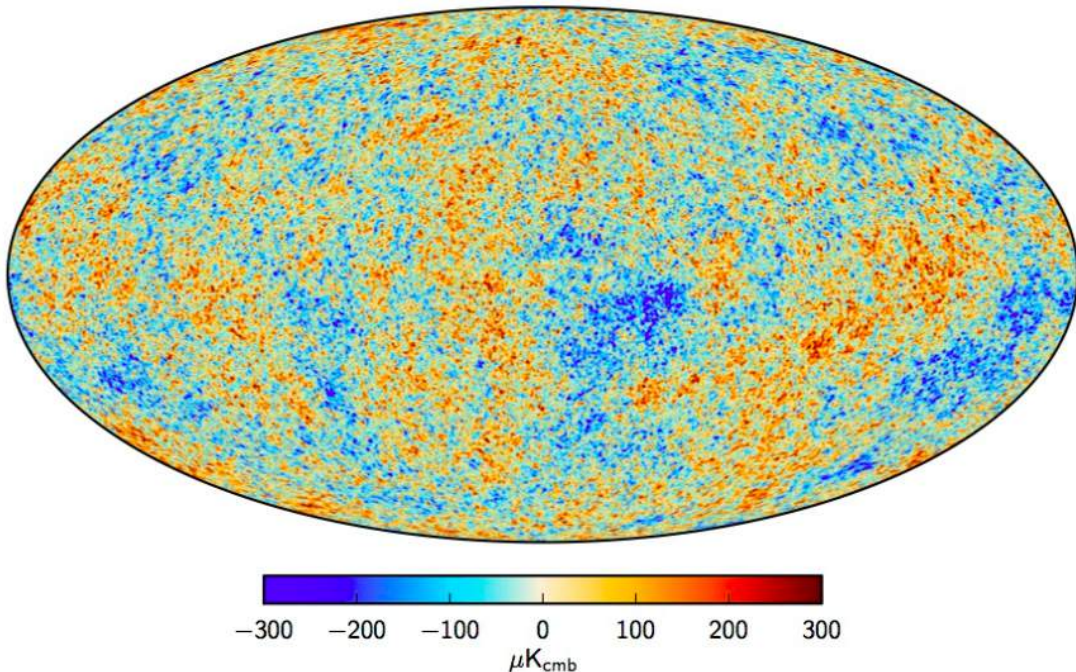


Figure 1.3: The Planck CMB all sky map of 2015. The temperature map directly correlates to the matter density distribution at the time of photon decoupling about 380,000 years after the big bang [12].

Summarizing it has to be pointed out that multiple observations of missing mass on different scales strongly suggest the existence of a non-electromagnetically interacting unknown kind of matter. However, there is no gravitational process known that could lead to the formation of matter. Collider experiments like the large hadron collider (LHC) also rule out strong interaction. So if the assumption of the universe being born in a big bang is right, dark matter necessarily has to interact weakly or via a fifth, yet unknown force, that can account for its formation. A look in the standard model of physics shows, we indeed already know of a massive particle, which is neither electromagnetically nor strongly interacting.

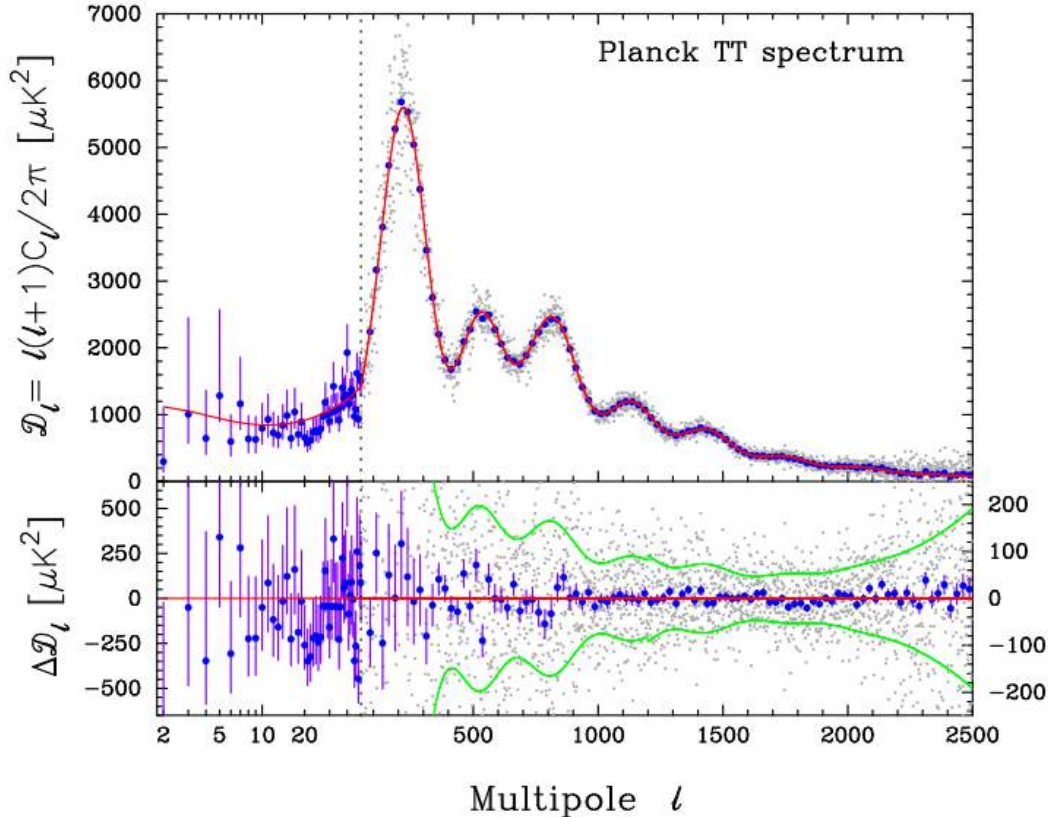


Figure 1.4: The Planck CMB power spectrum of 2013. The grey dots are the actual data points, whereas the blue dots with the error bars represent the data after a binning of $\Delta l \approx 31$. The data left of the grey dotted vertical line are shown with a different multipole scale. The power spectrum is fitted with the minimal Λ CDM model (red). In the lower panel the discrepancy of data and model is shown, together with the one sigma standard deviation (green) [11].

Neutrinos were long suspected to be responsible for the missing mass, but constraints on their mass, combined with observations on structure formation contradict this hypothesis. Like photons, neutrinos were also in thermal equilibrium with the primordial plasma until their time of decoupling. Because of their small mass, neutrinos must have been very hot at the beginning of structure formation and would have washed out small scale structures, leading to a top-down scenario in structure formation. However, since a bottom-up scenario favoring cold dark matter is seen as proven, neutrinos can only account for a small amount of the missing mass.

1.4 WIMPs

Weakly interacting massive particles (WIMPs) are among the most promising dark matter candidates. In particular, supersymmetric (SUSY) theories provide a field for postulations of new particles. Symmetries form the most fundamental level for our understanding of nature. The explanations for whether symmetries are broken or perfectly valid are beyond grasp until today. SUSY is the attempt to put the highly non-symmetrical relation between fermions and bosons in a bigger, symmetrical context. It assigns a bosonic partner to every fermion and vice versa, providing a wide field of free parameters, that can be adapted to observations and thereby explain phenomena like the missing mass problem. Most SUSY theories introduce a conserved multiplicative quantum number, the R-parity, ensuring that SUSY particles in interaction processes only show up in pairs. This way, the conservation of R-parity hinders the lightest SUSY particle (LSP) from decaying, making it a possible dark matter candidate. If the mass of the LSP particle is in the GeV to TeV range, it could be a main contribution to the missing mass.

1.5 Direct Detection

Generally speaking, there are three different approaches for the detection of WIMPs.

Particle accelerators are searching for signatures of WIMPs, created in particle-antiparticle reactions. The collision of energetic particles generates high energy densities, very like at the big bang, but in a much smaller scale. If dark matter has been born in the big bang and the energy of the accelerated particles is high enough, these particle collisions should hold the potential to also generate individual dark matter particles. The dark matter particles would leave the detectors unnoticed, due to their small interaction probability, but would reveal themselves to us by carrying away energy and momentum.

In the case of the WIMP being its own antiparticle, a characteristic signature could be detected in astronomical observations. Especially in the centers of galaxies, where the dark matter density is assumed to be high, annihilation of WIMPs could lead to an excess of particle-antiparticle pairs or high energy photons in the energy range corresponding to the WIMP mass. Also massive objects like the sun, where WIMPs of low energy could be gravitationally trapped, are of interest.

Direct WIMP detection mechanisms are based on elastic WIMP nucleus scattering. Dark matter particle flux and interaction cross section determine the expected interaction rate. For experimentalists especially the interaction rate per target mass is of interest.

$$R = \frac{\phi\sigma}{m_T} \quad (1.5)$$

$\phi = n_\chi v_\chi = \frac{\rho_\chi}{m_\chi} v_\chi$ = WIMP flux
 m_χ = WIMP mass
 n_χ = WIMP number density
 ρ_χ = local WIMP density
 σ = WIMP nucleus scattering cross section
 v_χ = WIMP velocity
 m_T = mass of target nucleus

The local dark matter density can be derived from observations of rotation curves in the milky way [13] and is reported to be $\sim 0.3 \text{ GeV/cm}^3$. For WIMP velocities in the galactic halo, usually a Maxwell-Boltzmann distribution is applied, justified by the assumption of thermalization due to “violent relaxation” [14] and dynamical friction [15]. The Maxwell distribution is assumed to be cut off at the galactic escape velocity of $v_{esc} = 544 \text{ km/s}$ and to peak in the solar system at a velocity comparable to the circular velocity of the sun $v_0 \approx 220 \text{ km/s}$, leading to $\langle v \rangle = \sqrt{\frac{3}{2}}v_0 \approx 270 \text{ km/s}$. With a typical weak interaction cross section, tungsten as target mass and a WIMP mass of 100 GeV, the rate can be estimated to a few events per kilogram target mass and year. The count rate expected from natural radio activity and cosmic rays is much higher. Therefore, active background discrimination and shielding is required. Also challenging are the small energies, deposited by WIMP nucleus recoils

$$E_r = E_\chi \frac{2\mu^2}{m_\chi m_T} (1 - \cos\vartheta) \quad (1.6)$$

E_χ = WIMP energy
 $\mu = \frac{m_\chi m_T}{m_\chi + m_T}$ = reduced mass
 ϑ = scattering angle

Assuming comparable masses $m_\chi \approx m_T$ of 100 GeV and a WIMP energy corresponding to $\langle v \rangle \approx 270 \text{ km/s}$, E_r can take on values between 0 and 50 keV. The Maxwellian velocity distribution results in an exponential recoil energy spectrum. This is also a typical behavior for background induced events.

Since the transferred energies are small ($\sim 10 \text{ keV}$), coherent WIMP-nucleus scattering is assumed, yielding $\sigma \propto A^2$ for spin-independent scattering. However, for higher momentum transfer the WIMPs could start to resolve the target nuclei and a form factor has to be introduced. Furthermore, the cross section is different for possible spin-dependent interactions.

The characteristics of WIMP nucleus interactions define the detector requirements. The small event rate requires the detectors to be run in underground laboratories. The overburden reduces the flux of electromagnetically interacting cosmic ray particles. Additionally, natural radioactivity from particle decays in the rock needs to be shielded with high purity materials. The assumed Maxwellian velocity distribution results in the expectation of a background like energy spectrum. To be able to distinguish between background induced particle events and that of WIMPs, most direct detection experiments introduced active background discrimination by reading out the deposited energy in two channels. Electrons and photons will mostly interact with the electronic system of the target mass, in general resulting in more scintillation light or ionization, contrary to particles, that interact with the target nuclei. Reading out the deposited energy via both, phonons and scintillation light provides an event-by-event background discrimination. Since the expected energy depositions are very small, of the order of 10 keV, an extremely sensitive detection mechanism is required. Often the technique of choice is to use transition edge sensors (TES) for energy deposition measurements at cryogenic temperatures. The proportionality $\sigma \propto A^2$ for coherent spin-independent scattering enables to investigate certain properties, like mass and coupling of a possibly detected WIMP with several targets. Such a multi target approach is currently only realized by the CRESST experiment.

1.6 Cryogenic Particle Detection

As described in section 1.5, energy depositions in WIMP nucleus scattering are very small (~ 10 keV), making detection challenging. Most energy detection techniques measure only part of the deposited energy, like e.g. ionization detectors. In ionization detectors the signal has to be read out quickly, before it decays into other, undetectable channels and to create uniform conditions across the whole active detector volume. But even if this is perfectly solved, fluctuations of the energy branching between different channels limit the energy resolution. Due to statistical reasons, every process of energy conversion produces heat. A back conversion of heat into other forms of energy is only possible with low efficiency, making heat a favored channel in energy conversion chains. Calorimetric detectors take advantage of this fact. The most simple calorimeter module would be an absorber equipped with a thermometer, which again is weakly coupled to a heat sink. This basic setup is sketched in figure 1.5.

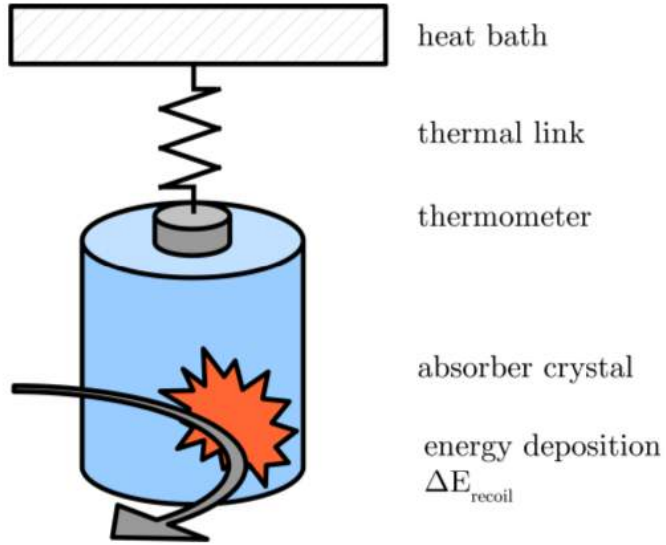


Figure 1.5: A simple calorimeter module. The deposited energy can only escape through the heat link [16].

Energy thermalizing in the absorber will cause a rise in temperature, given by

$$\Delta T = \frac{\Delta E}{C} \quad (1.7)$$

with C as the absorber's heat capacity. In the case of a dielectric crystal, held well below the Debye temperature, contributions to the specific heat capacity are only due to the phononic system and can be calculated as

$$c = \frac{12\pi^4}{5} n k_B \left(\frac{T}{\Theta_D} \right)^3 \quad (1.8)$$

The proportionality of $c \propto T^3$ favors cryogenic temperatures for the detection of small energies. Depending on the coupling of the thermometer to the heat bath, such a detector can be operated in a calorimetric or in a bolometric mode. The heat coupling for the calorimetric mode is small, so the thermometer is in thermal equilibrium with the absorber, whereas in the bolometric mode the heat flow through the thermometer is measured.

2 The CRESST Experiment

This chapter is addressed to the setup of the CRESST experiment (Cryogenic Rare Event Search with Superconducting Thermometers). It will explain the fundamental measuring technique, since this thesis has been done in the framework of this experiment.

2.1 The Experiment Setup

The CRESST experiment is dedicated to the direct search for WIMP like dark matter via coherent scattering on target nuclei. CRESST is situated in an underground laboratory, the LNGS (Laboratori Nazionali del Gran Sasso) of the INFN (Istituto Nazionali di Fisica Nucleare) in the Italian Abruzzo region. Covered by 1400 m of rock overburden, corresponding to 3500 m of water equivalent, it provides a reduction of the cosmic muon flux by about a factor of 360000 to about one muon per square meter and hour [17].

The detectors are run at milli Kelvin temperatures, provided by a ^3He dilution refrigerator. The general setup of the experiment is sketched in figure 2.1. Since the materials deployed in the commercially available cryostat (CR) do not necessarily meet the high radiopurity requirements of the detectors, any line of sight of the cryostat to the detectors is avoided by means of a coldfinger (CF). The detectors are mounted on a carousel (CA) like high purity oxygen free copper structure at the end of the coldfinger. It is capable of housing up to 33 detector modules. The coldbox that houses the carousel consists of five nested thermal radiation shields. Several layers of different materials surrounding the coldbox block, reduce or veto the flux of unwanted particles. The outmost layer is a polyethylene shield (PE), that moderates or blocks incident neutrons. Going inwards, the next layer is an active muon veto (MV), consisting of plastic scintillator. It surrounds a radon box (RB), that is constantly flushed with nitrogen gas, in order to displace radon contaminated air. γ 's are being blocked by a layer of low activity lead (PB) and high purity copper (CU) that again blocks the remaining radioactivity of the lead. The innermost shield inside the coldbox, not shown in the sketch, is again a polyethylene shield for further reduction of the neutron flux. To decouple the cryostat from external vibrations that could heat up the detectors, the whole cryostat along with the shieldings are put on air dampers. Vibrations caused by boiling nitrogen inside the cryostat could have the same effect. Therefore, the carousel rests on metal springs.

2.1 The Experiment Setup

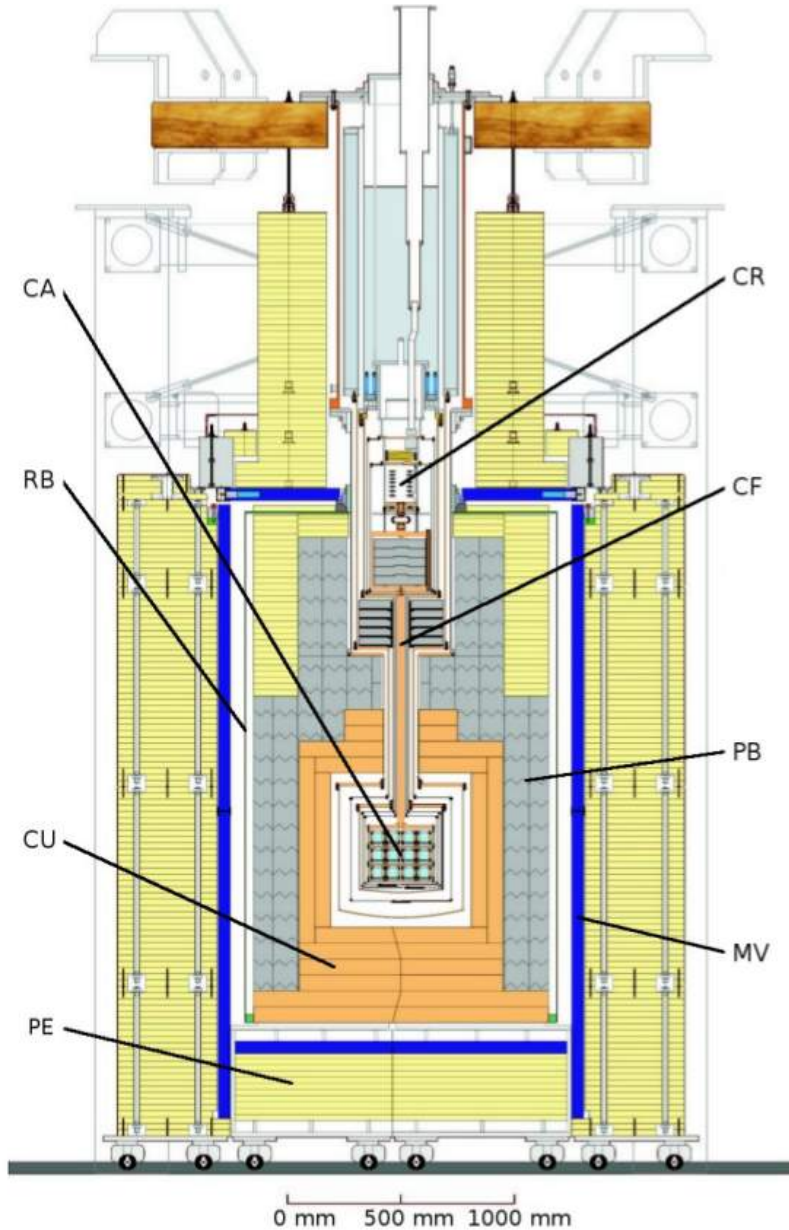


Figure 2.1: Sketch of the CRESST II experiment setup. The detector modules are situated in the carousel like structure (CA) at the end of the coldfinger (CF) and are cooled to milli Kelvin temperatures by the dilution refrigerator (CR). In order to reduce the flux of unwanted particles, a nitrogen flushed radon box (RB) as well as layers of polyethylene (PE), high purity copper (CU) and low activity lead (PB) surround the carousel. An additional muon veto (MV) allows an active reduction of the muon background [18].

2.2 CRESST-II Detector Modules

As detectors, CRESST is using cryogenic calorimetric modules with an additional readout channel for light. Currently, there are several designs in use with slightly different geometrical concepts of background suppression. However, the detection mechanisms are the same. In figure 2.2 one of the different designs is shown. It consists of an absorber crystal for phonon detection and an absorber disc for light detection, each equipped with an individual thermometer.

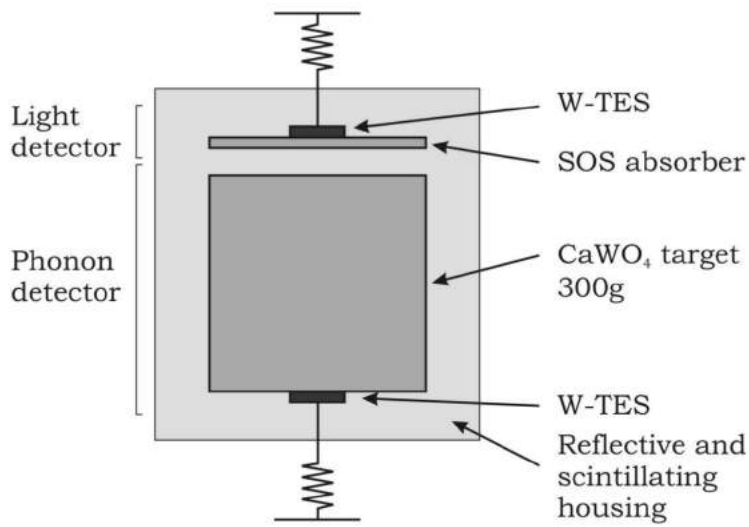


Figure 2.2: Example of a CRESST detector module. Incident particles in the target crystal will generate phonons and photons. While the phonons will heat up the tungsten TES and lead to a measurable signal, the photons are first converted into phonons inside the absorber disc and then detected by the TES of the light channel. The highly scintillating and reflective foil improves the light collection and vetos surface events by additional light generated in the foil [19].

The absorber crystal is a $\sim 300\text{ g}$ single crystal of calcium tungstate (CaWO_4), a material that contains nuclei of three different masses, and therefore of three different interaction cross sections for coherent scattering on nuclei for a given dark matter particle mass. The thermometer is realized by transition edge sensors (TES), that take advantage of the strongly temperature dependent resistance of metal films at their superconductive transition (see figure 2.3). For TES stabilized in their transition edge, a small change in temperature will cause a comparably large change in resistance. The development of superconducting readout technology made them a powerful tool in particle detection. The TES used in CRESST are made from 200 nm thick tungsten films. With 15 mK (see also section 4) tungsten has the lowest superconductive transition of all elementary metals, enabling to measure

with low heat capacities and therefore high sensitivity. The light absorber is a circular sapphire disc, of 40 mm diameter and 460 μm thickness, coated with a 1 μm silicon layer on one side for better light absorption.

About the energy conversion of particle events into phonons and the pulse shape formation in the TES, a detailed model has been developed in [20]. The following section will give a brief overview.

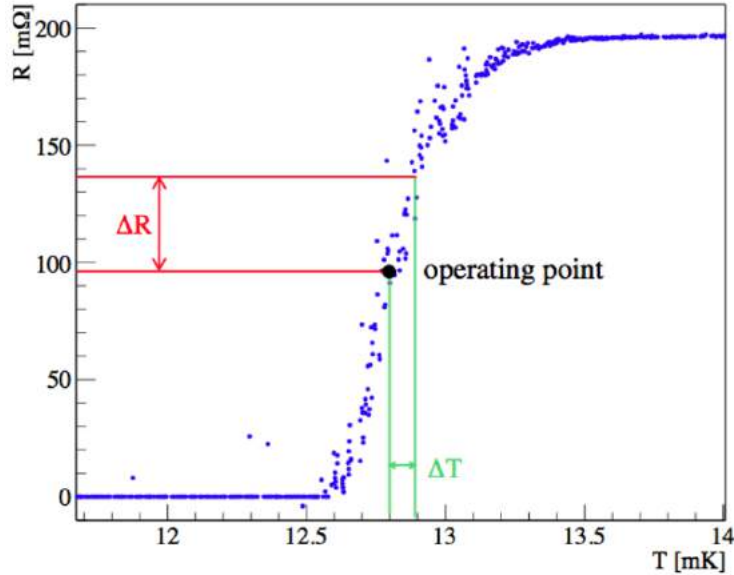


Figure 2.3: Typical example of a tungsten transition curve. If stabilized in the linear part of the transition edge, a small change in temperature (ΔT) will create a proportional and measurable change in resistance (ΔR) [21].

2.2.1 The Phonon Detector

The thermodynamic model of a CRESST phonon detector shown in figure 2.4 consists of four components. The heat bath, the phononic system of the absorber crystal as well as the phononic and the electronic system of the TES. The heat link between the absorber and the heat bath G_{ab} can not be avoided, because the crystal has to be held somehow, but it is minimized by the usage of thermally insulating materials. For the coupling between phonons and electrons in the TES a fifth power temperature dependence can be assumed [20], so at low temperatures both systems are largely decoupled. The conductance between two phononic systems is characterized by the elastic properties of both materials. The resulting Kapitza conductance in

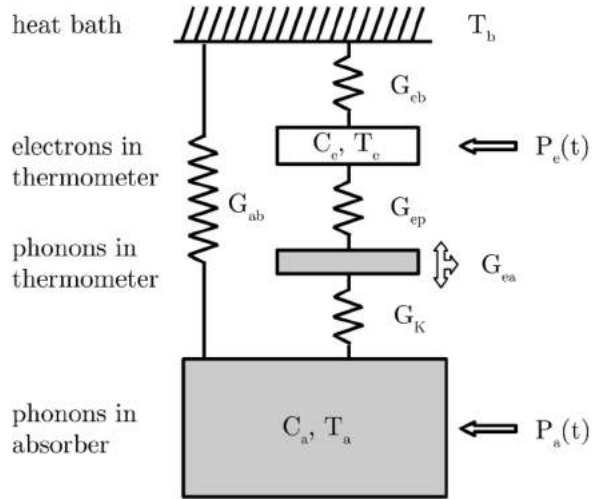


Figure 2.4: Thermodynamic model of a CRESST phonon detector as in [20]. C_a and $P_a(t)$, as well as C_e and $P_e(t)$ stand for the heat capacities of – and the respective power input into – the absorber and the electronic system of the TES. The indexed T 's denote the temperatures of the different components and G_{ab} , G_{eb} , G_{ea} , G_{ep} and G_K the thermal conductances across the heat links. Image credit Christof Sailer [16].

this case shows a $\propto T^3$ dependency. Since the heat capacity of the phonons in the film is negligible at cryogenic temperatures, the resulting heat coupling between the electrons in the TES and the phonons in the absorber can be expressed as

$$G_{ea} = \left(\frac{1}{G_K} + \frac{1}{G_{ep}} \right)^{-1} \quad (2.1)$$

The thermal conductance of the TES electrons to the heat bath G_{eb} is determined by the thermal conductance of the heat link itself and that across the film. Apart from specific material properties of absorber and film, G_{ea} and G_{eb} define if the detector operates in calorimetric or bolometric mode. The CRESST phonon detectors have a strong coupling to the heat bath and thus work as bolometers, whereas the light detectors are calorimeters.

Considering a particle interaction in the absorber crystal, distinction must be made between two processes.

In the case of an ionizing particle interaction, the energy will initially be deposited in the electric system of the absorber crystal by excitations of electrons, which then will generate electron-hole pairs, until the particle energy falls below two times the energy gap of the absorber. Electron-hole recombination then causes a small fraction of photons, but mainly optical phonons, that again decay into phonons of about half the Debye frequency ν_D . With the Debye temperature of ~ 250 K [22] for CaWO₄, ν_D calculates to $\nu_D = k_B\Theta_D/h \approx 4$ THz.

Nuclear recoils, however, result in a continuous spectrum of acoustic phonons up to ν_D .

Thermal phonons at typical operation temperatures of about 10 mK would have frequencies of $k_B T / h = \nu_{th} \approx 200 \text{ MHz}$. Therefore, the initial THz phonons are referred to as non-thermal. Due to lattice anharmonicity these phonons decay with a strongly frequency dependent rate $\Gamma \propto \nu^5$ within few milli seconds in respectively two phonons, until they reach a frequency of about 300 GHz, filling the crystal uniformly. By then all differences in the phonon spectra of originally electron and respectively nucleon interactions are washed out and only the amount of generated light can be used for distinction.

Phonons that hit the thermometer are absorbed efficiently by the free electrons of the film. This energy is then quickly thermalized due to the strong coupling of electrons among each other, causing the temperature of the TES and therefore its resistance to rise. The power input by the non-thermal phonons in the thermometer results in an exponentially decaying fast signal component. Part of this power escapes via the link to the thermal bath, while the remaining fraction is radiated back into the absorber, where it thermalizes, inducing a slow signal component.

2.2.2 The Light Detector

The particle detection mechanism of the light detector is the same as for the phonon detector. However, the TES is adapted to the even smaller energy depositions. The temperature rise in the TES at a particle detection is determined by the deposited energy and the heat capacity of the electrons in the film. For a given material with a certain T_c , the heat capacity of a film can only be decreased by reducing the size of the TES, causing the active area and therefore the number of phonons that hit the TES to drop. To gain a smaller heat capacity without having to reduce the phonon collection area, phonon collectors were introduced into the design of the light detectors. The tungsten film is reduced in size, maintaining the thickness of 200 nm, and two aluminum pads overlap the tungsten film on two opposite ends. Aluminum becomes superconducting at 1.14 K. Therefore, its heat capacity is negligible at typical operation temperatures. Phonons that hit the aluminum layers will create quasi particles, that are down converted in energy by creating more quasi particles, until they have an energy of less than two times the superconductivity energy gap. Since the proximity effect (see also chapter 4) causes a gradient of the energy gap that drops towards the tungsten film, the quasi particles drift into the TES, where they are detected. The weak thermal coupling of the TES to the heat bath enables to measure photon energy depositions down to $\sim 10 \text{ eV}$.

2.2.3 The Phonon-Light Technique

Both, the target crystal and the light detector are located in a highly reflective and scintillating housing, consisting of a polymeric foil, supported by a high purity copper structure. A main advantage of CRESST in the field of experiments dedicated to the direct dark matter detection is the exchangability of the target material. Varying interaction cross sections enable scanning of the dark matter parameter space. The most important requirement for the target crystal is the light output. Nearly every dielectric material becomes scintillating at low temperatures, but only few have a sufficient transparency, which is vital for the readout of the light channel. Particles that interact in the crystal typically deposit energy mainly in form of heat and only a few percent of the deposited energy is being converted into light. The light output depends strongly on the type of interaction. Interactions with the electronic system cause an enhanced amount of light compared to nuclear interactions, allowing an event-by-event active background suppression. Furthermore, the light signal can be used to distinguish between nuclear recoils on the three different target materials within the crystal. To do so, the *light yield* is defined as the ratio of the detected energy in the light detector and the measured energy in the phonon detector. The scale of the light yield is normalized by defining the light yield to be 1 for γ - and electron interactions. This calibration has been done with the photons of a 122 keV ^{57}Co source. The reduction of the light yield for α particles and nuclear recoils will from now on be referred to as *quenching factor*. Energy depositions by α particles and nuclear recoils on oxygen, calcium and tungsten differ, resulting in a band structure for particle interaction events in light yield versus phonon energy scattering plots. Figure 2.5 shows such a scatter plot from the previous run of the CRESST experiment. The majority of the events is caused by electron interactions and therefore gather around a light yield of 1. The black line marks the boundary below which only 0.1 % of the events are expected. The α (yellow), oxygen (purple) and tungsten (grey) recoil bands are separated at higher energies, but overlap in the region of interest (orange). The calcium band is left out for more clarity. The region colored in blue indicates the overlap free region of the α band.

2.2.4 Background Discrimination

Besides the dominating γ and electron events that leak down in the nuclear recoil bands at low energies, there are other types of background. Due to the proportionality of the nuclear recoil interaction cross section to the square of the nuclear mass ($\sigma \sim A^2$), neutrons preferably scatter on light elements and thus show up in the oxygen band. Another source of unwanted events are ^{210}Po decays. ^{210}Po is an isotope in the uranium-radium natural decay chain. It is hard to control ^{210}Po contaminations in the direct detector vicinity, since it is a decay product of ^{222}Rn ,

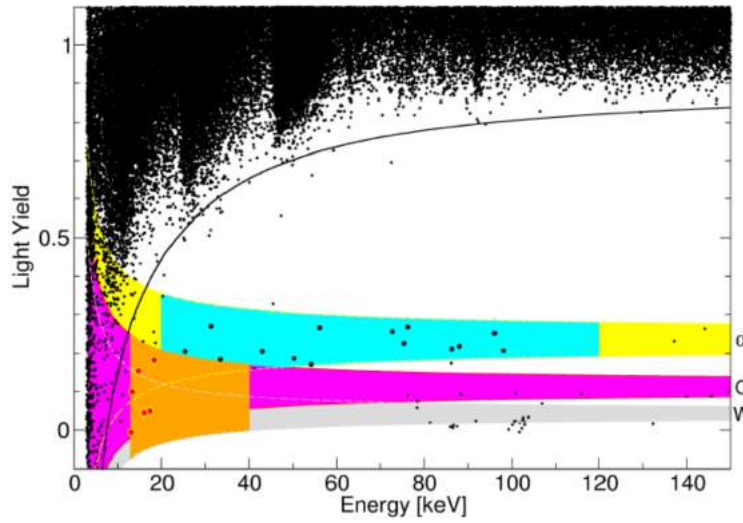


Figure 2.5: Scatter plot of a CRESST detector. The majority of events is due to electron and γ interactions in the crystal’s electronic system. Below the black line only 0.1 % of the electron and γ events are expected. The leakage of energy degraded α events from the yellow α band into the region of interest (orange) can be estimated using the overlap free α band (blue). The events in the violet oxygen band are caused by neutrons. Lead nuclei show up in the grey tungsten band, trailing downwards to low energies starting from their initial energy of 103 keV (see also section 2.2.4) [19].

a gas that diffuses through rock and accumulates in underground cavities like the LNGS underground laboratory. ^{210}Po follows the decay equation



Both, the α particle and the ^{206}Pb nucleus, that experiences a recoil can show up in the scattering plot. The α particle events can trail down towards the region of interest in the α band due to energy degradation. Assuming the ^{210}Po nucleus to be at rest at the time of decay, the ^{206}Pb nucleus will have an energy of 103 keV. The overall deposited energy of a ^{210}Po decay depends on the geometry of the decay process. Figure 2.6 illustrates the two possible cases where the mother nucleus is being ejected towards the target crystal. If the ^{210}Po was implanted in the crystal surface, 103 keV of energy will be deposited, plus a fraction of the α energy. These events are energetically far from the region of interest and would also be vetoed by the α particle that generates scintillation light in either the crystal or the surrounding foil. ^{210}Po implantations in the foil are more critical. If the lead nucleus is being recoiled towards the crystal, it can suffer an energy loss in the foil and hit the target crystal with degraded energy and could leak down in the tungsten band towards the region of interest. Also this event should be vetoed by additional light generated by the α particle and lifted up into the α band. However, this is not the case, if the α

particle hits the only non-scintillating areas, represented by the bronze clamps that hold the crystal. In this case it will stay unnoticed and the energy degraded ^{206}Pb nucleus mimics a WIMP recoil. Figure 2.5 shows all these events. The neutrons in the oxygen band, energy degraded α 's in the α band, down trailing ^{206}Pb events in the tungsten and α band as well as the γ and electron background.

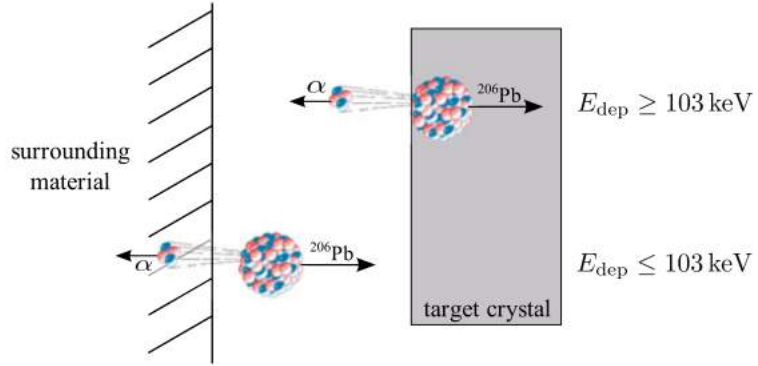


Figure 2.6: Two possible decay scenarios of ^{210}Po , which is slightly implanted into – or situated on surfaces in the detector. Note, that a fully scintillating detector housing would be able of vetoing all this events, that otherwise could mimic WIMPs [19].

2.2.5 Readout Electronics

The front end readout circuit for the TES is shown in figure 2.7. It is biased with a constant current of typically $\sim 10\ \mu\text{A}$. The current then divides according to the resistances of the TES of typically $\sim 100\ \text{m}\Omega$ at the operation point and that of the two shunt resistors R , that account for $20\ \text{m}\Omega$ each. A change in the TES resistance changes the branching of the current and thus the magnetic flux in the input coil L_{in} , that couples into the SQUID (Superconductive Quantum Interference Device). The SQUID is operated in a flux-locked-loop, meaning that a second coil, called feedback coil in a SQUID control circuit compensates the flux of L_{in} in the SQUID. The voltage across a SQUID varies periodically with every flux quantum, that couples into the SQUID. Measuring instead the current at the feedback coil results in a wide linearized range of the output signal.

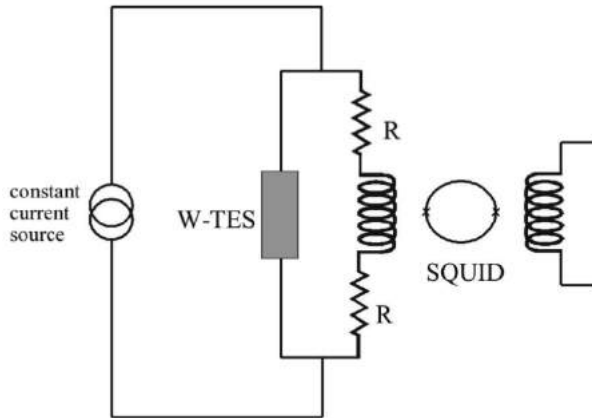


Figure 2.7: Readout circuit for a TES as used in CRESST. The current branches according to the resistances of the TES and the shunt resistors. A change in the TES resistivity will thus change the magnetic flux coupled from the left coil into the SQUID. The feedback coil (right) then compensates the flux through the SQUID and the required current is a measure for the TES resistance [18].

2.3 Current Status of the CRESST Experiment

The results of direct WIMP detection experiments are usually presented in a mass versus cross section plane, since neither mass nor cross section are known. Figure 2.8 shows results of the CRESST-II phase-1 and phase-2 run, as well as an outlook into the near future of CRESST (CRESST-III). The solid red line denotes the 90 % confidence level exclusion limit, yielded by the TUM40 detector with an exposure of 29 kg-days [23]. The shaded region at the lower edge marks, where WIMP nucleus scattering experiments will run into the background of neutrino coherent scattering on target nuclei [24]. The data taken during the CRESST-II phase-1 were analyzed in a maximum likelihood analysis, taking all the background sources described in the previous section into account [19]. However, they couldn't account for all events in the region of interest. Including a possible WIMP in the maximum likelihood analysis, resulted in the two WIMP likelihood maxima M1 and M2 with significances of 1σ and 2σ , shown in figure 2.8 as colored regions in turquoise and green. Kuźniak et al. suggested these additional events to originate from nuclei, sputtered from the clamps by ^{210}Po decays [25]. In the current run detector modules where deployed that try to eliminate this background, by preventing any line of sight from the target crystals to the bronze clamps. As can be seen from the data shown in figure 2.9, at least one of the modules was able to do so [23]. Also the neutron background has been reduced by introducing an additional polyethylene shield inside the coldbox of the cryostat (see section 2.1). The TUM40 detector module is the working horse of the ongoing run. It was not only able to exclude the upper WIMP likelihood

maximum, it also enabled a lower energy threshold of only 600 eV. The dashed red line is the projection of the CRESST-II phase-2 run to an exposure of 500 kg-days, which is expected to be reached in mid 2015[26]. The increase in sensitivity by higher statistics is only marginal at small WIMP masses, however, in the high WIMP mass regime it still scales with the exposure. The blue dash dotted line shows the expected exclusion limit for an exposure of only 50 kg-days with an improved detector type of 24 g target mass each as it is planned for CRESST-III [26], enabling an energy threshold of ~ 100 eV. With the CRESST detectors being performance limited when hunting for WIMPs of small masses and exposure limited above about 10 GeV, two general research-and-development branches arise.

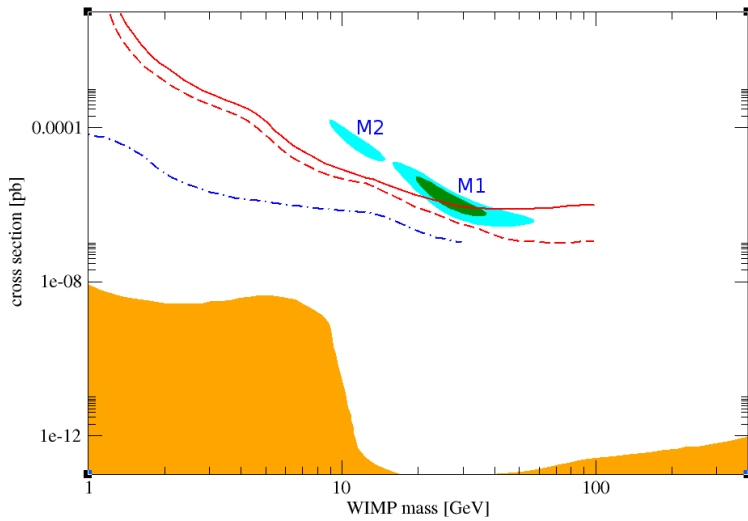


Figure 2.8: Past, recent and possible future exclusion lines obtained with the CRESST experiment. M1 and M2: maximum likelihood maxima for a possible WIMP with 1σ (turquoise) and 2σ (green) certainty as obtained from the previous run (see text for more information) [19]. Solid red: Exclusion limit of 29 kg-day exposure with the TUM40 detector [23]. Dashed red: projection of the current run to 500 kg-day exposure, which is expected to be reached in mid 2015 [26]. Dash-dotted blue: Expected sensitivity of the next run [26]. Orange: background of coherent neutrino scattering [24].

At WIMP masses above ~ 10 GeV, where the detection sensitivity is limited by exposure, the accessibility of smaller cross sections for a given WIMP mass is a matter of overall target mass or measuring time respectively. The last run already lasted for about two years, so extending the running time by orders of magnitude is not really an option. Therefore, an upgrade of detector mass would be required. A simple enlargement of the target crystals does not work, because it would degrade the light output, making it hard to discriminate between different particle interactions.

2.3 Current Status of the CRESST Experiment

An upgrade of the number of modules makes the detector production with anyhow demanding requirements even more challenging. One of the components that would need to be produced in high numbers is the TES. As a rough estimate, an increase of the overall detector mass from ~ 6 kg by two orders of magnitude while maintaining the current detector measures requires 1800 detector modules and thus a total of 3600 TES. The TES for the CRESST experiment up to now were produced at the Max Planck institute in Munich. Unfortunately the production facility in Munich is not capable of producing thousands of TES in a reasonable time.

Another option would be to go for small mass WIMPs, where the detector sensitivity is performance limited. The low energy threshold of a detector is partly determined by the crystal size. Tests with cubic shaped 24 g detectors revealed a significant increase in sensitivity compared to the current detector design. Also the light output improves, enabling a better event discrimination. Thus small detectors with improved performance are very promising to reach for the low WIMP mass regime.

For the next run of the CRESST experiment (CRESST-III) 10 of the 24 g detectors are planned to be used, to aim for the exclusion limit as shown in figure 2.8.

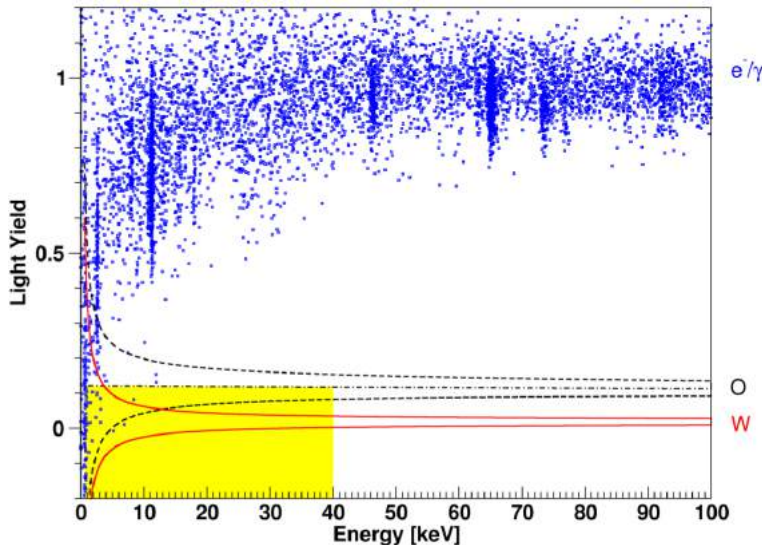


Figure 2.9: Scatter plot of the TUM40 CRESST detector. The nuclear recoil bands of tungsten and oxygen are shown in red and black. The region of interest for WIMP search (yellow) is chosen to contain half of the oxygen recoils between the detection limit (0.6 keV) and an energy of 40 keV. Note that the α and lead background could be rejected [23].

3 SuperCDMS

Since part of the work for this thesis has been done at Stanford university for the SuperCDMS (Super Cryogenic Dark Matter Search) collaboration, this experiment will be briefly introduced in this chapter.

As the name suggests, SuperCDMS is also an experiment that tries to directly detect dark matter. The main difference in the functionality of the CDMS detectors in comparison to the CRESST modules is the reading out of not a light signal, but charge. However, both experiments are reading out phonons as the main signal component with tungsten TES and are working at cryogenic temperatures. The absorber crystals of CDMS consist of either high purity germanium or silicon. The crystals are equipped with electrodes to shape the internal electric field and to read out the charge, and with so called Quasiparticle-trap-assisted-Electrothermal-feedback-Transition-edge-sensors (QETs). Figure 3.1 illustrates the working principle of such a QET unit. As already described for the CRESST light detector, phonons that hit the aluminum break up cooper-pairs and create quasiparticles. These quasiparticles diffuse and get trapped in the aluminum tungsten overlap region, where the superconductivity band gap is smaller, due to the so called proximity effect (see also chapter 4). Thousands of this QET units are covering the surface of the absorber crystals. To read out the signal, hundreds of TES are connected in parallel and in contrast to CRESST they are voltage biased. If one TES is driven to a higher resistance, the current that was going through it will be bypassed through the other TES, reducing the joule heating, and leading to a quick recovery of the TES. This effect is known as negative electrothermal-feedback [27, 28]. It reduces the Johnson noise of the TES which is a limit to its energy resolution, reducing the detector sensitivity. However, to use electrothermal feedback the detector temperature must be about 20% higher than that of the heat sink, costing detector sensitivity for a given bath temperature due to the higher heat capacity of the TES. Which one of this techniques is yielding a higher sensitivity depends on the specifics of the detector design and can not easily be answered. The layer of amorphous silicon, shown in figure 3.1 is necessary to avoid currents between different electrodes.

Apart from differences in the absorber crystal material, two different detector designs are planned to be installed in the SuperCDMS cryostat. The so called iZIP design, with $< 60 \text{ mK}$ TES, and the high voltage (HV) design, that will dispense with the charge signal and concentrate on the phonon readout. The HV detectors require a transition temperature of $< 45 \text{ mK}$ to satisfy the signal-to-noise goals. Since the length and the width of the TESs are restricted by thermal conductance

and photolithographic constrains, the TESs need to be fairly thin (40 nm) in order to yield a high enough resistance of the TES circuit and thus a short signal time constant L/R .

Interested readers will find more detailed information on SuperCDMS detectors in e.g. [29, 30] and [31].

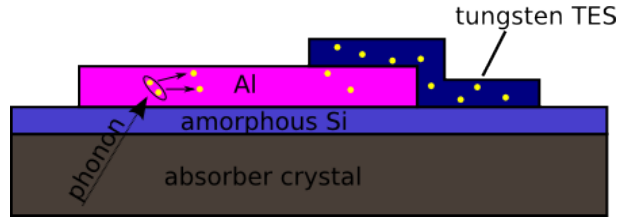


Figure 3.1: Working principle of a QET. Phonons that hit the aluminum phonon collectors will break up cooper-pairs and create quasiparticles. The quasiparticles will be trapped in the tungsten TES and can be read out as an enhanced temperature.

4 Tungsten Film Properties

For direct detection of dark matter in cryogenic experiments using TES, tungsten is the material of choice. In particular its low superconductive transition of about 15 mK and the small heat capacity enable the sensitivity required for the dark matter search. However, the properties of thin films that are needed for TES applications can differ a lot from the properties in tungsten bulk material and can vary over a large range. It is crucial to understand how tungsten films form under different conditions in order to produce films with the required transitions in the range of 15 to 20 mK. This chapter will also show what properties measurable at room temperature affect the T_c , and might enable a presorting of the films before cooling them down for testing at sub Kelvin temperatures.

4.1 General Tungsten Properties

Tungsten is an extreme element in many respects. The tungsten bcc (body-center cubic) crystal structure got the highest cohesive energy of all elements (see also [4.2](#)), even higher than diamonds (carbon). The high cohesive force causes a melting temperature of 3422 °C [\[32\]](#) at atmosphere, which is the highest of all metals. Furthermore, it has the highest tensile strength [\[32\]](#) and the lowest coefficient of thermal expansion. The density of tungsten is comparable to that of gold and its boiling point of 5555 °C [\[32\]](#) is only exceeded by rhenium. A central property when it comes to tungsten being used in TES applications, is the heat capacity. Following [\[33\]](#) it can be derived from the equation

$$C = \gamma T + \frac{12\pi^4}{5} nk_B \left(\frac{T}{\Theta_D} \right)^3$$

The first term is due to the contribution of electrons and the second term describes the heat capacity of the phononic system. The Debye temperature of tungsten below 15 K is $\Theta_D = 378$ K [\[33\]](#) and the specific electronic heat capacity is given by $\gamma = 8.04 \cdot 10^{-6}$ J/gK² at temperatures below 1 K [\[34\]](#). In the low temperature regime the electronic system is dominating the heat capacity of tungsten, leading to

$$C \approx 8.04 \cdot 10^{-6} \text{ J/gK}^2 \cdot T$$

Since $1/C$ is the conversion factor for energy transformed into heat, small values for C are desirable in TES applications. In fact the comparison to the heat capacity of other metals in the low temperature regime like aluminum ($C \approx 5 \cdot 10^{-5} \text{ J/gK}^2 \cdot T$ between 1 and 4 K [35]), shows the suitability of tungsten and makes it an excellent candidate as TES material in cryogenic low sensitivity particle detection (see also chapter 1.6).

As mentioned above the thermal expansion coefficient of tungsten is the lowest of all metals, measuring $4.44 \cdot 10^{-6} \text{ K}^{-1}$ at room temperature [36]. Between 0 K and at least 1700 K it shows the usual, strictly increasing behavior like all elementary metals. In comparison, the coefficient of thermal expansion of the semiconductor silicon turns negative between 20 K and 120 K [37]. At all temperatures it stays well below the one of tungsten and reaches about $2.6 \cdot 10^{-6} \text{ K}^{-1}$ at room temperature [37, 38, 39].

4.2 Crystal Phases of Tungsten

Tungsten occurs in three different crystal phases:

The Alpha Phase

The stable α -phase has a bcc (A2) structure with a lattice constant of $a = 3.16524 \text{ \AA}$ [40]. Most of the extreme properties are associated with this crystal structure, which is the most prominent of all. It is this α -phase that is found to have the high cohesive energy mentioned above. At 0 K, derived from extrapolations, a value of 8.9 eV/atom is reported [40], resulting in a density of 19.246 g/cm^3 [40]. α -tungsten usually has a granular microstructure [41] with grain sizes of typically 100 - 250 nm [42] and a specific resistance of $\sim 5.3 \mu\Omega\text{cm}$ at room temperature in bulk tungsten [43]. The grain size has a direct impact on the specific resistance ρ , due to electron scattering on grain boundaries. Learn et al. report the α -grain size to be dependent on the film thickness [44] and thus the thickness to influence the specific resistance in a non-linear manner. Also scattering on the film surface (“size-effect”), and on impurities contribute to ρ [43, 45]. Therefore, the specific resistance in thin films can differ a lot compared to that in bulk tungsten, depending on film thickness, impurities and crystallinity. On the other hand, for a given thickness, the specific resistance is a good measure for impurity content and crystallinity of a film.

The Beta Phase

The tungsten β -phase is of an A15 structure. Unfortunately, no values of its cohesive energy are reported, but since it is meta stable and converts into the α -phase, the β -tungsten cohesive energy has to be smaller than the one of α -tungsten. The difference in cohesive energy can also be seen in the microstructure. While α -tungsten grows in grains, β -tungsten typically has a columnar structure [46, 41]. Also the density of 18.9 g/cm^3 [40] is lower and the lattice constant of $a = 5.05 \text{ \AA}$ [40] higher compared to the bcc structure of the α -phase. The decay of the β - to the α -phase was observed at room temperature [43] and can be enhanced by heating to about $600 - 700^\circ\text{C}$ [40, 43]. Impurities like P, As, Al, K, [40] and O [47, 48, 46, 49] are known to stabilize the A15 structure. Whether β -tungsten is a phase of tungsten growing at low temperatures, or just a tungsten oxide (W_3O), has been a matter of research for quite some time [41]. But investigations of Moss and Woodward [50] showed, that only little amount of oxygen is sufficient to stabilize the β -phase, less than expected by the stoichiometry of W_3O . Due to the difficulty of producing a pure sample of β -tungsten, for the superconductive transition T_c a range between 1 and 4 K is reported [51, 47]. The specific resistance of β -tungsten is found to have much higher values than α -tungsten ($\geq \times 10$) [42].

The Gamma Phase

The third tungsten phase has a face centered cubic (A1) structure with a lattice constant of 4.15 \AA [52] and a density of about 15.8 g/cm^3 [40]. It has only been observed in thin films, deposited on rock salt (NaCl), glass and mica via sputtering [52]. A transformation of this so called γ -phase to the normal bcc structure can be obtained by annealing. The required temperature seems to depend on the deposition conditions [53] and ranges from $\sim 200^\circ\text{C}$ to $\sim 700^\circ\text{C}$. Chopra et al. [53] also reports the absence of fcc structure in films, deposited at elevated temperatures by thermal evaporation, and the fcc structure showed to be more stable, when deposited by sputtering. That could be caused by a higher content of impurities due to the process gas or by a higher kinetic energy of the tungsten atoms.

4.3 Superconductivity in Tungsten Thin Films

In tungsten thin films, superconductive transitions range from about 15 mK up to ~ 5 K and are primarily dependent on crystal phase composition [54, 52, 51], impurities [55, 56, 57], grain size [58] and film stress [59]. These properties then again strongly depend on the deposition conditions. Therefore, it is crucial to understand these dependencies as far as possible in order to tune the superconductive transition to a specific temperature.

4.3.1 Phase Composition and Grain Size

In pure, unstressed single phase α -tungsten films, the T_c corresponds to the α -tungsten bulk value of about 15 mK [60], whereas films containing other phases can have a T_c as high as ~ 5 K [52]. A central parameter describing superconductivity is the temperature dependent Ginzburg-Landau coherence length ξ_{GL} . It sets the length scale for variations in the wave function of the superconducting electrons. Assuming a tungsten film with regions of α -tungsten next to regions of e.g. β -tungsten at a temperature fulfilling the inequality $T_{c_\alpha} < T < T_{c_\beta}$, according to [61] the β -phase electron wave function would penetrate the α -phase regions, on a length scale of

$$\xi_{GL} = \sqrt{\frac{\hbar v_F l}{6\pi k_B T}} \quad (4.1)$$

The Fermi velocity v_F was found to be of the order of $6 \cdot 10^7$ cm/s [62] and studies of the size effect in tungsten by Choi et al. [45] revealed an electron mean free path l of 19.1 nm. At a temperature of 15 mK equation 4.1 results in a coherence length of $\xi_{GL} \approx 500$ nm. Since ξ_{GL} exceeds the grain size, this so called proximity effect results in "surviving" cooper pairs in α -grains above the actual α -tungsten T_c and thus in an intermediate T_c of the film. A tungsten film T_c , influenced by the proximity effect, depends on the ratio of α - and β -tungsten content and the grain size. So the ability of controlling the growth of different phases would provide the possibility to tune the T_c . Since bcc tungsten is the only stable equilibrium phase, the growth of α -tungsten can be favored by elevated substrate temperatures [50]. Structural order is usually determined by surface mobility of the atoms. Low mobility leads to amorphous film growth, whereas high mobility results in a higher degree of order. For sputter deposited films, apart from heat, also negative voltage biasing of the substrates has a positive effect on the growth of α -tungsten, due to "cleaning" of the films by ion bombardment [42, 63]. The formation of β -tungsten can also be suppressed by avoiding oxygen and other contaminations, that have a stabilizing effect on this phase [47, 49, 46]. γ -tungsten seems also to increase the T_c [52], but since it has only been observed to form under special conditions in sputter deposited thin films [52, 53], avoiding these conditions should suppress this phase.

4.3.2 Magnetic Impurities

Tungsten is a conventional type I superconductor, so the electrons are coupling to spinless cooper pairs. Interactions between magnetic impurities and the spins of electrons can prevent the formation of cooper pairs and lead to a lower T_c [55], or even to the suppression of superconductivity [56, 64]. This effect is quite strong and can even be used to tune the T_c [55]. In films that have an original T_c of ~ 15 mK, magnetic impurities should be avoided, because even little contamination could completely suppress the formation of cooper pairs.

4.3.3 Film Stress

As a conventional superconductor, in tungsten the coupling of electrons to cooper pairs is mediated by phonons. Therefore, it is intuitively understandable, that the phonon spectrum has a huge impact on the superconductivity properties. The phonon spectrum is strongly dependent on the lattice parameters, and thus deformations of the lattice. Also the electron density of states is dependent on the lattice structure and influences superconductivity. In the BCS theory, named after John Bardeen, Leon Cooper and John Schrieffer [65], the relation between phonon spectrum, electron density of states and T_c is given by

$$T_c = \Theta_D \cdot \exp\left(-\frac{1}{N_e(E_F) \cdot V}\right) \quad (4.2)$$

where Θ_D is the Debye frequency and V the interaction potential of the cooper pairs and $N_e(E_F)$ the electron density of states. This simple looking relation in reality is quite complex, when you take a second look. For example in a highly isotropically compressed lattice, Θ_D tends to increase (phonon-hardening) while $N_e(E_F)$ decreases due to band broadening [59]. So even in such a simple case the influences of lattice deformation on the T_c are contrary. The lattice deformations expected in a tungsten thin film in general are of much higher complexity and their influence on the T_c can not easily be calculated.

There are several causes, that can lead to stress in tungsten films, that can be roughly divided into extrinsic and intrinsic sources.

Extrinsic Sources

Using a single crystal as substrate, a mismatch in lattice spacings causes a lattice deformation, when the tungsten takes over the periodicity of the underlying substrate. Epitaxial growth can be avoided by amorphous substrates, or by an amorphous intermediate layer between substrate and film. Film stress caused by a mismatch in lattice dimensions would be referred to as extrinsic.

Also a mismatch in heat expansion coefficients between substrate material and tungsten causes extrinsic film stress, when the film is being heated above, or cooled below its production temperature [51]. In the case of tungsten films deposited at elevated temperatures on silicon substrates, the mismatch in heat expansion leads to tensile stress in the film plane and compressive stress perpendicular to it at room temperature.

Intrinsic Sources

Since α - and β -tungsten differ in structure and lattice constant, a phase transformation from β - to α -phase would cause intrinsic film stress. However, the stress strongly depends on the film microstructure. The transformation of β -tungsten grains, that are surrounded by α -tungsten, or untransformed β -tungsten would put the grain under isotropic tension. In this case, the spacings of the lattice planes would increase isotropically. On the other hand, if the transformation is mainly restricted by the substrate, the initial β -tungsten would be free to contract along the film normal, leading to tensile stress in the film plane and a compressively strained lattice perpendicular to it. Noyan et al. [66] reports compressive stress in the film plane at room temperature for films consisting of "primary" α -tungsten and tensile stress in the film plane for films, where α -tungsten originates from transformed β -tungsten. These films were deposited by sputtering at room temperature, so a mismatch of heat expansion coefficients should not have influenced the stress state. Also other microstructure reformation processes during and after film growth like coalescence (see next section) can introduce intrinsic film stress.

In the case of tungsten films A. M. Haghiri Gosnet et al. suggested inter granular forces to be the cause of intrinsic film stress [67]. For sputter deposited films they observed low substrate temperatures to result in a very porous structure of small grains separated by voids. This structure comes along with tensile stress, since the voids tend to be closed by interatomic attractive forces. With increasing substrate temperatures the grains become bigger, the voids smaller and the tensile stress increases up to a maximum value of about 2 GPa, where the voids are closed and the grains are separated by metallurgical grain boundaries. This structure corresponds to the zone I to zone T transition in the structure zone model by Thornton (see section 4.4). A further increase of the substrate temperature causes the stress to drop again and even to become highly compressive. According to their investigations this effect seemed to be thickness independent in the range between 50 and 1000 nm. The findings of Haghiri-Gosnet et al. are illustrated in figure 4.1. It shows the film stress in dependence on the substrate temperature during deposition, measured directly after deposition and three months after. The percentage of oxygen after three months of air exposure that is shown as well, is a measure for the crystallinity of the film. Films with originally a lot of β -phase tungsten that decays towards the α -phase, will be left with voids in between the grains. These voids then are likely to attract oxygen during air exposure.

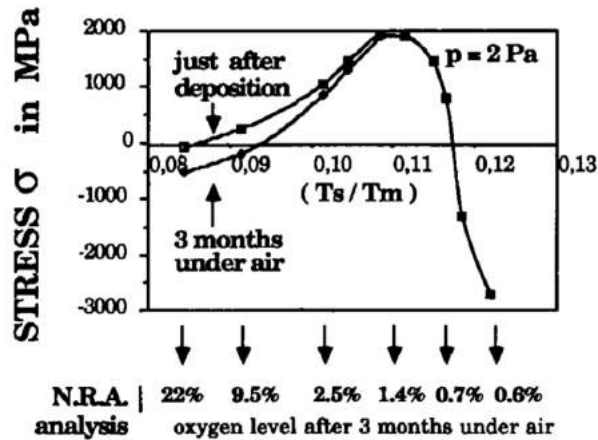


Figure 4.1: Film stress in dependence on the ratio deposition temperature T_s and melting point T_m . Also shown is the oxygen content after three months of air exposure. Porous films are more attractive to oxygen than crystalline ones. The stress originates from inter granular forces, that try to close the voids of porous films [67].

The above suggests, that the understanding of the intrinsic film stress might be used to learn about the film microstructure.

4.4 Film Growth and Microstructure Evolution

In order to understand the microstructure formation in thin tungsten films, this chapter will briefly introduce the different processes of film growth and show how the deposition conditions can influence microstructure evolution. If not stated differently, it is based on [68], [69] and [70].

Nucleation

The very first step of film growth is nucleation. Atoms, that hit the substrate will diffuse along the film surface and start to form islands of uniform crystal orientations. On an amorphous substrate the crystals are oriented randomly.

Crystal and Grain Growth

Randomly oriented discrete nuclei that accommodate additional atoms, form crystals in random orientation, that, at some point will start growing into each other. These crystals can coalesce by surface atom diffusion and grain boundary motion. Complete coalescence is accompanied by coarsening of the film's crystal orientation. In order to lower the substrate-crystal free surface energy, usually the smaller crystal takes over the orientation of the bigger one. However, depending on crystal shape and specific orientation, in some cases a smaller crystal might have a lower free surface energy and enforces its crystal orientation. Thus coarsening can lead to a preferred crystal orientation, also on amorphous substrates. This texture, determined by the minimization of free grain surface energy is referred to as *restrukturierung growth texture*. At low temperatures and for bigger grains coalescence is slower and driven by grain boundary migration. Coalescence and coarsening will go on until the grains reach a size, where grain boundaries become immobile.

After the formation of a largely continuous film layer, also competitive growing among neighboring crystals can lead to preferred crystal orientation. The growing faces of crystals contribute to the free surface energy and different orientations can differ in their propensity of accommodating additional atoms. This process is especially dominant, when grain boundary migration is marginal. Competitive growth leads to the formation of characteristic V-shaped grains, that overgrow neighboring crystals. Ongoing deposition would result in columnar structures of nearly identical crystal orientations. The resulting texture is referred to as *competitive growth texture*.

The Influence of Impurities

During film growth, the impurities in a contaminated particle stream can either be segregated on the growing crystal faces, or dissolved in the grains. In particular the formation of impurity layers at grain boundaries, that cover partially or completely the surfaces of crystals, strongly influences the evolution of microstructure. They either inhibit or promote crystal growth on covered surfaces and, in the case of complete crystal growth suppression, can even lead to repeated nucleation. Depending on the involved elements, also the formation of another crystal phase is thinkable, stabilized by impurities.

The Influence of the Substrate Temperature

Considering the above, substrate temperature plays a major role for the evolution of microstructure. In general an enhancement of atom and grain boundary mobility will lead to bigger grain sizes and will favor the most stable crystal phase. For tungsten, this has been confirmed by e.g. R. L. Moss and I. Woodward [50]. Figure 4.2 depicts different crystal structures in dependence on the substrate to melting point ratio T_s/T_m after the structure zone model developed by John Thornton [71]. Also annealing of the films after deposition supports grain boundary motion. The films produced at the MPI in Munich are deposited at usually about 450°C and annealed at the same temperature for additional 4 hours [72], while T_m is 3422°C.

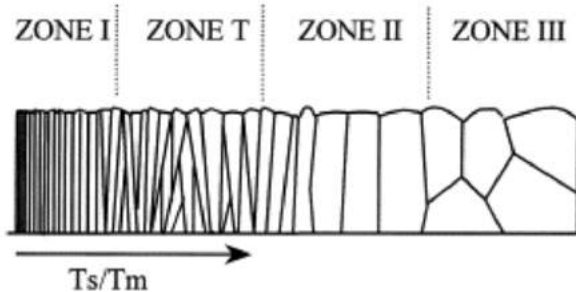


Figure 4.2: Structure zone model for film growth. Zone I: surface diffusion is negligible. Coalescence stops early, resulting in thin fibers. Zone T: Grain boundary migration is strongly limited, but surface diffusion becomes a factor and competitive crystal growth determines the texture. Zone II: Homogeneous microstructure due to grain boundary mobility. Zone III: The crystal growth was inhibited at a certain thickness. This kind of structure is characteristic for very high substrate temperatures, but can also occur at lower temperatures, depending on the presence of impurities [68].

Influences of the Substrate

Also the specific crystal structure and orientation of the underlaying substrate can have a huge impact on the mobility of atoms, and can lead to epitaxial film growth. To avoid influences by the substrate, either amorphous substrates or amorphous substrate coatings can be used [70]. The Munich Cryogenic Vacuum Collaboration investigated the production and usability of single crystalline tungsten films grown on single crystalline sapphire substrates for cryogenic particle detection [64, 60]. However, the required effort was disproportional to the results, and it proved to be feasible to achieve a low T_c also with polycrystalline films.

Influences of the Deposition Rate

Especially in the initial phase of film growth, the deposition rate plays a major role. Together with the atom mobility it sets the time scale for surface diffusion and determines the predominant distance between the initial clusters. The further apart these clusters are from each other, the more space they have to grow and to form big grains.

Influence of the Film Thickness

For substrate temperatures that correspond to Zone II in figure 4.2, until the point during film deposition where grain boundary migration and thus coalescence of grains stops, the grain size is likely to correlate with the film thickness. For tungsten this has been investigated e.g. by A. Learn et al. [44].

Due to the change of surface to volume ratio of grains during deposition, the most stable phase for a thin film might not be the same as for a thicker one. With tungsten as deposition material, films of only few tens of nanometers thickness, produced at room temperature, tend to prefer the meta stable β -phase, as has been observed by several groups [66, 73, 74].

Conclusion

To summarize: the influences on superconductivity in tungsten thin films are manifold and complex. An increase of the oxygen content would e.g. at the same time introduce scattering centers, that hold the potential of breaking up cooper-pairs, disturb the crystal order and favor small grain sizes, stabilize β -phase tungsten and influence film stress via β -phase transformations. In order to yield tungsten films of low T_c , apart from oxygen, especially magnetic contamination should be avoided and the substrates should be heated during deposition to yield a high degree of order. Also the growth rate could influence the film microstructure and thus superconductivity. Small growth rates tend to result in bigger grains.

5 Setup of the Electron Beam Deposition System and Film Production

The setup and commissioning of the facility for tungsten film production was the central goal of this thesis. In the following, the different parts of the facility will be described and put into the context of film production.

5.1 Requirements on The Film Deposition System

The extreme properties of tungsten that are shown in chapter 4 are making it the material of choice for TES in direct dark matter detection applications. However, they also make TES production challenging. To gain high sensitivity, a heat capacity as low as possible is desirable, which scales with the volume of the TES. At the same time the TES should cover some area to efficiently absorb phonons. Therefore, for CRESST thin films of typically 200 nm thickness are chosen as basis for TES production.

In particular the low superconductive transition temperature of tungsten is quite a challenge. Magnetic impurities are known to have a diminishing effect on the transition temperature. They could easily lead to a complete suppression of superconductivity in tungsten and should be avoided. So all materials employed in the deposition system should be non-magnetic.

But also non-magnetic impurities like e.g. oxygen can influence superconductivity by stabilizing the β -crystal phase. To get films of a high α -tungsten content, the deposition should take place in an ultra high vacuum system.

For the same reason, the deposition technique should be as clean as possible. To avoid process gases, electron beam evaporation was the technique of choice. However, the high cohesive energy of tungsten requires high temperatures for evaporation, way above the melting point of all other metals. So, to not melt or evaporate anything but the tungsten, active cooling is required.

Also cooling traps are desirable to support the condensation of residual gas for a better vacuum.

Of the three tungsten crystal phases, in particular α -tungsten shows desirable properties. Since heat has a positive effect on the growth of α -tungsten and on the grain size, heating of the substrates should be provided.

In order to be able to produce TES in large numbers, the production process should be as time efficient as possible. For instance long pumping times could be avoided by introducing a substrate transfer system. Furthermore, as many films as possible should be produced per deposition process. Even deposition onto big areas is easier to accomplish by sputtering than by electron beam evaporation. However, due to the other requirements above, still electron beam evaporation was chosen.

Additionally to the production requirements the deposition system should provide the possibility of monitoring influential parameters like temperatures, the vacuum pressure, the residual gas composition and the deposition rate.

5.2 The Ultra High Vacuum System

The major components of the electron beam vapor deposition system, that has been set up in a class 7 clean room, are two ultra high vacuum (UHV) chambers. The main chamber for the actual tungsten deposition has been designed by Markus Turad, an instrument scientist in the LISA+ collaboration (Center for Light-Matter Interaction, Sensors & Analytics). The second one is a small, 4 liter load lock chamber. Both chambers are equipped with turbomolecular pumps and share a 5 stage roots pump as backing pump. The chambers are separated by a manual gate valve (see figure 5.1). Opposite to the gate valve a magnetic transfer stick is flanged to the load lock chamber. It enables the transfer of the substrates between these chambers without having to flood the main chamber for the exchange of the substrates. Thereby, a low pressure is maintained and the interchanging of substrates can be done quickly, which is helpful, when it comes to mass production of tungsten films. The final pressure of the system is dependent on the temperature. At typical room temperatures of about 25 °C a pressure of $\sim 2 \cdot 10^{-8}$ mbar is realistic. For pressure measurements two full range gauges are in use, that work with pirani technique at higher pressure and use cold cathodes between $5 \cdot 10^{-4}$ and $5 \cdot 10^{-9}$ mbar. After larger modifications inside the UHV system that introduce additional parts or require longer exposure to air, outgassing of molecules that are condensed on surfaces will extend the pumping time. Baking out the chambers can reduce it again to a reasonable duration of about two days. A four channel heating controller with the corresponding heater bands and silicon insulation mats enable stable baking temperatures of up to 200 °C. However, due to some viton gaskets, that do not sustain this temperature, usually a baking temperature of 120 °C was chosen. Also the substrate heater (see section 5.4) can be used to support the outgassing, although it does not reach every surface.

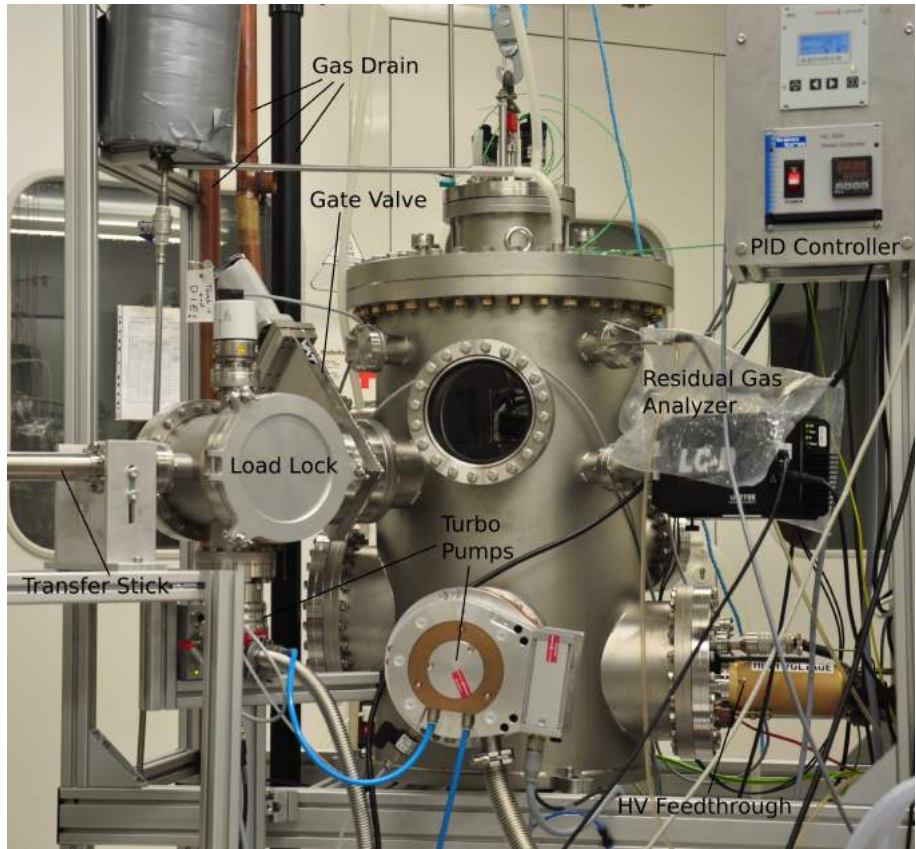


Figure 5.1: The UHV system for tungsten film deposition. The process chamber in the center of the image and the small load lock chamber with the transfer stick on the left are separated by a gate valve. On the right side electronics, water and power supply are connected to feedthrough flanges, from top down of the oscillator crystal, the residual gas analyzer and the electron beam source. The turbo pumps are located below the load lock chamber and below the view flange, pointing towards the camera. Also some pipes for the nitrogen handling (see section 5.5) can be seen.

5.3 The Electron Beam Source

The electron gun in use is a “568 source”, developed by Telemark. It consists of two largely separated parts. An electron beam source unit and a shiftable copperblock containing three crucibles for the deposition materials. Figure 5.2 shows a similar evaporation unit, however with a four crucible copper block. Each crucible can be positioned next to the electron beam source by a linear manipulator. The filament of the electron source is a tungsten coil, usually biased with about 7.5 kV and the emission current is adjustable between 0 and 750 mA via a filament AC current of maximum 40 A at 8 VAC. The electron beam is being shaped by an aperture and then deflected by a permanent magnet on a 270° arc towards the crucible. Two electromagnet coils are connected to the pole shoes of the magnet. The longitudinal and latitudinal impact position of the electron beam in the crucible is adjustable by

manipulating the coil currents and thus the magnetic field lines. Four permanent magnets, that act as a quadrupole magnet focus the electron beam. Due to financial reasons, the electron beam sources power supply, a Telemark TT-6, is shared with another electron gun of the same type, deployed at another UHV chamber. The high voltage is always applied to both sources, so both chambers need to be evacuated to a pressure below 10^{-5} mbar for the usage of one of them. The filament current is only applied to one of the sources, selectable by a switch. At the first tests, the maximum power of 6 kW was just sufficient for the evaporation of tungsten, however, with an unsatisfying rate and much too high heat generation. The cause were 200 V 50 Hz oscillations on the high voltage and apparently uncorrelated disturbances on the deflection coil voltages. The oscillations on the high voltage could easily be removed by lowering the high voltage from 8 kV to about 7.5 kV. It turned out, that the tetrode, which controls the high voltage is above its limits at 8 kV and can not regulate the high voltage properly any more. The origin of the disturbances on the deflection coil voltages could not be identified. After following the suggestions of the manufacturer with unsatisfying results, it turned out to be easiest to buffer the deflection voltages against ground with high capacities. These changes enabled tungsten evaporation at about 2.6 kW with a sufficient rate, that accounts for $\sim 2 \text{ \AA/s}$ growth rate at the substrates. Changes on the deflection voltage influence not only the electron beam impact point in the crucible, but also the beam spot geometry due to another impact angle. At 7.5 kV acceleration voltage, the best focus is in the middle of the crucible, about ~ 5 mm above the bottom. It corresponds to a nearly round beam spot with a diameter of about 5 mm. Depending on the evaporant, different liners can be used. Targets of different sizes with different connections to the liner or crucible, using tungsten wire or washers were tested. The size of the target crystal and its heat flow to the copper block turned out to have a huge impact on the required electron beam power. A cylindrical crystal of ~ 10 mm height and 8 mm diameter (just above the beam spot size), directly put in a tungsten liner, was found to work best. In spite of the water cooling, after evaporation, crystal and liner are slightly melted together, but can easily be separated again by hand.

5.4 The Substrate Holder

The substrate holder is located above the crucible on an extension of the top flange as can be seen in figure 5.3. The substrate holder support structure, together with the top flange can be elevated by a pulley for direct access to the substrates and the heater. A rectangular shaped boron nitride heater is mounted right above the

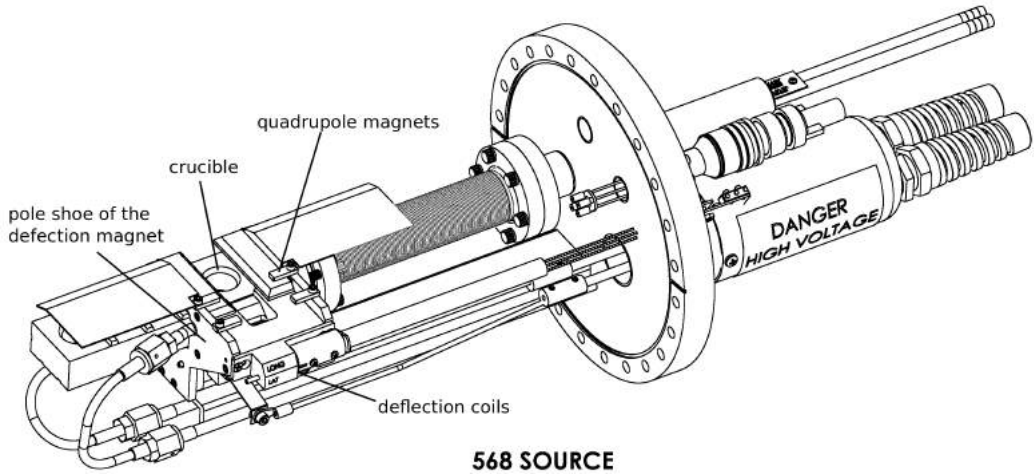


Figure 5.2: The electron gun with the electron beam source unit and the crucible block.

substrate mask, heating its back plate. It is capable of heating up to 2000 °C, but usually heats the mask to only 450 to 500 °C during evaporation and ~560 °C for annealing. Two thermocouples encapsulated in a high melting point, non-magnetic nickel based alloy (inconel 600), fed through the top flange, are in direct contact to the heating element and the substrate mask respectively. They enable temperature monitoring or control via a PID controller. To enable substrate transfer between the two UHV chambers, substrate mask and heating element are separated by a few millimeters, making it impossible to precisely control the heater output current via the mask temperature due to a delayed response. Therefore, the heater thermocouple is used for the temperature control. A set of PID parameters has been investigated, that stabilize the substrate temperature in a range of one degree Celsius. The dependence of the substrate temperature on that of the heater was measured and is depicted in figure 5.4. As measurements show, it follows the equation

$$T_s = 0.700 * T_H + 7.501 \text{ } ^\circ\text{C} \quad (5.1)$$

Several modifications during the setup phase of the system changed the dependence of these two temperatures. The values in figure 5.4 are derived from measurements in the final configuration, with filled nitrogen shields (see also section 5.5). In the current configuration the temperature of the substrate mask can not be monitored, when the mask is placed in its holder structure by the transfer system, since in that case the thermocouple can not be connected to the mask. A contactless measurement with a pyrometer was tested, but proved to be unfeasible. The substrate mask consists of high melting point metals, that show a quite low emissivity at about 500 °C and a direct measurement of the substrate temperature fails, because of the high transparency of the substrates in the infrared regime. Furthermore, during evaporation infrared radiation of the target crystal, reflected inside the UHV

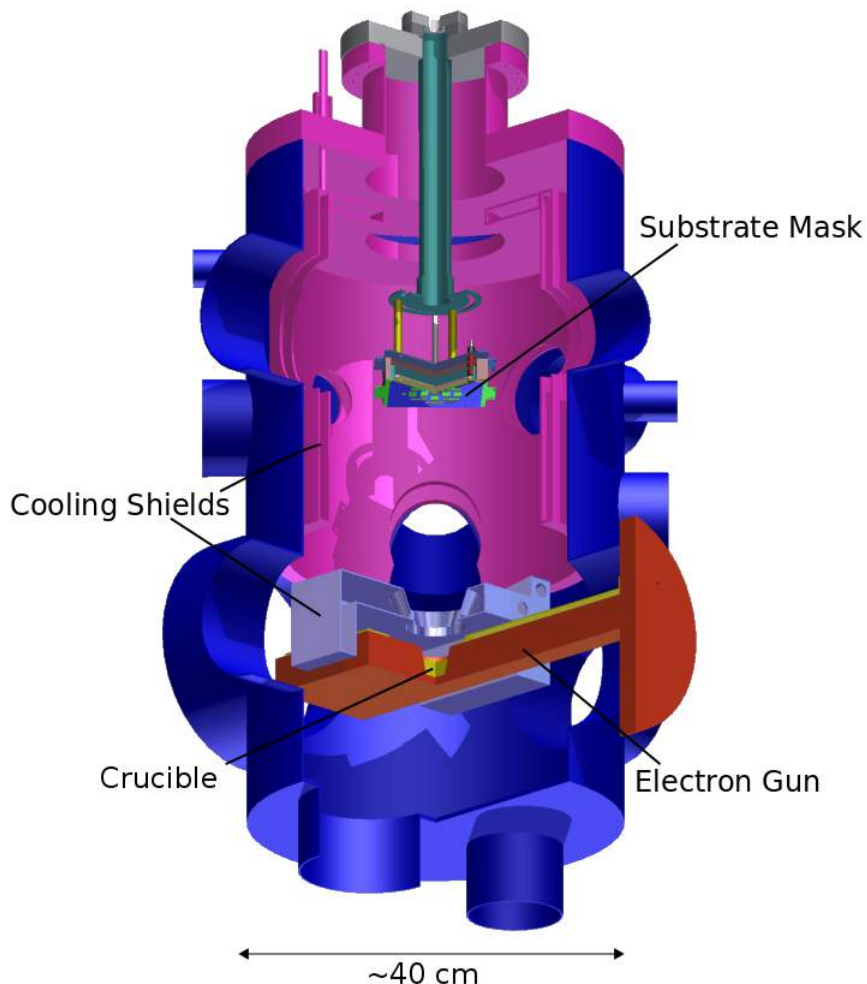


Figure 5.3: CAD drawing of the film deposition system.

chamber, can hit the pyrometer and falsify the measurement. In the possible case that the curve in figure 5.4 will prove to be not accurate enough to determine the substrate mask temperature from that of the heater in the degree needed to control the superconductive properties of the films, a wobble stick that would need to be flanged to the process chamber could be used to press a thermocouple with specified contact pressure to the mask and this way enable an independent measurement of the substrate mask temperature.

High heater temperatures could cause outgassing of the material in the direct vicinity of the substrates, affecting the film composition, the film structure and even lead to the suppression of superconductivity. Especially magnetic impurities are known to

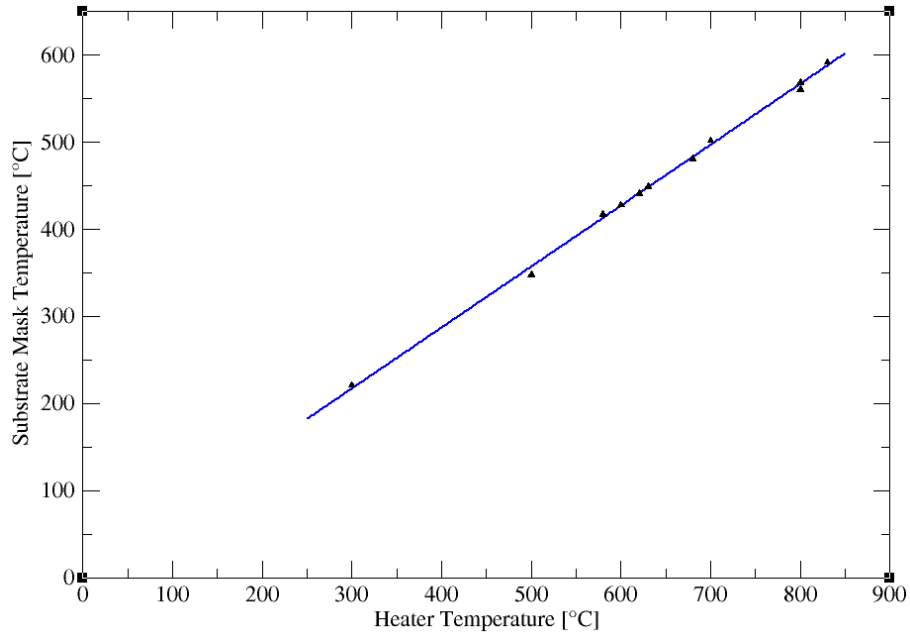


Figure 5.4: Temperature at the substrate mask versus that of the heater. The data points are fitted with a linear graph that follows equation 5.1. Only pairs of temperature values were taken, that account for the same conditions of a pressure in the low 10^{-8} mbar regime, filled nitrogen shields and the electron gun being switched off.

have a huge impact on superconductivity properties. Therefore, the substrate mask and its holding structure are made out of non-magnetic high melting point materials like tantalum, titanium and molybdenum. The substrate mask is limited in size by the dimensions of the heater, to ensure an even temperature distribution. There are 19 substrate spots in the mask, 12 for 20 mm x 10 mm substrates and 7 for the smaller 5 mm x 10 mm ones (see figure 5.5). They are held in total by three tantalum plates. The base and the middle plate are 1 mm thick and have longitudinal notches aligned in a circle to hinder the heat flow and build up temperature in the area of the substrates. While the base plate is solid in the center area, the middle plate has notches for the substrates. the third plate also has such rectangular notches, though of slightly smaller size. It holds the substrates in place, still enabling deposition. The middle plate can be exchanged and adapted to the substrate thickness.

The distance from the target crystal to the substrates is a compromise between evaporation power and an even growth rate over the whole area of the substrates. Originally the distance was chosen to be ~ 350 mm. To be able of reducing the power by about a factor of 1.4 to ~ 250 mA at 7.5 kV and 2 \AA/s , the substrates were lowered by 50 mm. The difference in thickness variations from the center to the

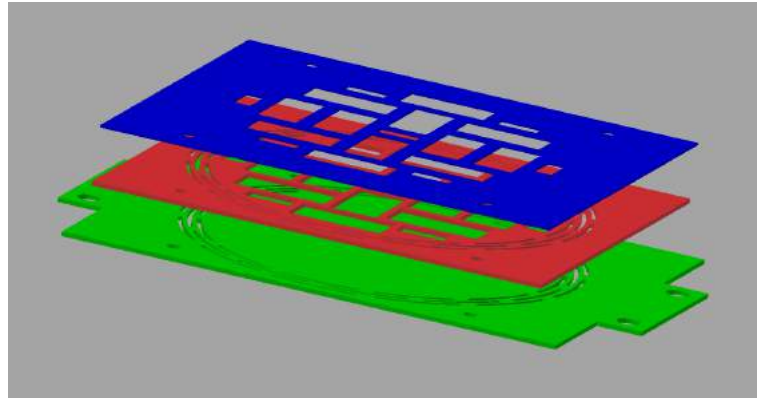


Figure 5.5: The three tantalum plates of the substrate mask. For a description see text.

outside before and after the lowering are shown for the 7 smaller substrate spots in figure 5.6. The values were taken from three film batches respectively, using a stylus surface profiler. The numbers show, that the lowering of the substrates had no significant impact on the thickness variations from the center to the outer substrate spots. However, with an in average nearly halved standard deviation the measurement suggests that the particle stream became less sensitive to slight differences in the geometric configuration of target crystal and electron beam. The thickness variations also depend on the position of the target crystal in the crucible. The values in figure 5.6 were taken in each case from three batches of films with the target crystal located in the center of the crucible. Keeping the advantage of the load lock, the distance between substrates and crucible can not be chosen arbitrarily, because the substrate height has to coincide with the flange that is used for the substrate transfer. The distance reduction between substrates and crucible enabled a power reduction from $\sim 2.6 \text{ kW}$ to about 1.9 kW for a film growth rate of $\sim 2 \text{ \AA/s}$ as planned.

5.5 Radiation Shielding

Thermal evaporation of tungsten is related to an enormous heat generation. Even at a pressure of about $5 \cdot 10^{-8} \text{ mbar}$ for a reasonable rate, temperatures in the range between 3100°C and 3600°C are required. These temperature values were derived from weight loss measurements of the target crystal and evaporation versus temperature values from the CRC Handbook of Chemistry and Physics [75]. Outgassing of the surroundings could contaminate the tungsten particle stream, so radiation shielding with efficient cooling is required. Two cooling shields are mounted inside the ultra high vacuum (UHV) volume, supporting the condensation of the residual

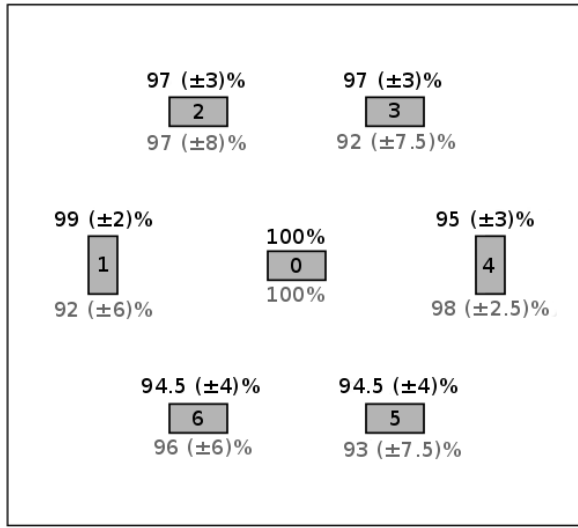


Figure 5.6: Comparison of local film thickness variations before (grey) and after (black) lowering of the substrate holder structure, derived from three film batches respectively. The grey areas represent the substrate spots within the mask. Note that the variations between different batches tended to decrease after reducing the distance to the crucible.

gas and protecting the surrounding materials. The bigger of the two volumes measures about 6 liters and goes along the inside walls of the main chambers upper part (see figure 5.3). To remove the power radiated towards that shield, about 70 to 80 liters of liquid nitrogen are required for the production of a film batch. This nitrogen, when evaporated, takes up the space of more than 50 cubic meters and could displace the room air, leading to a dangerous drop of the oxygen content. For safety reasons, additionally to the ventilation system of the laboratory, a gas drainage system is installed (see figure 5.1) that is connected to the ventilation system of the building. The second box like shaped shield is mounted above the electron gun. An opening right on top of the crucible enables the particle flow towards the substrates (see figure 5.3 and figure 5.9). Like the other cooling shield, this box is made out of a heat resistant stainless steel alloy and contains a volume of about 2.5 liters. Two of its three connector flanges, an inlet and an outlet are connected to a flange of the main chamber. The third one, intended as an optional second pressure release or inlet is not in use and therefore provided with a blind flange. Originally there was another cooling shield intended to be installed above the electron gun, but it proved to be of an unfortunate design. The pressure build up due to evaporation inside the cooling shield hindered the inflow of liquid nitrogen. Filling it with higher pressure was not possible. An unfavorably placed welded joint that connects a cooled and an uncooled and already deformed metal sheet might not have sustained higher pressure (see figure 5.7). The currently installed cooling shield doesn't have any uncooled parts and the only welded joint directly exposed to radiation is not in direct contact with the nitrogen. Due to financial reasons two other, more simple

5.5 Radiation Shielding

versions of shields were tested before the installation of the 2.5 liter box, but did not yield the desired results (see also chapter 6). The most simple version did not provide active cooling. It consisted only of a three layer structure of stainless steel sheets, arranged around the electron gun. The next, more advanced version was constructed out of seamless stainless steel pipes, bent into a loop (see figure 5.8). Metal sheets welded to the pipe completed it to a box like structure. This shield was run with water. The advantage of water compared to liquid nitrogen is, that at room temperature it is far from its boiling point, ensuring a better heat coupling. Liquid nitrogen is harder to handle due to the build up of pressure and the temperature changes of the cooling shield can lead to cracks. Also the heat coupling to the metal deteriorates once the nitrogen turns to gas (“Leidenfrost-effect”). But keeping the Boltzmann equation in mind, the low temperature of - 196 °C is a pro argument and a liquid nitrogen shield acts as cold trap, supporting the condensation of residual gas. Taking all this into account, it is hard to directly compare water and nitrogen as cooling fluids, since the cooling power strongly depends on the specific designs. In particular important is a high flow rate for water cooling and for nitrogen a good pressure release and a design that minimizes the Leidenfrost-effect.

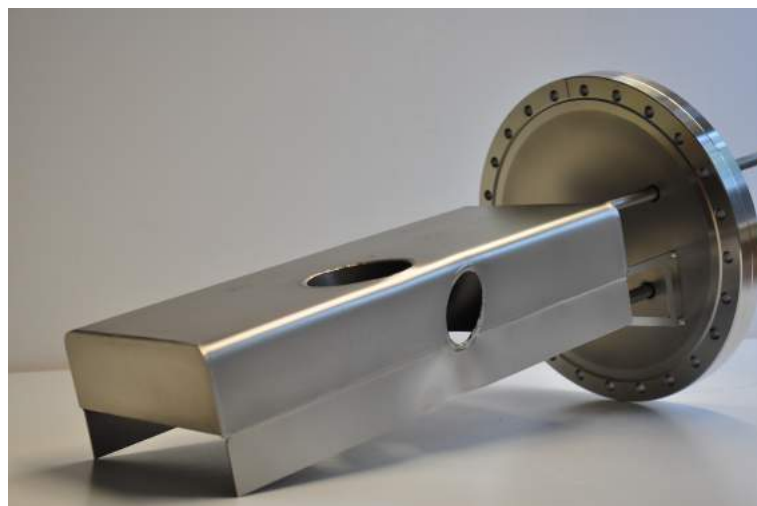


Figure 5.7: The first version of a nitrogen cooling shield. The additional hole at the side provided a direct view on the crucible via a view flange. The deformation of the uncooled metal sheet at the side led to the decision to not fill this shield with the required nitrogen pressure and thus to its rejection.



Figure 5.8: Version of a cooling shield operated with a constant water flow. It was exchanged by another, nitrogen operated cooling shield, since it appeared to not yield the desired results (see also chapter 6). The lengthy hole again provides a direct view via a few flange.

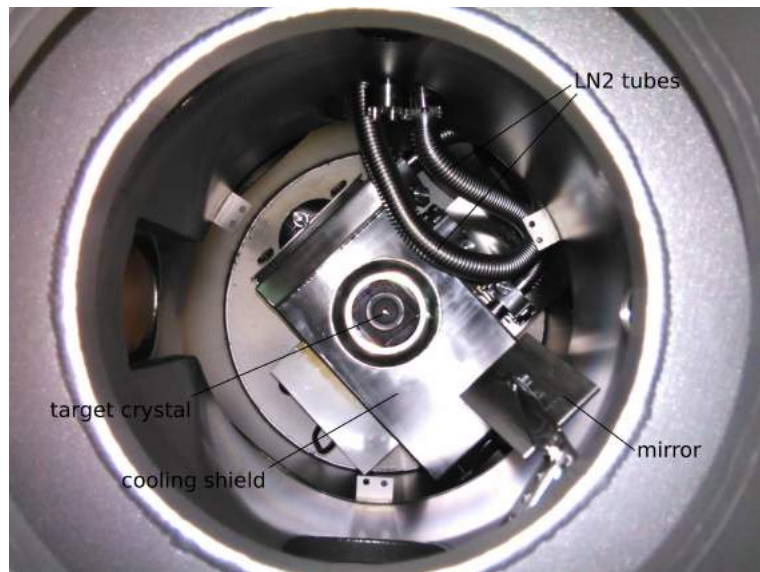


Figure 5.9: The final version of the cooling shield with a box like shape. It was tested with a liquid nitrogen over pressure compared to atmosphere of about 0.8 bar, which is by far enough for operation.

5.6 Growth Rate Monitoring

Monitoring the growth of thin films during deposition in vacuum is done by the well established oscillating quartz crystal microbalance technique. Taking advantage of their piezo electric character, quartz crystals are being stimulated to oscillate

at their eigenfrequency. Deposition of a thin film on the crystal surface causes the eigenfrequency to drop in a highly reproducible manner. Measuring of the frequency difference reveals the mass, loaded on the crystal:

$$m = m_q \cdot \frac{\Delta\nu}{\nu_q} \quad (5.2)$$

m = deposited mass

m_q = mass of crystal

$\Delta\nu$ = shift of eigenfrequency

ν_q = eigenfrequency

However, this equation is only valid when the mass of the deposited film is much smaller than that of the crystal and the frequency shift is limited to 2 % [76]. In order to increase the quartz crystals life time, based on the work of J. G. Miller and D. I. Bolef [77], C. S. Lu and O. Lewis [76] extended this simple relation to equation 5.3, that also accounts for elasticity properties of the deposit.

$$m = \left(\frac{\rho_q N_q A}{\pi Z \nu_L} \right) \cdot \arctan \left(Z \cdot \tan \left(\pi \frac{\nu_q - \nu_L}{\nu_q} \right) \right) \quad (5.3)$$

$Z = (\rho_q \mu_q) / (\rho_f \mu_f)$ = Z-factor of film material

ρ_q = density of quartz

ρ_f = density of film

μ_q = shear modulus of quartz

μ_f = shear modulus of film

N_q = frequency constant for AT-cut quartz crystal. $N_q = 1.668 \cdot 10^{13}$ Hz Å [78]

A = surface area of quartz

ν_L = resonance frequency of loaded crystal

ν_q = resonance frequency of unloaded crystal

The Z-factor can be interpreted as oscillation coupling between quartz and deposit. It could cause a problem, in the case of two deposition materials, that are layered. The electron evaporation facility that has been set up in the framework of this thesis is foreseen to not only be used for tungsten deposition, but also for SiO₂ as evaporant in order to coat substrates that don't come with a SiO₂ surface with an intermediate, epitaxy breaking layer (see section 5.8). Film thickness measurements in the case of alternating deposition of two materials with different oscillation coupling to the quartz is usually performed by choosing an intermediate Z-factor. Since SiO₂ is just the formula for quartz, the Z-factor for SiO₂ must be unity, whereas it is 0.163 for tungsten. This big difference in oscillation coupling effects the thickness measurement accuracy and limits the lifetime of the crystal to only few layers. Having to exchange the crystal after every production of a film batch would override

the advantage of the transfer system. Therefore, for tungsten TES production on substrates that are not already provided with a SiO_2 layer, a second oscillator crystal should be installed. The installation of either a second single headed crystal, or that of a double headed one, equipped with an electro pneumatic shutter can easily be done, but is quite costly.

Since oscillator crystal and substrates are not at the same place, a linear *tooling factor* has to be introduced, that compares film growth on substrates and crystal. The tooling factor for the current geometric configuration has been determined from the film growth measurements performed with the quartz and the film thickness data, independently recorded using mechanical surface profiling. It proved to be 2.9. So the growth rate measured with the quartz crystal has to be multiplied by 2.9 to determine the growth rate at the substrates.

The crystals resonance frequency also depends on its temperature. So an unstable crystal temperature would result in incorrect thickness measurements. To eliminate this effect, water cooling of the crystal is provided.

5.7 The Residual Gas Analyzer

To monitor the residual gas composition, a Dycor LC-D series residual gas analyzer of the company Ametek is flanged to the main chamber (see figure 5.1). It is based on the operating principle of a mass spectrometer and has its working range in the UHV regime below 10^{-4} Torr, corresponding to about $7.5 \cdot 10^{-5}$ mbar and has the capability of measuring partial gas pressures down to $5 \cdot 10^{-12}$ mbar. At the final gas pressure in the low 10^{-8} mbar regime the residual gas is dominated by water. It originates from room air, that condensates on the surfaces within the UHV chamber. To reduce this effect, to open the UHV chamber it is being flooded with nitrogen gas and all cooling systems, even that of the turbo pump are switched off a few hours in advance. Also cleaning of surfaces with isopropanol supports condensation by evaporative cooling, followed by enhanced condensation on the cooler surfaces. Therefore, clean working conditions are essential. Second strongest represented in the residual gas is nitrogen (N_2), followed in this order by OH, CO_2 , H_2 , H, O_2 , O, N and C. This are all gas components of air, or split air molecules. At UHV pressure, pumping of residual gas works ballistically, meaning that only molecules that hit the turbo pump are removed. Baking of the UHV chamber causes the molecules to accelerate, increasing the possibility of them hitting the pump and support outgassing of the condensed water. Therefore, the baking reduces the overall pressure, and especially the partial pressure of water. However, metal is permeable to hydrogen. At higher temperatures, hydrogen inside the chamber walls gases out and contributes more and more to the residual gas, since it is poorly pumpable. During film production, the heat generated by the substrate heater and the electron beam source has an effect on the residual gas, similar to baking. Simultaneous cooling of the liquid nitrogen shields further reduces the partial pressures, particularly that of water. Figure 5.10

5.7 The Residual Gas Analyzer

shows the partial pressures of molecules in the mass over charge range between 0 and 80, during film production. If the molecules are just simply ionized, the different molecules show up in that plot at mass over charge numbers that are equal to their number of nucleons, which exemplary for water is 18. The pressure is dominated in this order by hydrogen, nitrogen, carbon dioxide and water. The spikes at lower mass over charge numbers are likely to be caused by multiple ionization due to the electron beam itself and the heat generated by it.

During deposition the partial pressures of the residual gas was logged and saved. Possible correlations between the residual gas composition and superconductive properties of the films could be used to reject unpromising film batches from the TES production and testing process.

Apart from residual gas analysis, the residual gas analyzer proved to be a valuable tool when it came to leakage detection with helium.

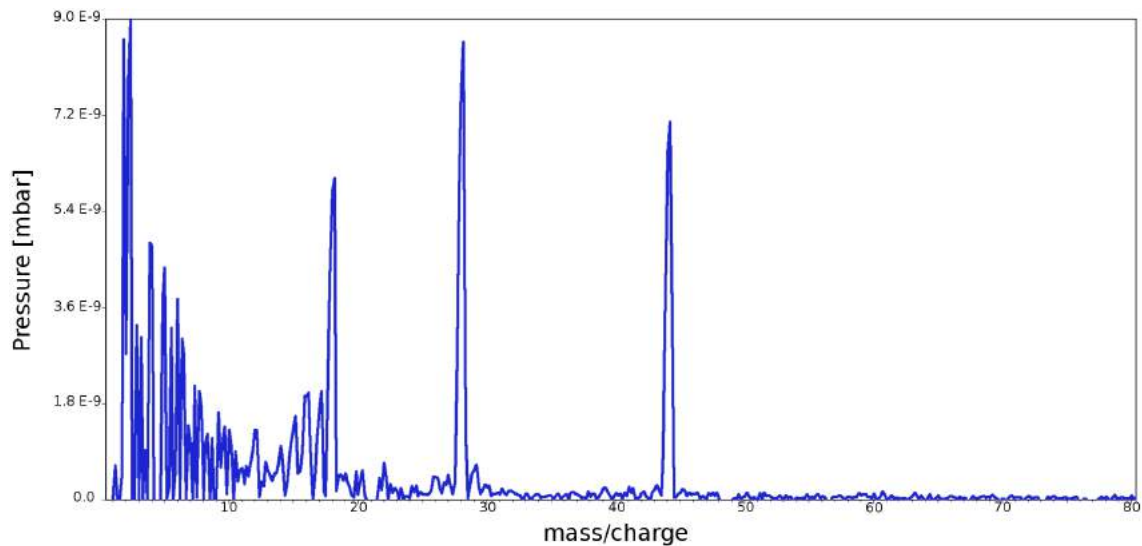


Figure 5.10: Typical partial pressure scan of the residual gas analyzer during film production. The most prominent peaks belong to N_2 (mass/charge = 28), H_2 (mass/charge = 2), CO_2 (mass/charge = 44) and water (mass/charge = 18). For more details see text.

5.8 Film Production

This section will be on the different production steps at the final state of the evaporation facility.

Every production cycle of film batches starts with preparations. Layers of tungsten deposited on the bottom of the cooling shield can peel off, fall into the crucible and contaminate the tungsten with particles from the cooling shield. Several extensions to a vacuum cleaner, manufactured from stainless steel, are helpful to clean the crucible and the bottom side of the small cooling shield.

The tungsten crystals that are usually used weigh about 8 to 9 g and are of cylindrical shape, 9 mm in height and 8-9 mm in diameter. They are monocrystalline with a 001 orientation. The starting material for the growth of these crystals is of 99.99 % purity. After the growth of the crystals and refining by 5 fold zone melting the purity is definitely improved, though the final purity is not specified. Before being placed in the crucible, the crystals need to be cleaned to get rid of surface contaminations. This is done in an ultrasonic bath in this order with acetone and isopropanol before the crystals are finally dried with nitrogen gas.

For the CRESST experiment the tungsten films are deposited on CaWO₄ for the phonon detector and on sapphire for the light detector. To break the epitaxy of these materials, an intermediate layer of SiO₂ is used. Epitaxial growth of tungsten on a substrate with different lattice constant could cause lattice deformations and influence superconductivity properties (see also chapter 4). Since CaWO₄ substrates are not available in the amount needed during the setup phase of the facility, thermally oxidized silicon substrates were used. The SiO₂ layer take up the top 300 nm of the 380 μm thick substrates. It ensures conditions comparable to CRESST requirements. Before the coating the substrates need to be cut in shape and cleaned in the same manner as the crystals and then placed in the substrate mask.

After evacuating the chambers to a pressure of about $2 \cdot 10^{-8}$ mbar, the cooling shields need to be filled and the heater to be started. To be prepared for the case of a sudden cooling shield disruption, the screws of a viton sealed flange are loosened, so the flange can act as an overpressure relief. The fastest way of setting the start conditions for evaporation is as follows:

- Start filling the big liquid nitrogen shield, switch on the cooling water for the electron beam source and the oscillator crystal
- After 90 minutes, start the heater and switch on the electron beam sources power supply (make sure the right source is selected!)
- After 120 minutes, start filling the small cooling shield
- After 135 minutes, start residual gas analyzer and oscillator crystal

It is important to switch on the electron beam sources power supply at least 30 min before applying the high voltage to the filament, because the tetrode that controls the high voltage is indirectly heated and needs time to warm up. After about 140 minutes from starting, everything should be ready to switch on the electron source. The positioning of the electron beam is a bit tricky. The first three versions of the cooling shield (see section 5.5) provided a direct view on the crucible through a view flange, specifically intended for this purpose. However, a direct view means less radiation shielding and also coating of the view flange. This flange is equipped with a shutter and an exchangeable sheet of glass, both on the vacuum side, so this glass sheet gets coated instead of the view flange window. The currently installed liquid nitrogen cooling shield prevents a direct view on the crucible, but provides better shielding. Even though, when deposition is in progress, the shutter of the view flange should only be opened, after placing a welding protection glass sheet of DIN 11 on the flange, to prevent harming of eyes and skin. With the current cooling shield, positioning of the electron beam is done by using a mirror inside the vacuum chamber and the flange above the turbomolecular pump as view port (see figure 5.1). The mirror is situated next to the substrate holder support structure and consists of a polished stainless steel plate. The coating with tungsten makes it highly reflective and enables an indirect view on the crucible. The beam positioning via the mirror requires some practice.

The substrate mask and the oscillator crystal are provided with manual shutters. The substrate shutter should be closed at the start of the electron beam source, so impurities from the crystal surface don't end up on the substrates. The heat generated by the electron beam will cause the vacuum pressure to increase by about an order of magnitude, until evaporation sets in. Evaporated tungsten atoms are gettering residual gas molecules, leading to a drop of pressure that stabilizes at about $5 \cdot 10^{-8}$ mbar, depending on the heat generated at the target crystal and the initial pressure. After annealing the crystal for some minutes, the substrate shutter can be opened and deposition started.

The growth rate is a parameter that can influence the superconductivity properties of the films. A high growth rate can cause “chunks” of tungsten to hit the substrates, leading to uneven growth, or influence the crystal structure, when the tungsten atoms don't have sufficient time to find the deepest potential wells associated with the α -phase. Slow deposition on the other hand favors chemical reactions of tungsten atoms with the residual gas and could result in e.g. an oxygen content in the films. Here it shows to be essential to control the residual gas pressure and composition in order to yield the highest purity possible. The growth rate can easily be varied and is usually chosen to be only 0.1 \AA/s in the beginning to yield a base layer of large α -tungsten grains and then slowly increased up to 2 \AA/s , to get a film of high purity.

The substrate temperature is not only dependent on the heater temperature, but also on the temperature of the target crystal, the growth rate, the heat coupling to the mask and on its specific material and thickness of the tungsten layer. The heater

temperature can easily be varied, using a PID controller. Growth rate and tungsten crystal temperature are directly coupled. The crystal heats the substrate mask via infrared radiation and the incident tungsten particles, that form in a crystal lattice, heat the substrates with their thermal and cohesive energies. Monitoring the substrate mask temperature revealed an increase of about 5 °C during deposition at an initial temperature of ~ 500 °C. The infrared radiation power absorbed and emitted by the substrates depends on its material and thickness. Monocrystalline silicon itself is largely transparent in the infrared regime, but the growth of a tungsten surface layer changes that. Therefore, the substrate temperature has to be assumed to increase during deposition. One way to even out this effect is by ensuring a fast heat flow between substrates and mask. Since the intermediate tantalum sheet of the substrate mask is 1 mm thick, whereas the substrates measure 0.380 mm, they are usually stacked with “dummy” substrates, that fill the space between substrates and base plate. To not introduce new materials, they either consist of silicon or tantalum. In spite of this heat link, the temperatures of substrates and mask will most probably not be the same, but linearly dependent. A direct measurement of the substrate temperature has not been performed, due to technical difficulties. Measuring the substrate temperature directly with a thermocouple is thinkable when drilling a hole in a substrate, but it is related to technical difficulties, due to brittle material and small thickness. Also, that doesn't seem necessary, since with good heat coupling to the mask, mask and substrate temperature should be linearly dependent.

After growing a film of about 200 nm, the substrate shutter is usually closed and the electron beam source switched off. The thickness of 200 nm is kept constant for different film batches for better comparison.

To yield an improved crystallinity, the substrates can be annealed after coating. Temperature and duration of the annealing can easily be varied, but are usually chosen to be 500 - 700 °C for 5 hours.

With the cooling shields at liquid nitrogen temperature, the main chamber should not be flooded to avoid ice formation and condensation of dirt. Warming up of the cooling shields takes about 12 hours. Here the transfer system shows to be of value. It enables the production of several film batches within one cooling cycle.

5.9 Mass Production

With regard to a higher sensitivity for WIMP detection in the WIMP mass range above ~ 6 GeV, for the CRESST experiment more detector mass and therefore more TES are needed. Investigating the possibility of TES mass production was part of this thesis.

The time needed to produce a batch of films, strongly depends on the annealing time. Unfortunately, the specific influence of annealing on the superconductivity

properties could not be tested, because of too few reliable transition measurements (see also chapter 6). Also very time consuming is the pumping after e.g. the exchange of the target crystal. It takes about 2 days of pumping until the pressure converges in the low 10^{-8} mbar regime. In order to avoid long pumping times, the load lock chamber together with the transfer stick was installed. So usually the main chamber only needs to be opened to exchange the old target crystal with a new one. One crystal is good for up to four film batches, so thanks to the transfer system, the main chamber only needs to be opened every three to four batches. If necessary also other pockets of the crucible copper block can be provided with tungsten liners and tungsten crystals, to further increase the number of TES produced within one pumping cycle. Since the production of a batch, including preparation work until the start of annealing takes about four hours, and assuming annealing times of a couple of hours, one film batch per day is realistic. Taking the pumping time into account, that makes a total of four batches per week when using just one of the crucibles. In the current configuration the substrate mask has spots for 12 big and 7 small sized substrates (see section 5.4), enabling the production of 48 big and 28 small sized films per week. The fraction of films that suffice the requirements for being deployed on CRESST like detector modules is still a matter of research, since the superconductivity properties of the films could not be tested to the extent needed. The rate of film production depends on several TES requirements like the substrate size, film thickness and number of evaporants needed, which might need to be adapted to changes in the detector design. So the numbers above are rather an estimate of what the evaporation facility is capable of. They show, that in general even the production of a four digit number of tungsten films should be possible with this evaporation facility within a period of few years.

After film deposition the next step in the processing chain of TES production would be to test the films for their superconductive transition at sub Kelvin temperatures. This is done by using a $^3\text{He}/^4\text{He}$ dilution refrigerator. Since every wire going inside the cryostat introduces a heat load, the number of wires that can be used for measuring is limited by the desired base temperature. Therefore, usually only few films can be tested in one cool down. To widen this bottle neck, in Tübingen a multiplexed SQUID system is in work and will be installed in a cryostat in near future [79]. Not to widen, but to avoid the bottle neck, the films can be tested at room temperature for properties, that are related to their superconductivity properties (see als chapter 4). This could allow presorting of the films.

To make a TES from a tungsten film, the surface has to be provided with the possibility for electrical and heat connections, or in the case of a CRESST like light detector with phonon collectors (see section 2.2.2). The surface structuring is a quite straight forward process, involving photolithography, surface etching and deposition of aluminum or gold. All individual steps have been tested and didn't show any major difficulties. When it comes to mass production of TES, the surface structuring can easily keep up with the film production as long as the man power is provided.

6 Results on Superconductivity

As described in section 1.6, for cryogenic particle detection with calorimetric detector modules, in general a temperature as low as possible is favored. Since the superconductive phase transition temperature defines the sensitivity range of a TES, tungsten films of low T_c are required. Moreover, the slope of the transition edge is a parameter that affects the sensitivity. The steeper the slope, the higher the resistivity change for a given temperature change. These properties need to be tested for every tungsten film to define its suitability for employment on calorimetric detector modules. This chapter will show results on transition curve measurements.

6.1 Results of R(T) Measurements

For the purpose of cryogenic detector development a Kelvinox 400 HA dilution refrigerator has been installed in an underground laboratory at the physical institute in Tübingen (see also [16] and [79]). Its nominal base temperature of 4.54 mK is usually exceeded by about 5 to 10 mK, depending on the heat load by e.g. wiring. This cryostat has been used to test the tungsten films for their superconductive phase transition with a SQUID. The first two films that were tested were electrically connected to the read out interface by aluminum wires, directly bonded onto the tungsten surface. The measured resistance over temperature curve showed a quite odd behavior (see figure 6.1), that was far from any expectation.

This was assumed to be caused by a temperature dependent contact resistance between the bonds and the film. To solve this problem, all following films were furnished with four aluminum contact pads in the corners of the films. The pattern of four pads was chosen to also enable four point measurements of the specific resistance (see also section 7.2). For all the surface patterning of the tungsten films, another UHV system was used. It consists of a central handling system, encircled by a locking chamber and several process chambers. Once placed in the locking chamber samples can be transferred by the handling system to the different process chambers. This way the tungsten films are not exposed to air in between two processing steps. The process chambers used in this work were an etching chamber for chemical (SF_6 , O_2) and mechanical plasma etching (Ar) as well as another electron beam

6.1 Results of $R(T)$ Measurements

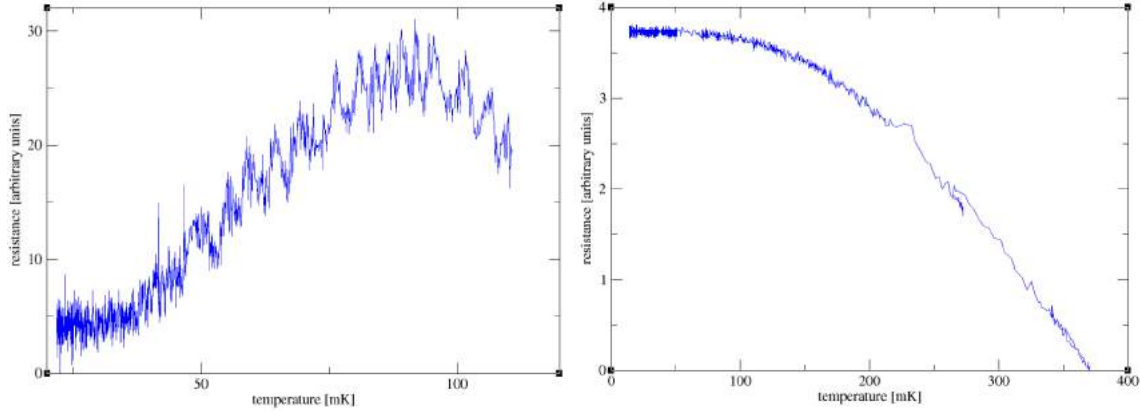


Figure 6.1: Odd $R(T)$ behavior of two tungsten films, where the aluminum wires for electric connections were directly bonded onto the tungsten surface.

evaporation chamber for aluminum and gold deposition. The surface structure of the films can either be defined by photolithography or by the usage of a shadow mask. Prior to the deposition of the aluminum pads the layer of natural tungsten oxide, that immediately forms when exposed to air, needs to be exposed. To do so, the substrates were put into a shadow mask (see figure 6.2) and exposed to the argon plasma source for mechanical etching.

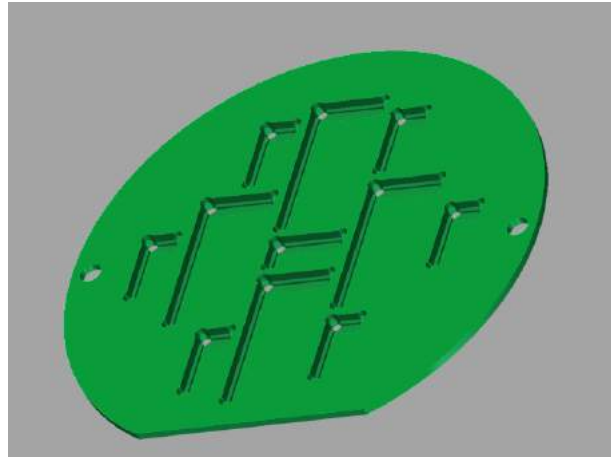


Figure 6.2: Shadow mask for aluminum pad deposition and mechanical etching. Dimension: 7.5 cm

In order to investigate the etching rate, several test runs were performed. For these tests the tungsten surfaces of some films were coated and patterned with photoresist prior to etching. The resulting sharp edges enable precise height profile measurements with an atomic force microscope. All tests were performed with

Argon at a flow rate of 6 sccm (standard cubic centimeter per minute), 100 W of RF-power and differing etching times. Figure 6.3 shows the results of these tests, fitted with a regression line. Since there is no kink in the data, tungsten and tungsten oxide seem to have similar etching rates, preventing the thickness determination of the tungsten oxide layer by this test. The linear graph suggests an etching rate of 0.08 nm/s.

To make sure that all oxide was removed before the deposition of the aluminum pads, 30 nm of material were cleared off. The aluminum pads were deposited by electron beam evaporation immediately after the etching. Equipping the films with those pads solved the contacting problems.

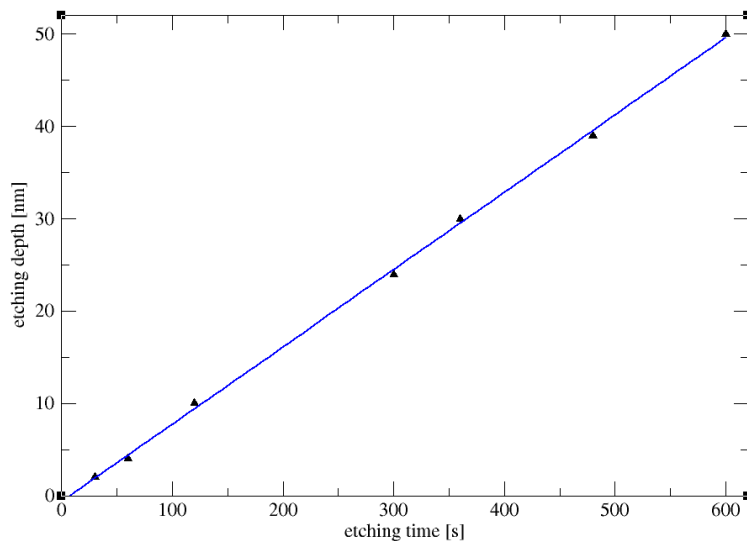


Figure 6.3: Etching rate for tungsten with an argon plasma source. The data points were fitted with a linear graph. The rate accounts for about 0.08 nm/s.

The following measurements that were performed in Tübingen always showed the same behavior. Below 2 K the R(T) curves stayed flat with falling temperatures and showed a drop off at about 1 K, where the aluminum bonds become superconductive and an additional one, typically between 180 and 250 mK (see figure 6.4). In spite of massive changes at the deposition conditions, this general behavior did not change. However, the deposition conditions were assumed to largely affect the transition temperature, so some films were sent to the Max Planck institute in Munich to crosscheck their R(T) curves at another cryostat. The two films that were tested showed the same behavior, just with an additional drop off at about 15 mK, as can be seen in figure 6.4. The reason why this drop off has not been seen at the cryostat in Tübingen is due to two facts. The cryogenic resistivity measurements were not absolute. All connectors and the wiring introduce resistances, that shift

6.1 Results of $R(T)$ Measurements

the resistance of a superconducting sample from 0Ω to a finite value. This led to the false interpretation of the step at $\sim 200\text{ mK}$ as superconductive transition. Furthermore, the fact that the resistance drop off at $\sim 15\text{ mK}$ has not been observed in Tübingen, leads to the conclusion, that the measured cryostat base temperature of about 12 mK has not identical with the temperature of the films. The origin of the step at $\sim 200\text{ mK}$ however is still unclear. It might be caused by the $\sim 50\text{ nm}$ thick aluminum pads that, affected by the proximity effect, show a lower transition than the aluminum wires, or exhibit a lower transition due to a changed microstructure of the aluminum on top of the tungsten layer. The first case could be confirmed or ruled out e.g. by varying the thickness of the pads. The second hypothesis is being supported by the SEM images in figure 6.5. The images show a silicon wafer with aluminum and tungsten films on top. In the left image the tungsten was deposited last and is overlapping the aluminum in some areas. In the right image the tungsten was deposited first and the aluminum last. While in the overlap region the formation of the big aluminum grains seems to be suppressed when it was deposited ontop of the tungsten, the aluminum grains in the left image show no difference in the overlap region and the rest of the film. These images were taken from devices that were produced at Texas A&M for the study of the quasiparticle diffusion length at the university of Stanford. The change of grain size might explain a change in transition temperature and thus the step in the R versus T curve below.

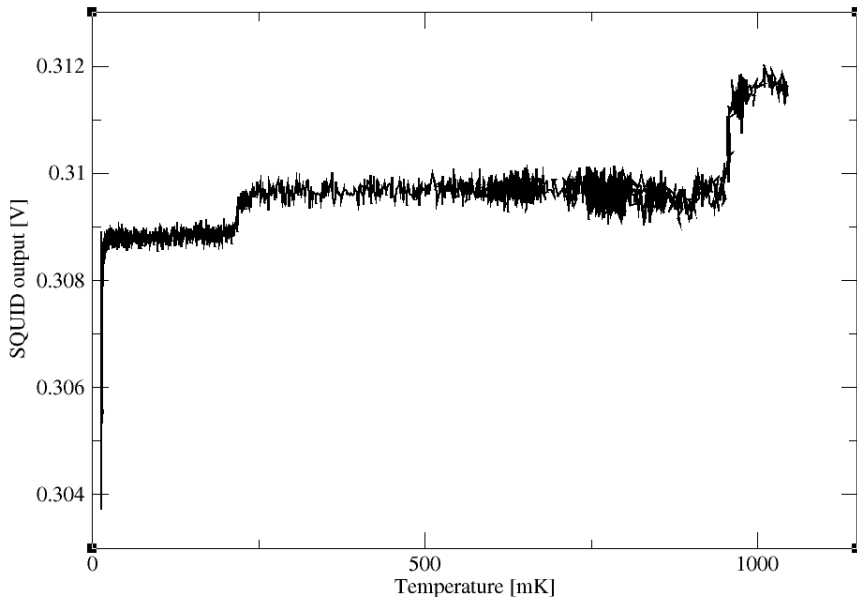


Figure 6.4: SQUID output versus temperature curve of film 140527_0. The step at about 1 K is due to the superconductive transition of the aluminum wiring. The one at $\sim 200\text{ mK}$ might be caused by the transition of the aluminum pads. The drop off at about 15 mK is the actual transition of the tungsten film. Unfortunately the cryostat did not reach a low enough temperature to see the whole transition.

The unfortunate misinterpretation of the R(T) curves made it impossible to study within this thesis, how deposition conditions as well as post deposition treatment correlate with width and temperature of the superconductive transition. Also studies of the film structure measured at room temperature could not be put into relation with the superconductive properties of the films, and the uniformity of transition temperatures over the deposition area could not be investigated. Nevertheless the following chapter will introduce film analysis techniques and report on analysis results on microstructure, resistivity and film strain to develop a better understanding of those film parameters, that might have an impact on superconductivity and could help to preselect the films with the right T_c .

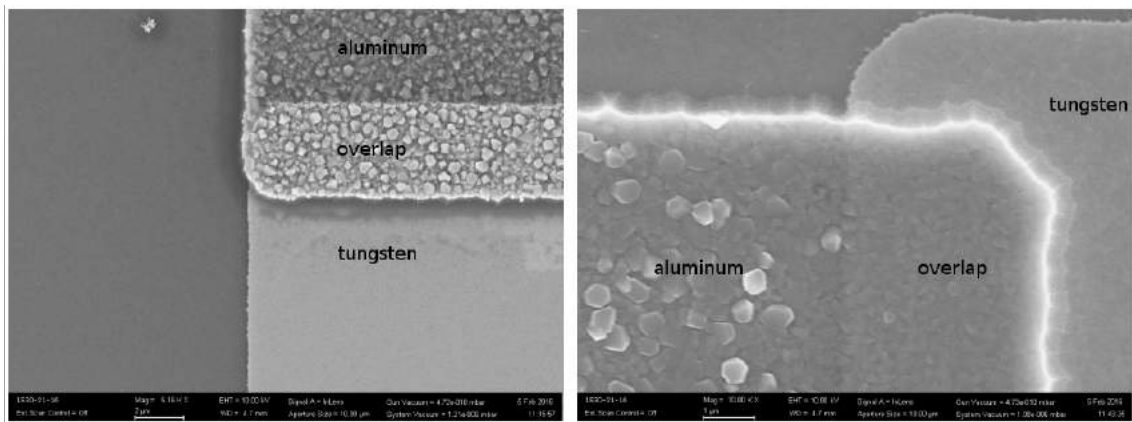


Figure 6.5: Right: the image shows a drastic change in grain structure for aluminum when it overlaps a tungsten film. For comparison the left image shows an aluminum film that is being overlapped by tungsten.

7 Film Analysis

In thin films superconductivity as a quantum effect is very sensitive to even the smallest changes in the deposition conditions. Often it seems almost mysterious how superconductivity properties change while maintaining the deposition parameters apparently unchanged. In order to reproducibly grow tungsten films with the required properties it is crucial to understand the influence of the deposition conditions as well as possible. However, due to the lack of analysis results on superconductive transition properties, the influence of deposition conditions on superconductivity could not be investigated within this thesis. Instead tungsten films have been analyzed with several methods to study the film microstructure and look for structural properties that might affect superconductivity. As mentioned in chapter 4, in particular the crystal phase composition, grain size, impurities and film stress are known to influence superconductivity.

In the following, several analysis techniques that have been applied, will be introduced, their results shown and discussed. If not stated differently, the analyzed films were deposited at substrate temperatures ranging between 450 and 500 °C, with a deposition rate, that increased from about 0.1 to 2 Å/s and a thickness of 200 nm. The films were annealed for about 4.5 hours at about 600 °C.

7.1 Microstructure Analysis

7.1.1 Surface Morphology

Scanning electron microscopes (SEM) produce images of samples by scanning their surface with a focused electron beam. These electrons trigger various kinds of radiation, that contain informations about the sample. For imaging, usually SEM's are taking advantage of secondary electrons, that are generated inside the sample. These secondary electrons are emitted in all directions and are of low energy (~ 50 eV). They are guided to the detector by a charged collector grid that is usually biased with a few 100 volts. The actual detector consists of a scintillator, read out by a photomultiplier tube. The scintillator is coated with a thin metal layer, biased with about 10 kV to provide the secondary electrons with the energy needed to excite the scintillator. The number of secondary electrons depend on the angle at which the beam strikes the surface, resulting in an image that reflects the sample topography with different shades of grey. The scanning electron microscope that

has been used to analyze the tungsten films contains several detectors additionally to such a secondary electron detector, enabling also other microstructure analysis techniques (see subsection 7.1.3 and subsection 7.1.2). The volume of excitation, where the secondary electrons originate from is strongly dependent on the primary electron energy as well as the sample density. Following [80] the penetration depth in tungsten can be estimated as ~ 460 nm for an acceleration voltage of 20 kV of the primary electron beam. But since the mean free path of the low energy secondary electrons is only a few nanometers, the SEM only resolves the sample surface.

Figure 7.1 shows the SEM image of a tungsten film. Immediately eye catching is the contrast between featureless areas and areas of a sublime lamellar structure. These areas typically extend over a few hundred nanometers. This kind of surface morphology is only typical right after deposition. It dissolves over the period of a few months.

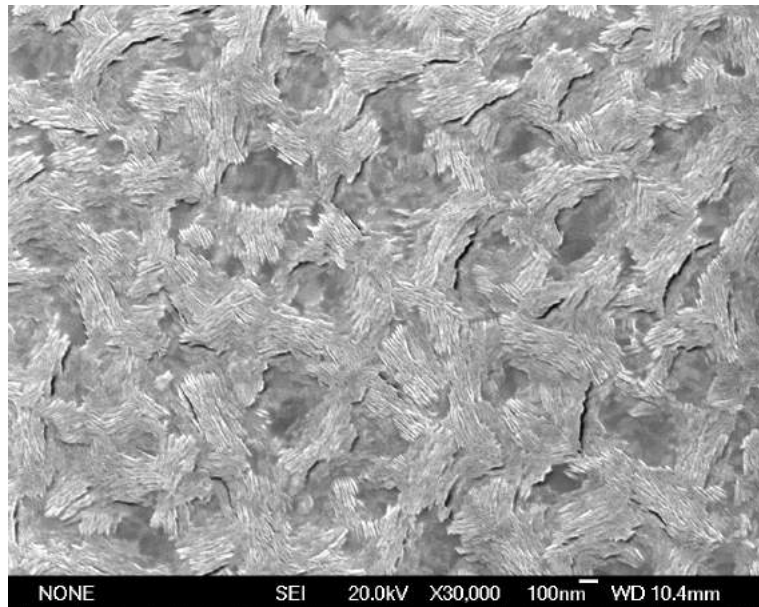


Figure 7.1: SEM image of a tungsten film.

A similar morphology has been observed by L. Maille, C. Sant and P. Garnier [81]. High resolution SEM revealed, that in the investigated films the lamellar structures sometimes go all the way through the whole thickness of the film. Grazing Incidence X-Ray Diffraction (GIXRD) analysis also done by this group showed, that their films favored a 0 1 1 orientation with increasing thickness. Since also the lamellae covered more area with increasing thickness, they suggested the lamellae to correspond to the 0 1 1 orientation. This hypothesis is also supported by the investigations of H. Y. Xu et al. [82]. After exposing tungsten samples to a high flux of low energy deuterium plasma, the surface showed three different kinds of nanostructures,

7.1 Microstructure Analysis

each corresponding to a specific orientation. While on grains with a $0\ 0\ 1$ and $1\ 1\ 1$ orientation spongy and triangular structures were observed, all grains that were fairly close to a $0\ 1\ 1$ orientation showed lamellar like morphologies. Having this in mind it stands to reason to assign the observed lamellar structures to the $0\ 1\ 1$ oriented crystal phase.

Comparison of films of the same batch could not reveal any differences in surface structure for the different spots in the substrate mask. Also films of different thickness, that were produced in the same deposition process didn't show significant changes in surface structure, as long as the thickness exceeded a few ten nanometers.

Part of the work for this thesis has been done at Stanford university in the context of detector research and development for the SuperCDMS experiment. As described in chapter 3, the SuperCDMS phonon channel will be read out by TES as well. The big surface area of the 10 cm diameter detectors requires high uniformity of the tungsten film, which is why sputtering was the deposition technique chosen. However, sputtering is not the optimal technique when it comes to low transition temperature tungsten films. To yield a uniform T_c of less than 45 mK over the whole crystal in a 40 nm thin sputtered film is one of the main challenges in the detector fabrication. Instead of heating, the SuperCDMS collaboration is using tungsten targets with an iron content of several parts per million to tune down the T_c .

Figure 7.2 shows SEM images of a 40 nm thin tungsten film, sputter deposited at Stanford university on a 4 inch silicon wafer. The first three images (left to right and top to bottom) were taken from three different spots of one wafer, that correspond to a T_c of about 74.5 mK, 66 mK and 59 mK (there might be a positive temperature offset on these values of 10 - 20 mK). The gray shades of the first three images were turned into black and white, with the threshold in the middle of the gray scale. While the difference in surface morphology between the two upper images is rather small, the image that corresponds to the lowest T_c shows a more distinct morphology. This shows that a nonuniform T_c can indeed be reflected in a nonuniform surface morphology. Images that were taken at other magnifications showed the same trend. The fourth image shows the same area as the third one (the one with the lowest T_c) at much higher magnification (x 130,000). In contrast to the other areas of higher T_c , this area shows a lamellar structure as well, however, on a much less distinct level.

Combining the surface morphology uniformity of film batches that were deposited in Tübingen with the fact that T_c non-uniformity was reflected in surface morphology non-uniformity as observed in Stanford, is a very promising result when it comes to T_c uniformity across the substrate mask.

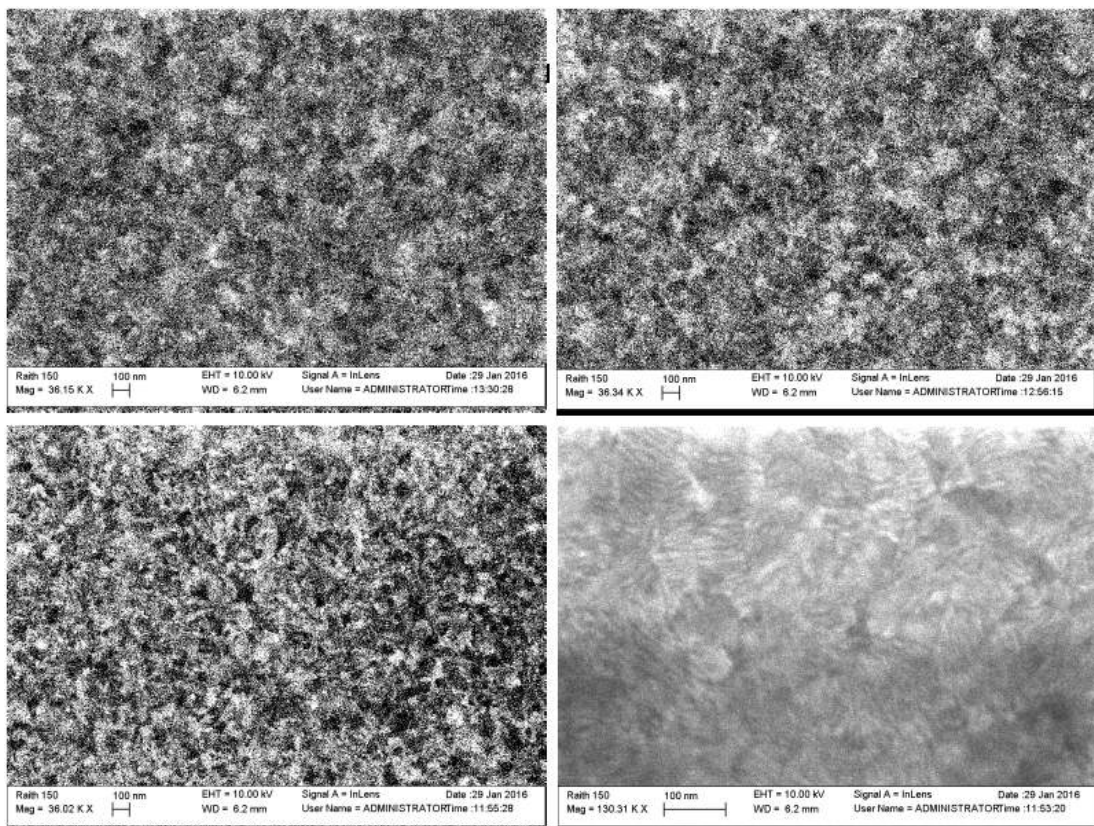


Figure 7.2: SEM images of a 40 nm thin sputtered tungsten film with nonuniform T_c . The images correspond from left to right and top down to T_c values of 74.5 mK, 66 mK, 59 mK and again 59 mK with a magnification of 130,000 instead of 36,000.

7.1.2 Crystal Structure Mapping

Apart from secondary electrons, backscattering of the primary electrons of a SEM beam leads to another radiation component. The backscattering occurs in the strong electric fields of the atoms and is therefore strongly dependent on the electron density within the sample. Since electrons have a limited mean free path of only few ten nanometers, backscattered electrons are only informative about the top nanometers of the sample surface. They can not only be used to map the surface for materials of differing electron density, but also for mapping of crystal phase distributions and their orientations, by taking advantage of diffraction patterns in the backscattered electron stream, that are characteristic to the crystal structures of the penetrated top layer. These so called Kikuchi bands are being visualized on a phosphor screen, and finally detected by a CCD chip. To select backscattered electrons for detection from secondary electrons, the sample is usually tilted by $\sim 70^\circ$ with respect to the electron beam. The detector has an angle of 90° to the beam and 20° to the sample surface normal, respectively (see figure 7.3). This analysis technique is usually referred to as electron backscatter diffraction (EBSD).

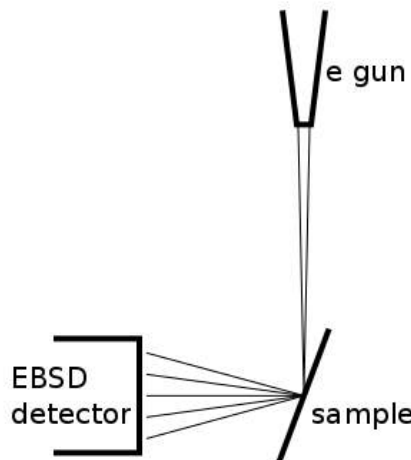


Figure 7.3: Geometrical setup for EBSD analysis.

Because of the extreme angle of the sample towards the SEM beam, drifting of the beam is a major issue for EBSD mapping and since the mapping is quite time consuming the beam focus needs to be very stable over time. Charging effects in non conductive materials like carbon from split up carbon hydrogen chains can disturb the electron beam, enforcing the rejection of EBSD maps. Unfortunately the rejection rate is very high, making EBSD mapping even more time consuming. Furthermore, oxidation of the tungsten films allows EBSD analysis only right after deposition. Therefore, only few usable EBSD maps of tungsten films exist and this

technique is not suited for the analysis of large numbers of films. However, the EBSD analysis led to a better understanding of the film microstructure.

Figure 7.4 shows a SEM image of a tungsten film (top left) and the same image overlayed with an EBSD map of the same area (top right). The colors represent different α -tungsten crystal orientations. Even though the SEM image is of poor quality, it is clearly visible, that all darker, featureless areas coincide with grains of α -tungsten, but also some slat covered areas show this crystal phase. The bottom left image shows the spatial distribution of α (yellow) and β -tungsten phase (pink). The bottom right image is a pole figure showing the orientation distribution function (ODF) for the α -phase with respect to the sample normal.

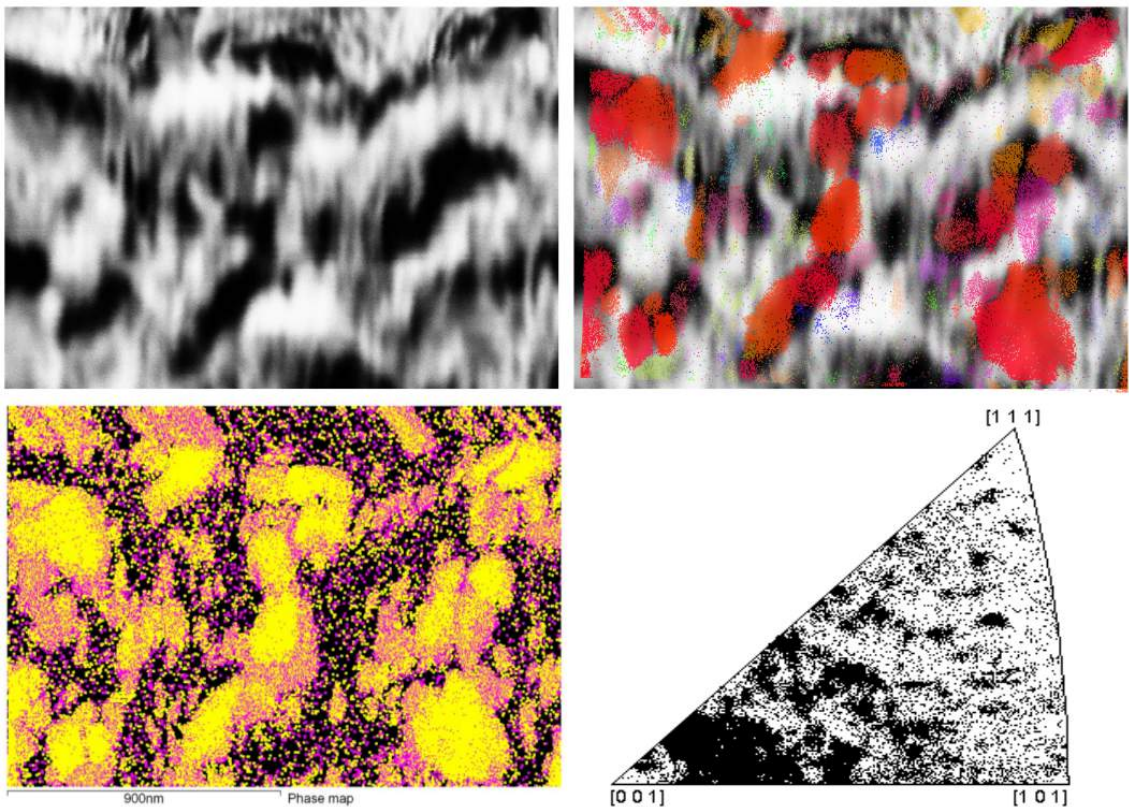


Figure 7.4: EBSD map of a tungsten film. The images at the top show a SEM image of a tungsten film surface (left) and again the same SEM image, overlayed with an EBSD α -tungsten map of the same area (right). The different colors represent different crystal orientations (red corresponds to 001). The α -tungsten tends to coincide with the featureless darker areas. The bottom left image shows α and β -tungsten of the same area in an EBSD phase map. While α -tungsten (yellow) grows in grains, the β -phase tungsten (pink) only shows an excess at α -grain boundaries. At the bottom right the α -phase orientation with respect to the sample normal is shown. The 001 orientation is represented strongest.

Unlike α -tungsten, the β -phase does not form grains, but is usually observed when the film grows in a columnar structure, so with a much bigger surface to volume ratio. That suggests the β -phase to preferably form at the surfaces of the microstructures and at the grain boundaries. In none of the EBSD maps the slats could be resolved. Due to their widths of only a few nanometers they might not make up big enough scattering centers for EBSD analysis. Moreover, they largely prevent EBSD mapping of the underlying tungsten. So the fact that at the bright white areas only little α -tungsten is found, is likely due to the coverage by the slats. The preferred occurrence of the 001 orientation in the EBSD map (see bottom right) at the first glance seems surprisingly, since energetic reasons favor the 011 oriented grains over the 001 orientation. However, the slats that prevent EBSD analysis on 011 oriented areas could explain the measured texture if they preferably grow on 011 surfaces. As further investigations confirm (see subsection 7.1.4), the slats indeed cover 011 oriented surfaces.

7.1.3 Atomic Composition

Energy dispersive x-ray spectroscopy (EDX) is an analysis technique for the characterization of a sample's elemental composition. The electron beam of a SEM generates x-rays within the sample. The characteristic spectrum of the outgoing x-rays is a fingerprint of the chemical composition. In contrast to wavelength dispersive spectrometry (WDS) that uses a crystal for better energy resolution, EDX provides better statistics by measuring the x-rays directly with a semiconductor detector. The detection limit depends on various things and is typically at a few per mille for elements of higher atomic number and $\sim 0.5\text{ - }1\%$ for elements in the first and second period of the periodic table.

Figure 7.5 shows the resulting spectrum of an EDX analysis of a tungsten film. The data had been analyzed with the INCA software of the electron microscope. The oxygen content seen in this analysis of about 2.8 atomic percent is likely to be the sum of oxygen within the sample and from the oxidation layer on the film surface. Depending on the electron acceleration voltage, also the SiO_2 layer covering the substrate can contribute to this spectrum, preventing the determination of the oxygen content within the film. The carbon line however is caused by a fairly known process of surface contamination by hydrocarbons. The vacuum of the microscope's process chamber is generated by a turbomolecular pump in combination with an oil lubricated backing pump, and the manipulator stick for sample transfer is lubricated with vacuum grease. Therefore, the residual gas is slightly contaminated with hydrocarbons that are absorbed on surfaces like that of the sample. Interactions with the electron beam causes the molecular chains to crack, liberating the hydrogen and leaving the carbon as surface contamination. This effect was verified by varying the measuring time at different surface spots. The carbon content increased with time and can even be seen with the SEM as darkening spot on the film surface. At an acceleration voltage of 20 kV also tantalum contaminations could be seen, that

most likely originated from the substrate mask. The spectra that were taken did not show any significant change with the beam being directed on featureless areas or on the lamellar like structures. The presence of oxygen, tantalum and carbon prevent the analysis of contaminations by these elements within the films. Apart from these three elements, the EDX was only sensitive to the tungsten and silicon and thus is not suited for impurity analysis.

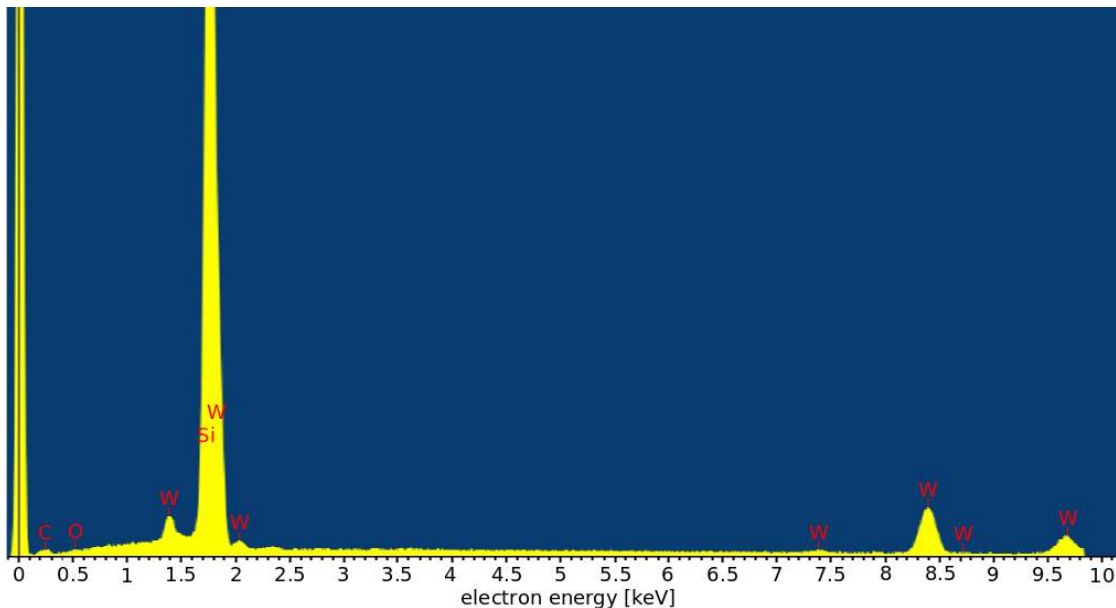


Figure 7.5: Typical EDX spectrum of a tungsten film. Apart from tungsten only oxygen, carbon and silicon could be detected. The silicon peak is caused by the substrate, whereas the carbon occurs as surface contamination (see text). Unfortunately EDX analysis can not be applied to quantitatively determine contamination by oxygen, because oxygen also shows up in the intermediate SiO_2 layer.

7.1.4 Microstructure

Similar to a SEM, also focused ion beams (FIB) can be used for surface structure imaging by taking advantage of secondary electrons. But apart from imaging an FIB can also be used for the ablation of sample material, as has been done for this work. Gallium ions were accelerated to 30 keV and focused onto the surface of tungsten films. Combined with the scanning abilities of the FIB, whole areas could be cleared off the top film layer. The depth of this layer is adjustable by the scanning speed.

Figure 7.6 shows a SEM image of a tungsten film, that has been treated by a FIB in such a way. For the resulting hilly landscape profile on the whole, three causes are

7.1 Microstructure Analysis

thinkable. One scenario could be, that already existing structures on the initial film surface were being enhanced by the FIB treatment. Ions that hit the flank of an existing structure are channeled downwards and would preferably ablate material in the 'valleys'. Also different material compositions or crystal structures that differ in their propensity of being sputtered could lead to such a profile. The profile could for instance reflect the distribution of α and β -tungsten within the film. A third cause could be a channeling effect that differentiates between crystal lattice orientations of the same phase. Geometrical considerations on the [001], [011], and [111] orientation of the bcc α tungsten structure suggest a hierarchy following

$$[011] > [001] > [111]$$

with the [011] orientation being the one with the biggest cross section for sputtering. M. T. Robinson and O. S. Oen simulated the channeling effect on bcc iron and fortified this consideration [83].

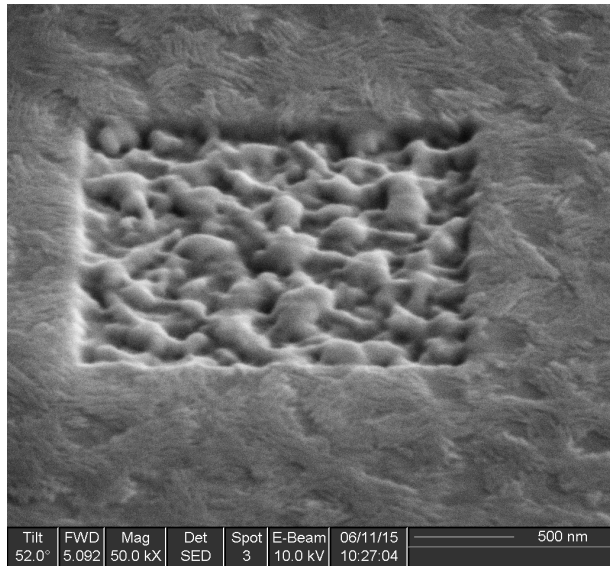


Figure 7.6: SEM image of a FIB treated tungsten film.

In the case of the analyzed tungsten films, amplification of the initial surface structure could clearly be ruled out as cause of the hilly profile. Figure 7.7 shows a series of images that were generated from two SEM images, taken before and after FIB ablation. The two images are overlayed and the opacity of the top image gradually increased. In between the picture taking, the electron beam drifted by a few ten nanometers. To compensate the drift, the images were aligned by eye. An easily recognizable structure pattern is e.g. the set of four lamellar free spots in the lower

left corner of the image (encircled in red), that shows the untreated film. All four of this spots result in sublime structures after the FIB treatment. However, the areas marked with red arrows, that are covered with fins, also results in an elevated structure. So it appears that the initial surface structure and the structure of a FIB treated film are correlated in size, though the latter is not an enhancement of the original height profile.

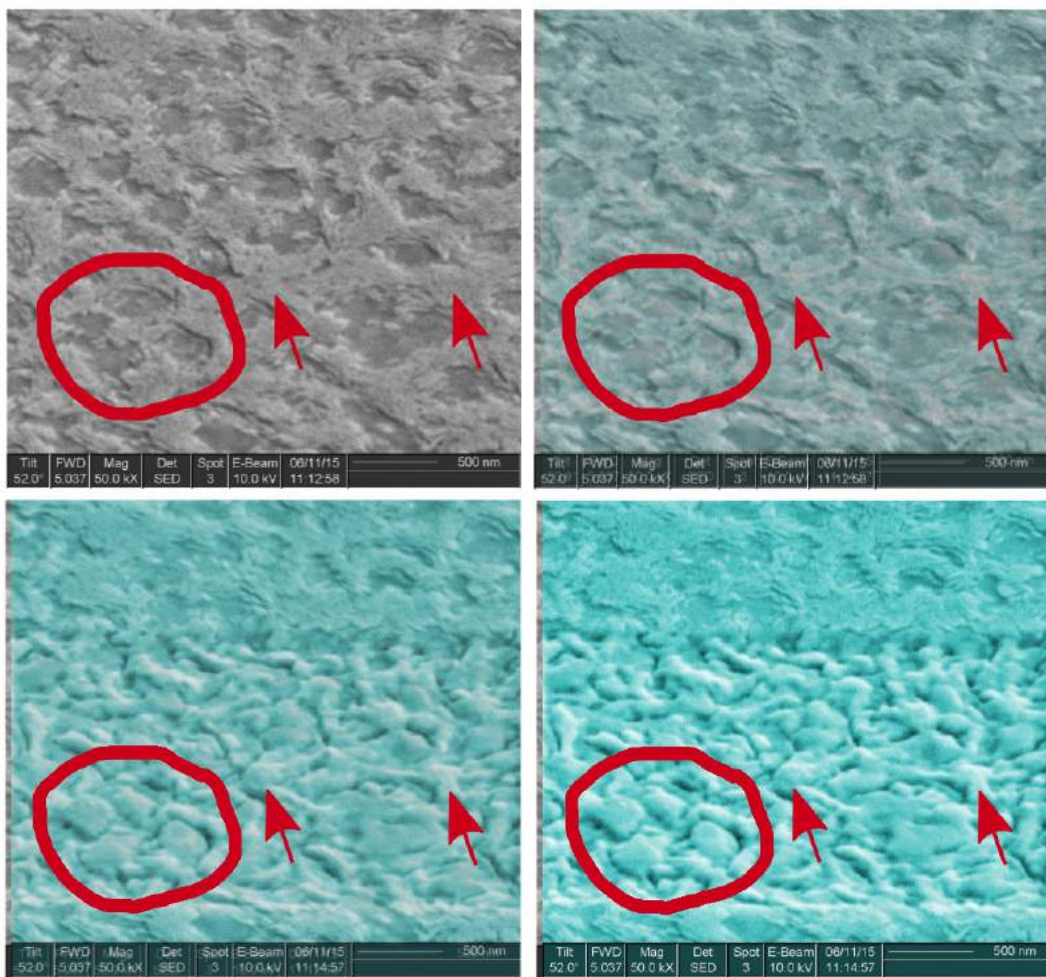


Figure 7.7: This series of images shows the correlation between the surface structure and the internal microstructure of a tungsten film. It is generated from two SEM images, taken before and after FIB ablation of the film surface layer. These images are overlayed and the opacity of the top image gradually increased from 0 to 100 %. The four encircled lamellar free spots in the lower left corner result in sublime structures after FIB treatment, as well as the areas, that are marked with arrows. Summarizing can be said, that the surface structure reflects the internal film structure in dimensions.

7.1 Microstructure Analysis

Channeling of gallium atoms as a significant cause for the hilly profile seams to be very unlikely. Comparison of FIB treated and untreated films showed no significant difference in crystal orientation. However, EBSD scans are very time consuming and unfortunately a large fraction of scans have to be rejected due to e.g. charging effects, that often lead to defocussing or drifting of the SEM beam. To completely rule out channeling of gallium atoms as contribution to the surface profile, higher statistics and thus more EBSD scans would be necessary.

EBSD analysis showed, that the resulting height profile reflects the internal film microstructure. Figure 7.8 shows SEM images of FIB treated areas (left) and the same images overlayed with color coded images of α -tungsten EBSD maps (right). They suggest the sublime structures to coincide with α grains of uniform crystal orientation. Shadowing effects and electrons, backscattered from the flanks facing the SEM beam that do not reach the EBSD detector, prevent the investigation of some areas. In particular the grain boundaries can seldom be resolved. Furthermore, it should be noted, that the FIB treatment is a destructive technique, that can partly destroy the crystal lattice and lead to point defects by implantation of gallium atoms. The fact that the “hills” in the FIB treated films correspond to α -tungsten grains means, that the regions in between the grains are more likely to be ablated and must differ in their structure.

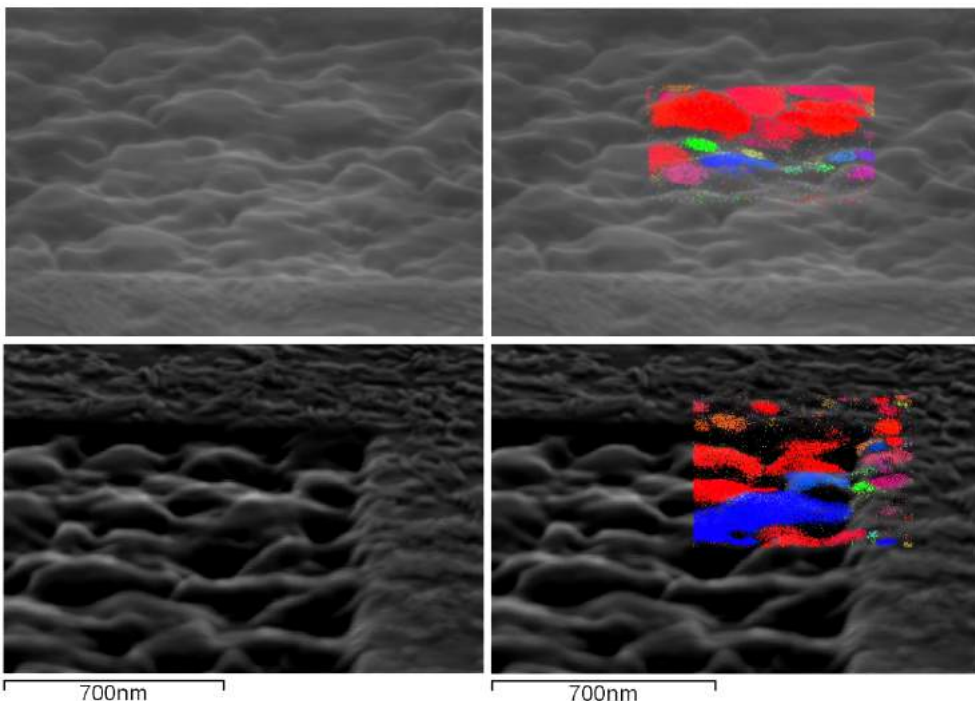


Figure 7.8: EBSD maps of FIB treated films. The different crystal orientations are color coded. The sublime structures coincide with areas of specific crystal orientation.

To get a better picture of how the α -tungsten grains extend along the film normal, a deep cut with a high intensity FIB beam was made (Figure 7.9). The absence of V-shaped grains suggests that competitive growth played a minor role, but coalescence and grain coarsening might have been determining factors for the microstructure (see also section 4.4). In the structure zone model the kind of texture shown in figure 7.9 is comparable to zone II, where grain boundary motion determines the texture evolution.

The FIB treated films had also been analyzed using EDX. Apart from the foreign carbon, oxygen and tantalum atoms, that had also been found in earlier measurements (see section 7.1.3), gallium atoms could be detected, that were implanted preferably in the flat top areas of sublime structures. The interpretation of this finding is, that in these areas the ions could not deposit their energy in an immediate single interaction, sputtering tungsten from the film, but slowly lost their energy by interactions with the crystal lattice potential, penetrating the film until they were being stopped and implanted. X-ray spectra taken from sublime and lower structures were also compared for the detected oxygen content, to investigate, whether oxygen preferably accumulates in grains or at their boundaries, but no significant evidence was found.

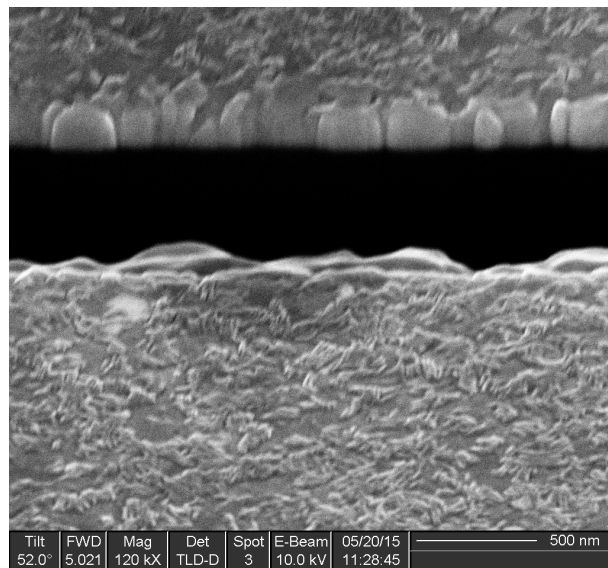


Figure 7.9: SEM image of a FIB cut into a tungsten film. The grains are clearly visible. The microstructure appears to be in agreement with zone II of the structure zone model developed by J. Thornton (see section 4.4).

7.1.5 Summary and Interpretation of the Microstructure Analysis

Using SEM analysis, two different types of surface morphologies were observed. Areas that are covered with lamellar like structures of locally preferred orientation alternate with rather featureless areas. EBSD analysis and FIB treatment confirmed that both structural types reflect the underlying microstructure, that consists of α -phase grains and β -tungsten at the grain boundaries. Comparison with the structure zone model (section 4.4) suggests the microstructure evolution to be dominated by grain boundary motion. The resulting grains range between 150 and 250 nm in diameter. The crystal structure of the slats could not be investigated using EBSD. They probably don't represent big enough scattering centers for the electrons. Looking at the surface morphology, the question arises, why these slats only grow on some areas, but avoid others. The work of L. Maille et al. [81] and H. Y. Xu et al. [82] suggest the slats to grow on all grains, that have an orientation fairly close to 011. The fact that EBSD analysis especially showed 001 oriented grains that are energetically disfavored in comparison to the 011 orientation is probably due to the slats, that prevent EBSD analysis of this areas. The dominant presence of 001 orientation compared to 111 is in agreement with energetic considerations.

The observed surface morphology does not show any variance over the film surface and also among the substrates of one batch no difference could be observed. Over time the lamellar structure gets more and more diffuse until it completely dissolves after a couple of months. Comparison of films, that were annealed after production and of those that were not, showed that annealing speeds up the temporal evolution. The impact of the film thickness onto the surface morphology is rather small. During film deposition a shutter was used to restrict the film growth on some of the substrates to a certain thickness. This way films of different thickness, produced under exactly the same conditions could be compared. No significant difference for film thicknesses that ranged from 120 to 250 nm could be observed. However, 20 nm and 30 nm films did not show any distinct features at all. Also an enhancement of the substrate temperature during deposition to over 600 °C results in featureless films. Smaller temperature changes between 450 and 500 °C do not result in recognizable differences.

7.2 Specific Resistivity

The specific resistivity of a thin metal film is determined by several effects. Distinction is made between the temperature dependent effect of electron-phonon scattering and non temperature dependent effects. Electron-phonon scattering typically has a linear dependence on temperature and freezes out at low temperatures, where only electron scattering on the surface, impurities, lattice defects and grain boundaries contributes to the resistance. When it comes to superconductivity, in particular impurity content and crystallinity are of interest, since these parameters not only determine the residual resistance, but also effect the phase transition temperature. The 'size effect' which means non specular scattering of electrons on the film surface that can lead to an increase of the film resistivity, plays a minor role as the following estimation shows and can thus be neglected as a source for an enhanced resistivity compared to the bulk value. The size effect is dependent on the film thickness d , which in this case is 200 nm and the electron mean free path l of about 20 nm [45]. Following E. H. Sondheimer et al. [84] the comparison of the specific resistance caused by the size effect to the bulk resistivity ρ_0 is given by

$$\rho_o/\rho = 1 - 3/8(1 - p)(l/d) \quad (7.1)$$

p is the fraction of electrons scattered specularly at the surface. The size effect will contribute to the film resistivity largest for $p = 0$, leading to a resistivity ratio of 0.9625 with respect to the bulk value of $\rho_0 = 5.3 \mu\Omega\text{cm}$. But, as can be derived from the measurements below, the ratio is always below 0.7. So even for $p = 0$ the size effect is not sufficient to account for a significant portion of the measured resistivity.

With the size effect being excluded, scattering on impurities, lattice defects and on grain boundaries are left as possible causes for an enhanced resistivity. A. F. Mayadas and M. Shatzkes concluded that in particular scattering on grain boundaries accounts for a major portion of the resistivity in polycrystalline films [85], leading to a resistivity ratio of

$$\rho_0/\rho_G = 1 - 3/2\gamma + 3\gamma^2 - 3\gamma^3 \ln(1 + 1/\gamma) \quad (7.2)$$

where ρ_0 is the intra grain resistivity, caused by scattering on point defects, electrons and phonons, and ρ_G as the film resistance under influence of electron scattering on grain boundaries. γ is given by

$$\gamma = \frac{l_0}{G} \frac{R}{1 - R} \quad (7.3)$$

with l_0 as the mean free path in single crystalline bulk material, G the average grain diameter and R as reflection coefficient at grain boundaries. In simulations of grain boundary scattering in metals Feldman et al. found, that both the change in crystal

7.2 Specific Resistivity

orientation in different grains, as well as disorder like impurities and vacancies in the boundary itself are the determinants of the reflectivity R [86]. Therefore, if the impurities are not exclusively situated next to the boundaries, ρ_0 and ρ_G can not be seen as independent contributions to the over all film resistance. Resistivity investigations in thin tungsten films confirm the findings of Mayadas and Shatzkes and suggest oxygen contaminations to preferably gather at grain boundaries and to be the primary determinant of grain boundary scattering in tungsten films [44]. Thus the low temperature residual resistance of tungsten films should be a good measure for crystallinity and oxygen content.

In films that are cooled down to below their transition temperature, point defects hold the potential of breaking up cooper pairs, leading to a shift or a broadening of the transition. Also the grain diameter is likely to influence superconductivity via the proximity effect. The residual specific resistance of a film is thus likely to be closely correlated with its superconductive properties. Research done at the University of Stanford support this consideration, as can be seen in the T_c vs. room temperature sheet resistance plot, shown in figure 7.10. The data points are scattered around a line, suggesting a linear relation. The relation seems to be material related and should be similar for the films deposited in Tübingen, in spite of different thicknesses (40 nm compared to 200 nm) and different deposition techniques.

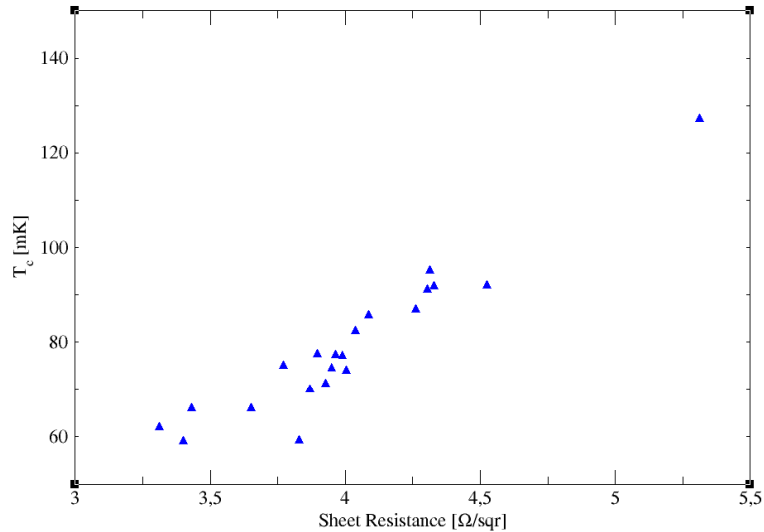


Figure 7.10: Transition temperature versus room temperature sheet resistance for sputter deposited 40 nm tungsten films. The plot suggests a linear dependence. Credit for this plot also goes to Betty Young, Matthew Cherry and Jeff Yen

The resistance measurements of the films from Tübingen were performed as follows. At first the films were equipped with four aluminum pads each to make wire bonding for four-point measurements easier. After bonding they were cooled down in

a can with liquid helium to a minimum temperature of 4.2 K. Two measurements for each film in different geometrical configurations enabled the specific resistance determination with the Van-der-Pauw method [87]. Figure 7.11 shows the temperature dependent specific resistance of a tungsten film. The low temperature regime below about 25 K, where the specific resistance becomes temperature independent, is of special interest. Since electron-phonon scattering is temperature dependent and surface scattering of electrons is also ruled out, in this regime the resistance is only influenced by scattering on grain boundaries and on lattice defects like impurities.

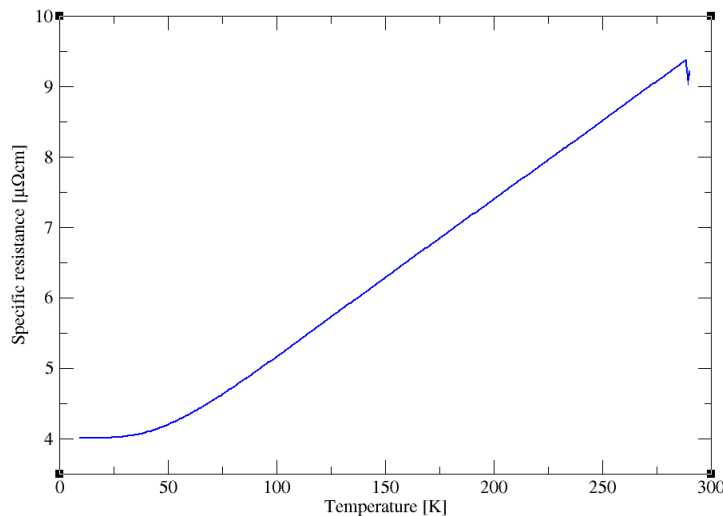


Figure 7.11: Specific resistance of a tungsten film in dependence of the temperature.
Credit: Lisa Tomm [88]

For most of the films only the values at room temperature and at liquid helium temperature were measured. Table 7.1 shows exemplarily for one of the film batches the specific resistance values at room temperature, 4.2 K and the RRR-value, which is the ratio of the first two. For materials with a resistivity at room temperature that is dominated by impurities and lattice defects, the RRR-value is close to one, while for phonon dominated room temperature resistances the RRR-value can be much higher. So the RRR-value is a simple measure for the cleanliness and crystallinity of a film. So a high RRR correlates with a low sheet resistance. In contrast to specific resistances measured with the van-der-Pauw method, the RRR-value is also independent from e.g. holes in the film, that could be caused from other analysis or bonding. From all films of the batch shown in table 7.1 the 150921_0 film differs the most in its values. It is the film from the middle position of the substrate mask. This is due to a different heat coupling. While all other films were coupled to the tantalum substrate mask with dummy silicon substrates, this film was stacked on a dummy tantalum substrate. Also, the plate of the mask that presses the films to the

backplate is only 0.5 mm thick and since the screws are located in the corners, the film in the middle might not be as well thermally connected to the heated backplate, as the others. This could easily be solved by exchanging this plate by a thicker one. Apart from this film, the others show only small differences. In the following the films from the middle position have not been taken into account.

film	$\varrho(300\text{ K}) [\mu\Omega\text{cm}]$	$\varrho(4.2\text{ K}) [\mu\Omega\text{cm}]$	RRR
150921_0	16.49	8.94	1.85
150921_1	12.77	5.95	2.15
150921_2	12.32	5.95	2.15
150921_3	11.32	4.99	2.28
150921_4	11.56	5.24	2.21
150921_5	12.09	5.75	2.10
150921_6	12.60	5.90	2.13

Table 7.1: resistivity values of a tungsten film batch.

The grain size of the films is expected to grow with rising substrate temperature during deposition. The RRR-value as a measure for the crystallinity is thus expected to increase with higher deposition temperatures. Figure 7.12 shows the RRR-value over deposition temperature of several films. In this plot all films but those from the middle position of the mask and those of only few ten nanometers thickness were taken into account. So some differ in deposition rate, cooling and radiation shielding during deposition (water or liquid nitrogen), residual gas composition, annealing temperature... Nonetheless, they seem to scatter around a regression line, suggesting a linear dependence. Two film batches at about 570 °C and 580 °C deviate the most from this line. No clear reason for this deviation could be found in the deposition conditions. However, it is encouraging that all films of these batches are affected evenly. It suggests the deviation to be indeed due to the deposition conditions.

Because of a lack of transition measurements, unfortunately the RRR measurements could not be put into relation with the respective transition temperature. Only for the two films of which the transition was measured in Munich the transition temperatures (both at about 15 mK) are known. The resistance values are listed in table 7.2 together with the substrate temperatures during deposition.

While all resistance values and the transition temperature of the two films are pretty consistent, the substrate temperatures differ quite a lot, so the temperature is clearly not the only determining factor for the superconductive transition. The two films also differ slightly in their annealing temperature and the the residual gas pressure,

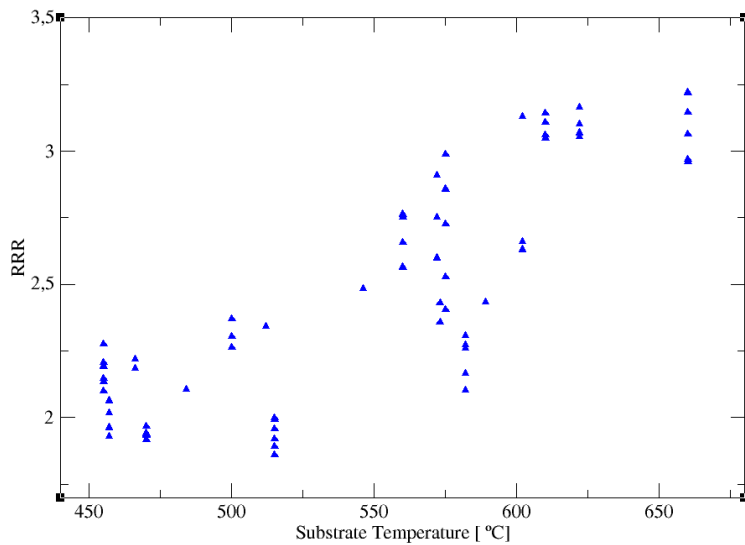


Figure 7.12: RRR-value versus substrate temperature. The data points suggest a linear relation.

but for a clearer picture of the dependencies, transition measurements of more films would be necessary. However, the consistency in both, the resistance values and T_c of the two films is very promising with respect of pretesting the films at room temperature and 4.2 K. With the assumption of the RRR-value to correlate with $1/T_c$, the T_c will correlate with the the substrate temperature.

film	$\rho(300 \text{ K}) [\mu\Omega\text{cm}]$	$\rho(4.2 \text{ K}) [\mu\Omega\text{cm}]$	RRR	$T_s [\text{°C}]$
140527_6	10.512	4.370	2.406	575
140603_0	10.495	4.457	2.355	500

Table 7.2: Resistivity values of the two tungsten films with known superconductive transition at 15 mK.

Also a gradient in T_c along the substrate mask within one film batch is likely to be noticeable already above the transition temperature as the following suggests. Two four inch wafers with 40 nm tungsten films on, that were sputter deposited in Stanford by Matthew Cherry and showed a gradient in T_c across the wafer were also tested for their resistances. The values are listed in table 7.3.

The fact that the gradient is visible in T_c AND resistance values, is good news for the mass production of TES. The film batches could be checked for a possible T_c gradient by measuring the resistance values.

To look for a possible film thickness dependence of the RRR value, films of different thicknesses within one deposition process were produced in Tübingen, by using a

7.2 Specific Resistivity

Wafer V21	$R_s(300\text{ K}) [\Omega/\text{sqr}]$	$R_s(4.2\text{ K}) [\Omega/\text{sqr}]$	RRR	$T_c [\text{mK}]$
top	3.95	2.63	1.5	74.5
middle	3.65	2.15	1.66	66
bottom	3.4	1.87	1.82	59

Wafer V23	$R_s(300\text{ K}) [\Omega/\text{sqr}]$	$R_s(4.2\text{ K}) [\Omega/\text{sqr}]$	RRR	$T_c [\text{mK}]$
top	3.77	2.18	1.73	75
middle	3.43	1.89	1.81	66
bottom	3.31	1.79	1.85	62

Table 7.3: Resistance and T_c values on three different positions of two sputter deposited 40 nm thick, 4 inch diameter tungsten films. The gradient in T_c is also reflected in a gradient of the resistance values. Credit also goes to Betty Young, Matthew Cherry and Jeff Yen.

substrate shutter. Since these films grew under identical conditions, differences in the RRR-value can only be attributed to a difference in thickness. In five deposition processes besides the standard 200 nm films, films of 20 nm, 30 nm, 120 nm, 150 nm and 250 nm were produced. Only the 20 nm and 30 nm thick films showed a difference in their RRR-value to their “siblings”. Given the relation of T_c and RRR-value, films of lesser thickness might still have a T_c in the required range. However, more T_c measurements would be necessary to find out if also less thicker films than the 200 nm ones are suited for 15 - 20 mK TES. The advantage of a 100 nm thick TES e.g. would be a halved heat capacity and thus a doubled sensitivity. Of course the front end electronics would need to be adapted to such a change.

To summarize the outcome of this chapter, the electrical properties of tungsten films seem to be sensitive indicators for other film properties. Combining the information of the plots 7.10, 7.12 and table 7.3 leads to the assumption, that a change of the substrate temperature during deposition can be used to tune the resistance values. An undoubtfull relation between electrical properties and T_c then leads to the assumption that also the T_c is tunable by the substrate temperature and that the resistance values can be used as quick checkup for the T_c . The similar RRR values within the film batches are promising with respect to uniform T_c 's. The unchanged RRR values for different film thicknesses down to 120 nm suggest the investigation of thinner tungsten films with less heat capacity as basis for the TES.

7.3 Strain Determination Using X-ray Diffraction

X-ray diffraction (XRD) is a powerful non destructive analysis technique for identification of crystal phases, investigation of their orientation and determination of their relative amount. XRD analysis is based on the wave character of x-rays. A monochromatic x-ray beam, directed onto a crystalline sample will be diffracted under certain angles, determined by constructive interference after reflection on the crystal structure. Figure 7.13 depicts the geometry of Bragg reflection. Constructive interference occurs, when a multiplicity of the wavelength matches the path difference of x-ray beams, reflected at different crystal planes. Mathematically the diffraction maxima follow the Bragg equation given by

$$n\lambda = 2d_{hkl} \sin(\theta) \quad (7.4)$$

with λ as the x-ray wavelength, the distance d_{hkl} between lattice planes of a certain orientation, the angle θ of the incoming beam to the sample surface and n as the multiplicity of the different maxima.

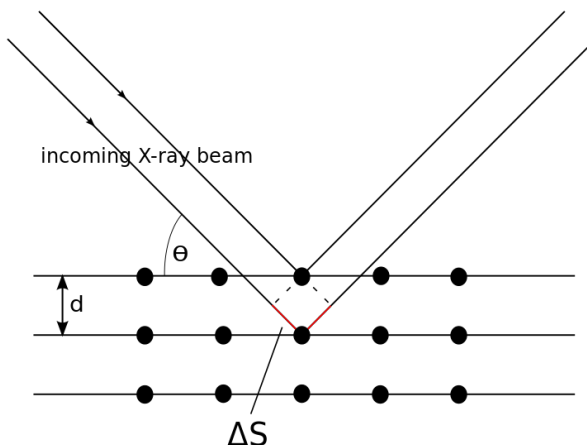


Figure 7.13: Geometrical configuration for XRD analysis. Diffraction will only occur, if the path difference ΔS of two beams, scattered at neighboring crystal planes, is equal to a multiplicity of the wave length.

Two diffractometers have been used for this work, since one of the instruments was down most of the time. Depending on the optics they were either using the 1.54059 \AA wavelength copper $K_{\alpha 1}$ line or both, $K_{\alpha 1}$ and $K_{\alpha 2}$ (1.54442 \AA). The weighted center of this double line is at 1.54187 \AA [89]. Both XRD's have optics for a parallel beam. X-ray optics and detector are always located on the surface of a circle, that surrounds the sample (Bragg-Brentano geometry). The $\theta = 0$ angle can

either be aligned with the film surface or the lattice of the single crystalline silicon substrate, that might slightly differ in orientation. For all measurements shown here, the $\theta = 0$ angle has been aligned with the film surface.

In table 7.4 the expected peak positions for an unstressed film of tungsten α and β -phase are listed. They are calculated from the α -tungsten lattice constant (see section 4.2), for $K_{\alpha 1}$ radiation only.

hkl	011	002	112	022	013	222	123
α peak position [°]	20.149	29.153	36.628	43.545	50.375	57.538	65.694
hkl	002	012	112	222	023	123	004
β peak position [°]	17.777	19.959	21.958	31.925	33.394	34.832	37.634

Table 7.4: XRD θ peak positions of tungsten α (top) and β (bottom) phase in unstressed tungsten. These values are calculated from the individual lattice constants (see chapter 4).

Figure 7.14 shows exemplarily the XRD θ -scan of a tungsten film. Comparison with table 7.4 reveals, that apart from the silicon substrate peak at about 35° all peaks represent the α -tungsten phase in different orientations and no sign for β -tungsten is present. In reality β -tungsten also contributes to the film composition, as can be investigated by e.g. EBSD analysis. However, to show up in an XRD scan, the β -tungsten micro volumes within the film would need to spread over a few ten nanometers in diameter. Otherwise the crystal phase is referred to as x-ray amorphous. As the EBSD film analysis showed in section 7.1.2, β -tungsten preferably grows at the boundaries of α -tungsten grains and does not form grains. Therefore, in this case XRD analysis appears to be unsuited for tungsten crystal phase composition investigations.

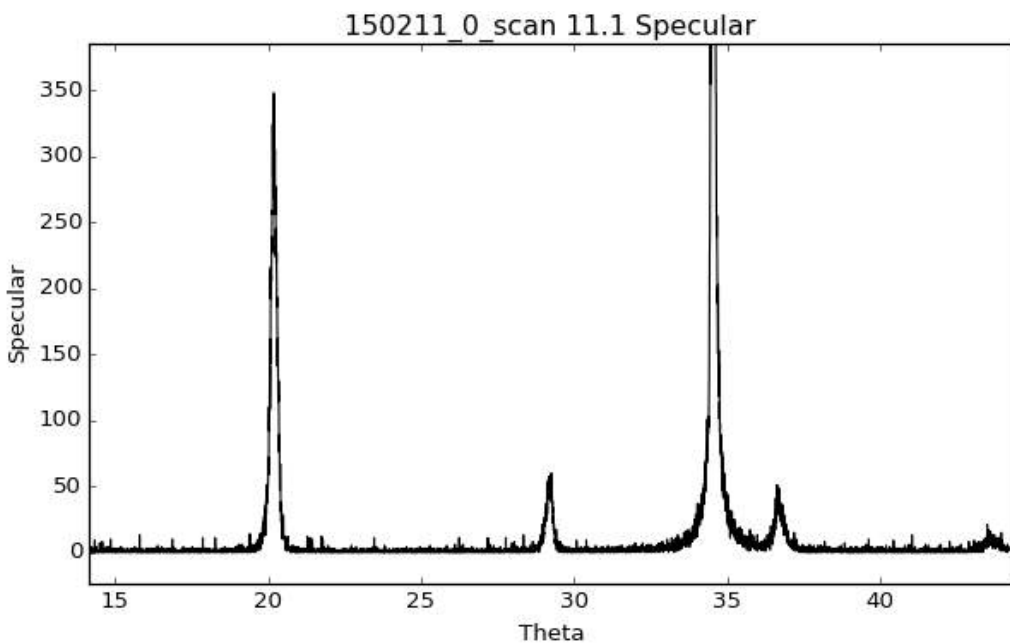


Figure 7.14: Typical XRD θ -scan of a tungsten film. Apart from the silicon substrate peak at about 35° only the α -tungsten phase is detectable.

Basics of Elasticity Theory

This short subsection will very briefly introduce some basics on the relation of stress and strain in elastic materials and the $\sin^2(\psi)$ measuring method.

Neighboring areas within a solid body usually are interacting via atomic forces that, in case of a crystal lattice, can lead to deformations of the latter. These interaction forces are described by the term “stress” while the relative deformation ϵ is referred to as “strain”.

$$\epsilon = \frac{(d - d_0)}{d_0} \quad (7.5)$$

With d and d_0 as a distance in the analyzed material in its strained and unstrained state. In general the stress for an infinitesimal volume segment in 3-D has to be written as σ_{ij} with $i, j \in [1, 2, 3]$. The indices describe the orientation of the segments surface and the direction of the force. Usually the notation is chosen that way, that a σ_{ij} with $i = j$ is the force per surface area perpendicular to the surface. In the case of non existing shear stress $\sigma_{ij} = 0$ if $i \neq j$. The notation for the strain tensor ϵ_{ij} is the same. ϵ_{ii} describes deformations perpendicular to the segments surface while ϵ_{ij} with $i \neq j$ represents shear strain. The relation between stress and

strain is given by Hooke's law:

$$\sigma_{ij} = c_{ijkl}\epsilon_{kl} \quad (7.6)$$

where c_{ijkl} is the stiffness tensor. All elastic materials, that are put under axial stress, react by deformations not only in the direction of the stress, but also perpendicular to it. This behavior is described by the Poisson's ratio ν . It is the ratio of the axial and the lateral deformation in the case of a one dimensional stress state.

$$\nu = -\frac{\epsilon_{lateral}}{\epsilon_{axial}}. \quad (7.7)$$

A direct measurement of the Poisson's ratio in polycrystalline thin tungsten films by Renault et al. revealed a value of 0.26, close to that (0.284) of bulk tungsten [90].

In the case of biaxial stress as it is typical for thin films, where the material is free to deform along the film normal towards its stress free state, stress in the film plane will lead to a deformation perpendicular to it. Figure 7.15 depicts how an elastic film will compensate tensile stress. Compared to the unstressed state (left) lattice planes that lie in the film plane will reduce their distances, while planes perpendicular to the film plane get a higher lattice constant (right). Lattice planes that have a certain angle (ψ) towards the film plane won't change their lattice constant. So clearly the position of a Bragg-peak measured by an XRD will depend on the orientation of the lattice plane within the film.

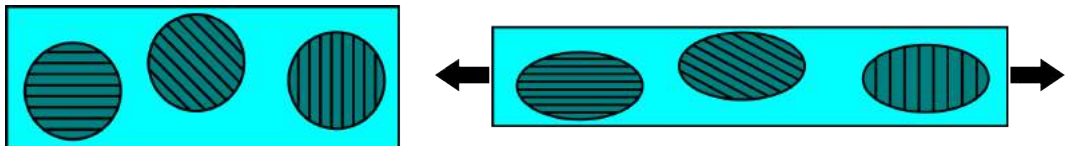


Figure 7.15: Illustration of the effect of tensile film stress on lattice planes of different orientation. left: no stress, right: tensile film stress in the direction of the arrows.

In order to select a certain lattice plane orientation within the film for XRD analysis, the sample can be tilted by an angle ψ relative to the tube-detector-configuration (see figure 7.16). For biaxial film stress ($\sigma_x = \sigma_y, \sigma_z = 0$) the strain component ϵ_ψ measured with a sample tilt ψ will have the following form:

$$\epsilon_\psi = \left(\frac{1 + \nu}{1 - \nu} \cdot \sin^2(\psi) + \frac{2\nu}{\nu - 1} \right) \cdot \epsilon_x. \quad (7.8)$$

where $\epsilon_x = \epsilon_y$ is the strain component within the film plane. Due to the linear dependence of ϵ_ψ and $\sin^2(\psi)$ this stress analysis method is usually referred to as $\sin^2(\psi)$ -method. It allows the independent determination of ϵ_x and ν from slope and ϵ_ψ -axis intercept of the regression line for the measured ϵ_ψ in dependence of $\sin^2(\psi)$.

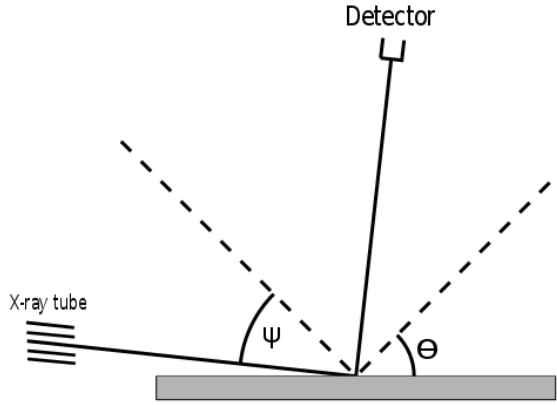


Figure 7.16: Geometry for $\sin^2(\psi)$ stress analysis. If the film is tilted with respect to detector and x-ray tube by an angle ψ , only lattice planes that are symmetrical in the detector-tube-configuration will contribute to the diffracted beam. This way lattice spacings of different orientations can be analyzed.

The Measurement

The main difference between the two XRD's used is the possible scanning range. Since one of them is only capable of up to $\theta = 45^\circ$ angles, this XRD is restricted to $\sin^2(\psi)$ scans of the $0\bar{1}1$ peak. This peak enables only sample tilts up to 20° . Furthermore, the Bragg-peaks of small θ angles are most sensitive to the shape of the substrate and to a misalignment of the z-coordinate. Therefore, lattice planes with higher miller indices are best suited for the $\sin^2(\psi)$ -method. This led to the decision to limit the analysis on the XRD that is capable of scanning the peaks with higher indices and on the $hkl = 123$ peak.

Figure 7.17 shows exemplarily the ϵ_ψ strain component over $\sin^2(\psi)$ for one of the films, measured by XRD scans. This and more plots can be found in [88]. It confirms the linear dependence. Due to geometrical reasons, the sample could not be tilted equally far in both directions.

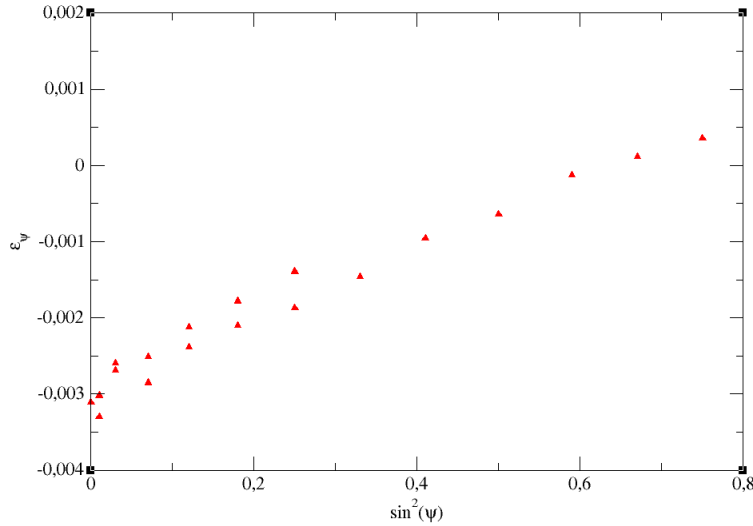


Figure 7.17: ϵ_ψ versus $\sin^2(\psi)$ plot of film 131029_0. The data points show a linear dependence as expected from equation 7.8 [88].

Using equation 7.8, the strain component in the film plane ϵ_x and the poisson ratio ν can be extracted from slope and y-axis intercept. Table 7.5 lists the ϵ_x and ν values for the analyzed films. As the positive slope shows, all films are under tensile stress.

film	ϵ_x	ν
130906_0	0.00169	0.427
131029_0	0.00170	0.462
140702_0	0.00053	1.347
150211_0	0.00112	0.519
150820_0	0.00074	0.229
150825_0	0.00184	0.429
150921_0	0.00095	0.541

Table 7.5: Uncorrected ϵ_x and ν values derived from $\sin^2(\psi)$ analysis of the 123 Bragg-peak.

Comparison of the poisson ratios with that of bulk tungsten ($\nu = 0.284$) or as observed in thin films ($\nu = 0.26$) [90] shows quite a discrepancy and questions the results for the ϵ_x values. That this discrepancy is due to a de-adjustment of the XRD will be shown by the following.

Assuming that the tube is not perfectly directed onto the center of the focus circle but misses it by a distance r , the x-ray beam will always be a tangent to a circle with radius r , if the tube moves on the focus circle (see figure 7.18). The first step of every XRD scan is the sample alignment. The detector will be put into the direct

beam path and the sample will be oriented parallel to the beam and moved half ways into the beam. The according positions of tube and detector will be set as zero. If the beam does not perfectly hit the focus circle center, already at this point there will be an offset on the θ angle, as depicted in figure 7.18 in an exaggerated way. In addition, the beam path will be changed during the $\sin^2(\psi)$ scan, leading to a systematic ψ dependent error $\Delta\theta$ of the 2θ angle.

The θ offset for a focus circle radius of 320 mm, as it is the case in he used XRD, and a defocus circle radius of 1 mm measures 0.179049° . The ψ dependent error $\Delta\theta$ has been calculated for 10 different sample tilts and again 1 mm defocus. The results are plotted in figure 7.19 and fitted with a polynomial of third order.

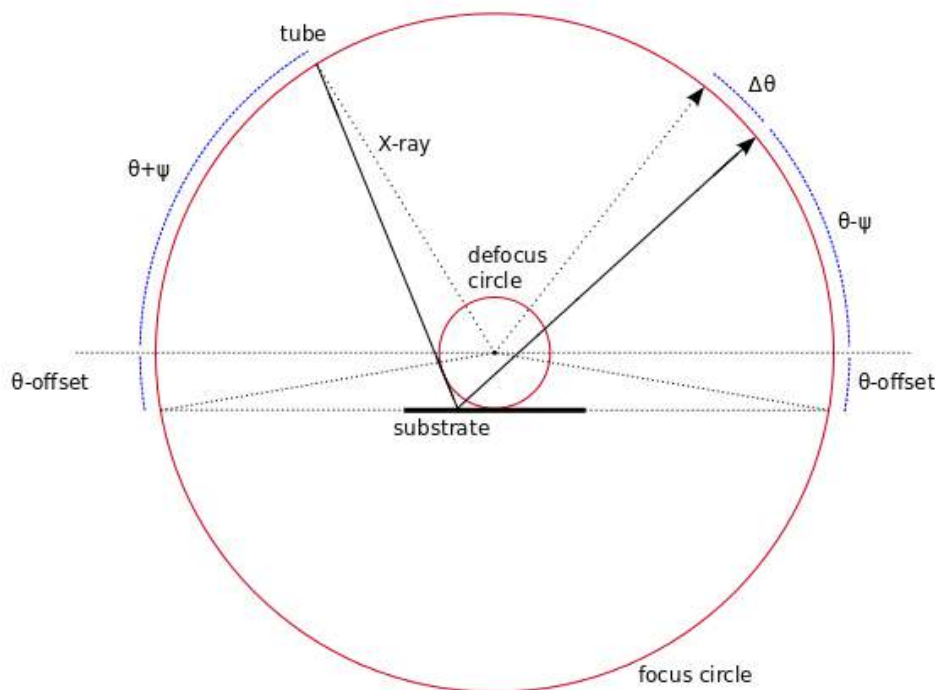


Figure 7.18: XRD defocus. If the beam misses the center of the focus circle, a θ -offset and a ψ dependent error on the 2θ will distort the results.

The polynomial and the θ offset have been used to correct the measured data under the assumption of a defocus of 1 mm in the direction as depicted in figure 7.18. The data of film 131029_0 before and after correction are plotted in figure 7.20. The regression line of the corrected data became slightly steeper and is shifted upwards. Also, the data became more symmetrical with regard to $\psi = 0$. The values for

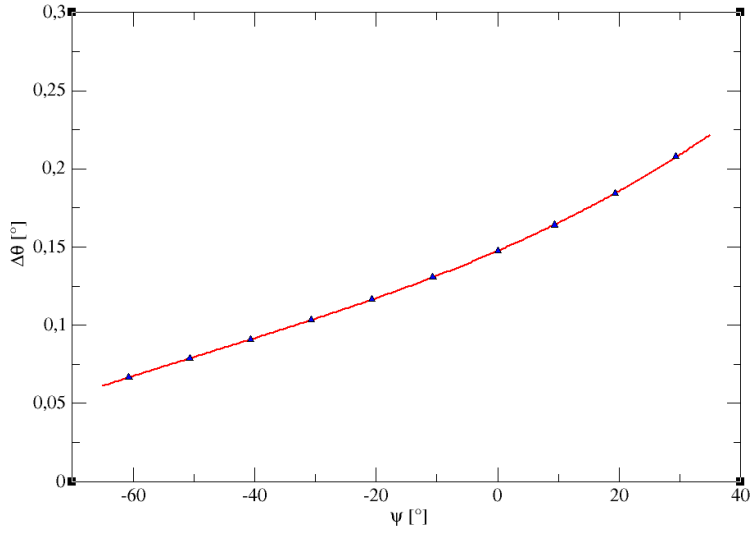


Figure 7.19: ψ dependent error on 2θ due to a XRD defocus of 1 mm as depicted in figure 7.18.

ϵ_x and ν calculated from the corrected values are listed in table 7.6. The yielded poisson ratios are now in the range of the expectation or a bit below, suggesting the XRD to be defocused by a bit less than 1 mm in the direction as depicted in figure 7.18.

film	corrected ϵ_x	corrected ν
130906_0	0.00291	0.239
131029_0	0.00291	0.278
140702_0	0.00172	0.280
150211_0	0.00233	0.269
150820_0	0.00194	0.222
150825_0	0.00306	0.253
150921_0	0.00215	0.263

Table 7.6: Corrected ϵ_x and ν values derived from $\sin^2(\psi)$ analysis of the 1 2 3 Bragg-peak.

As described in section 4.3 there are possible intrinsic and extrinsic sources for film stress. Extrinsic film stress due to epitaxial growth can be excluded due to the intermediate layer of amorphous SiO₂.

To estimate stress contribution caused by a mismatch in heat expansion coefficients the contraction of both materials have been calculated between production temperature (~ 800 K) and room temperature (~ 300 K). For tungsten the thermal expansion

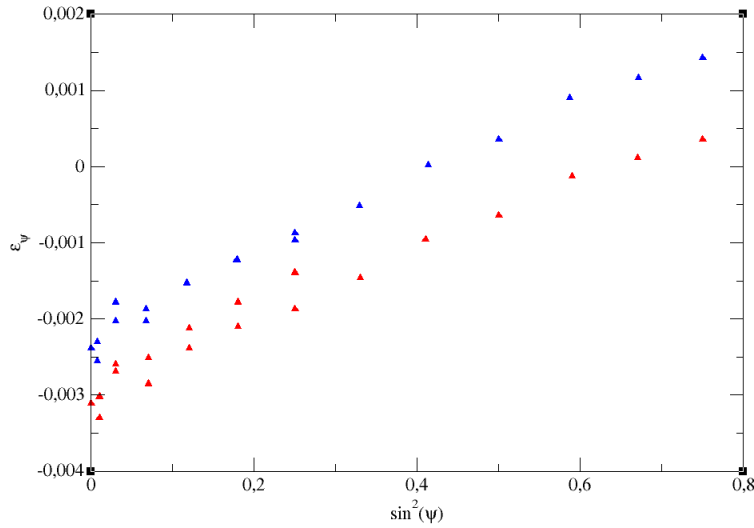


Figure 7.20: Corrected (blue) and uncorrected (red) $\sin^2(\psi)$ dependence of ϵ_ψ of film 131029_0.

coefficient at room temperature, reported by A. G. Worthing of $\alpha_W = 4.44 \cdot 10^{-6} \cdot K^{-1}$ has been applied [36], since it hardly changes over the temperature range. For the silicon contraction however, the the temperature dependent $\alpha_{Si}(T)$ reported by Y. Okada and Y. Tokumaru [91] has been integrated over the respective temperature range.

$$\epsilon_x = \alpha_W \cdot (800 K - 300 K) - \int_{300 K}^{800 K} \alpha_{Si}(T) \cdot dT \approx 0.000566 \quad (7.9)$$

$$\epsilon_{thz} = -\frac{2\nu}{1-\nu} \cdot \epsilon_x \approx 0.00044. \quad (7.10)$$

Comparison with table 7.6 reveals, that the differential thermal contraction accounts for only a few ten percent of the film strain. Thus extrinsic stress sources can be largely excluded, leaving intrinsic sources as cause for the film stress, like microstructure reformation processes.

To get a better idea of the origin of the film stress, figure 7.21 shows the ϵ_x strain component of the analyzed films in dependence of the substrate temperature T_s during film growth. Comparison with figure 4.1 in section 4.3 suggests the films to range around a stress maximum. As Haghiri-Gosnet et al. reported, this maximum to correspond to the transition between zone I and zone T in the structure zone model by Thornton. The stress originates from inter granular forces that tend to close voids in between the grains. These voids are likely to originate from decaying β -phase tungsten towards the α -phase. With growing temperature, the voids become smaller and the inter granular forces stronger until they reach a maximum value where the voids are completely closed. From there on an enhancement of the grain

size will lead to a fast decrease of the tensile stress until it turns compressive.

So the analysis of the $\sin^2(\psi)$ -method (see figure 7.21) gives an idea of the origin of the film stress and of the film microstructure. However, to confirm the findings, more $\sin^2(\psi)$ scans would be necessary, preferably with an adjusted XRD.

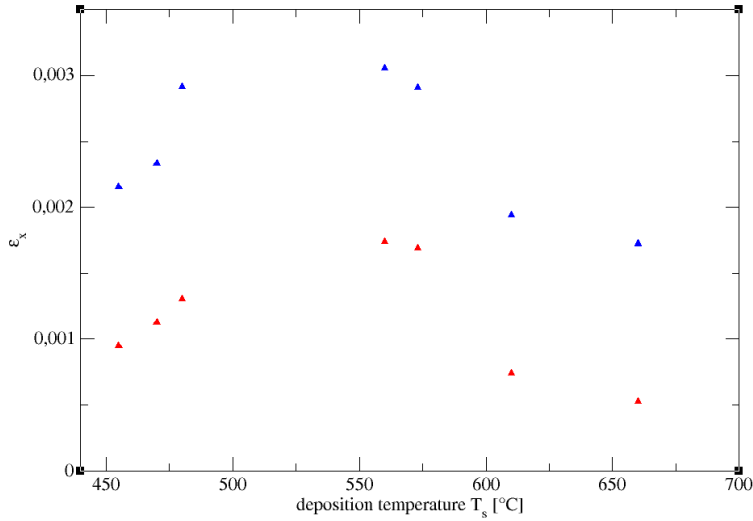


Figure 7.21: Corrected (blue) and uncorrected (red) T_s dependence of ϵ_x . The mathematical correction of the XRD-misalignment changes the measured strain quantitatively, but not the qualitative T_s dependence. Comparison with figure 4.1 in section 4.3 leads to the assumption that the stress originates from small voids in between grains, that tend to be closed by inter granular forces.

7.4 Annealing of Cold Deposited Films

For all the films that were deposited at elevated temperatures, the influence of annealing (at about 600°C) on the surface morphology was rather small. It seemed as if annealing speeds up the dissolving of the lamellar structure. However, higher statistics would be necessary to prove or disprove this. Films that were not heated during production on the other hand showed a dramatic change, when annealed at about 800°C. Figure 7.22 shows SEM images of two films before (left) and after (right) annealing. These films are from the same batch and were annealed in nitrogen atmosphere (top) and vacuum (bottom). Please note the different magnifications! Already before annealing there is a slight difference visible. The texture of the later in nitrogen annealed film looks more coarse than that of the other one. However, the difference in texture after annealing is much more obvious. In both films the grains are clearly visible, but while the vacuum annealed film shows grains of ~ 100 nm size, some grains of the other one even exceed one micron and images taken under an angle of 70° revealed, that from the edge to the middle of the grains, their height increases by several hundred nanometers. Since the initial film thickness was only 200 nm, the grains are probably barely touching each other. Both films also show voids in between some grains, so in spite of the big grains, the resistances can not be expected to be very low. In fact resistance measurements listed in table 7.7 and 7.8 show high resistances before annealing and even higher resistances afterwards. For the in nitrogen annealed film the resistance was not even measurable at 4.2 K any more. Annealing clearly has a massive impact on the film microstructure. In addition to heating during film deposition and if well dosed it might be suited to fine tune the film microstructure after deposition.

film 160418_0	before	after
$\rho(300 \text{ K}) [\mu\Omega\text{cm}]$	61.4	12820
$\rho(4.2 \text{ K}) [\mu\Omega\text{cm}]$	50.7	N.A.
RRR	1.21	N.A.

Table 7.7: Resistance values before and after annealing in nitrogen.

film 160418_0	before	after
$\rho(300 \text{ K}) [\mu\Omega\text{cm}]$	65.5	101.5
$\rho(4.2 \text{ K}) [\mu\Omega\text{cm}]$	54.3	81.9
RRR	1.20	1.24

Table 7.8: Resistance values before and after annealing in vacuum.

7.4 Annealing of Cold Deposited Films

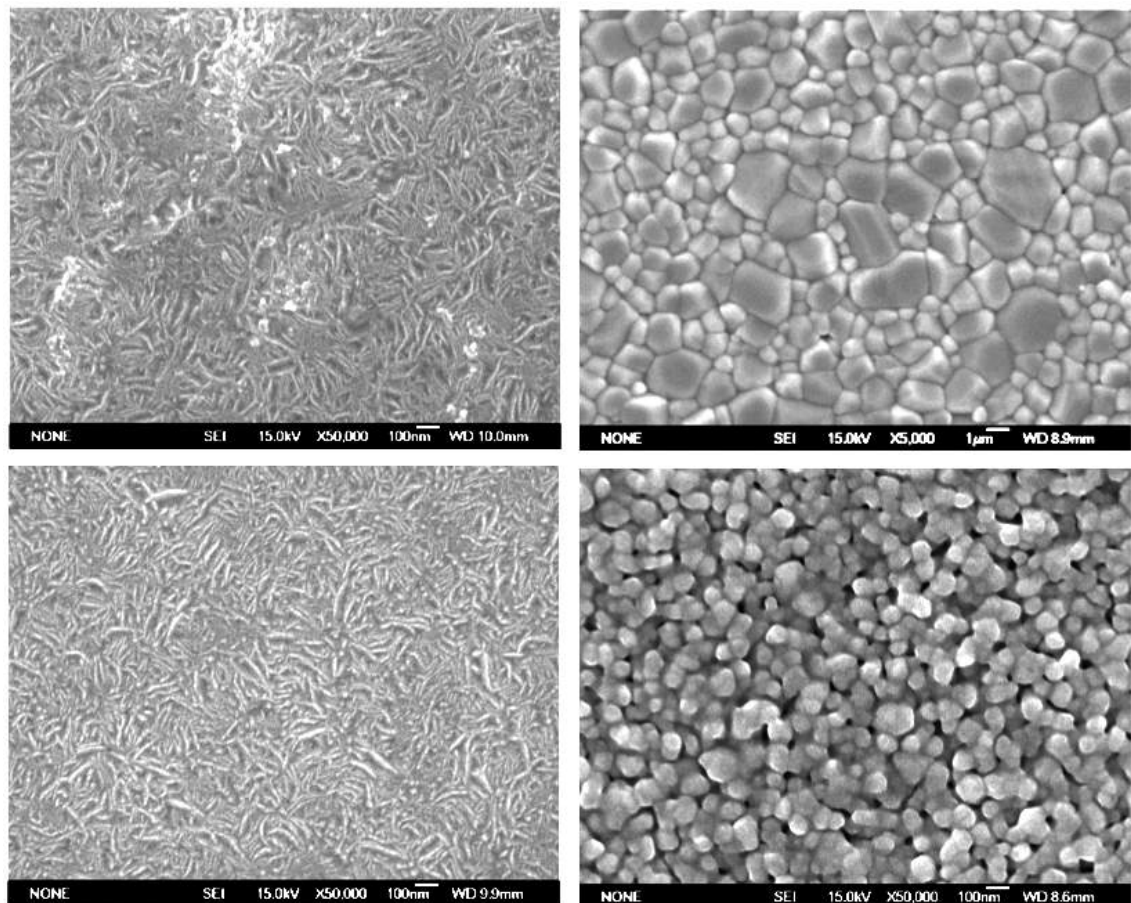


Figure 7.22: Cold deposited films before (left) and after annealing at about 800°C (right) in nitrogen atmosphere (top) and vacuum (bottom). In both cases the change is dramatic. Please note the different magnifications! While the top right image has a magnification of 5,000, the others are magnified by a factor of 50,000. In spite of (nearly) the same temperature, the annealing in nitrogen and vacuum led to quite different results.

8 Summary

The central goal of this thesis was to set up a deposition system, capable of growing thin tungsten films, suited for deployment in CRESST detector modules. That requires most of all a superconductive transition temperature (T_c) close to the bulk value of 15 mK. However, this is hard to realize in thin films. Another requirement was the production rate of TES. To enable a possible future upgrade, potentially within a joined effort of the dark matter community called EURECA, the current production rate needs to be sped up. Thus the system should be capable of producing hundreds of TES within years. Also the reproducibility of film properties is an issue in order to yield a high proportion of suited TES.

A deposition system has been set up and successfully put into operation. It consists of an ultra high vacuum system, equipped with an electron beam evaporation gun, a substrate heater, a residual gas analyzer and a liquid nitrogen cooling system. In order to account for a high TES production rate, a load lock chamber enables quick exchanges of substrates and serves to maintain stable vacuum conditions. The system proved to be capable of growing tungsten films with 15 mK T_c . A three inch area is available to grow multiple films at the same time. The precise number of TES that can be grown in one step, strongly depends on shape and size of the used substrates. The substrate holding structure can easily be exchanged or adapted to changing requirements.

Unfortunately the reproducibility of 15 mK T_c could not be tested within this thesis, due to a lack of reliable transition measurements. Difficulties with a cryogenic cooling system that is necessary to test the films at sub Kelvin temperatures, prevented the corresponding studies. Instead analysis of other film parameters have been performed to get a better understanding of deposition condition influences on film properties and their reproducibility. Analysis of the film microstructure revealed a surface morphology of lamellar type that could be attributed to the 011 crystal orientation. Changes of the deposition temperature showed little influence on the surface morphology. The grain size of 150 - 250 nm is not affected by thickness variations in the range of about 100 nm. The thickness variations also didn't affect the film resistance, suggesting a reduction of the film thickness, that would reduce the heat capacity and result in more sensitive TES's. However, also the T_c would need to remain unchanged in order to allow the thickness reduction. A linear dependence of deposition temperature and residual resistance ratio as well as the T_c could be shown. Strain investigations revealed that the film stress is mainly of intrinsic origin and caused by structure reformation processes. It was shown that

resistance values, film strain and the substrate temperature during deposition all correlate with each other and with T_c .

For future R&D projects I would suggest to further investigate the findings that a higher substrate temperature causes a higher RRR-value and a lower T_c and that the substrate temperature T_s correlates with the film strain ϵ_ψ and thus T_c correlates with ϵ_ψ . Then T_s is a tuning parameter for the T_c , and the RRR- and ϵ_ψ values can be used as quick checkup for the T_c . Additionally the correlation between film strain and microstructure would be interesting to further investigate. This all could help to not only tune the T_c , but also preselect films for measurements at sub Kelvin temperatures.

List of Figures

1.1	Rotation curve	2
1.2	Bullet cluster	3
1.3	Cosmic microwave background	5
1.4	CMB power spectrum	6
1.5	Calorimeter module	10
2.1	CRESST setup	12
2.2	CRESST detector module	13
2.3	Transition curve of a tungsten film	14
2.4	Thermodynamic model of a CRESST phonon detector	15
2.5	Scatter plot of a CRESST detector	18
2.6	Sketch of possible lead decay scenarios	19
2.7	Readout circuit for TES as used in CRESST	20
2.8	Status of the CRESST experiment	21
2.9	Scatter plot of the TUM40 CRESST detector	22
3.1	Quasiparticle Electrothermal feedback Transmission edge sensor (QET)	24
4.1	Film stress versus deposition temperature	31
4.2	Structure zone model	33
5.1	The UHV system for tungsten film deposition	37
5.2	The electron gun	39
5.3	CAD drawing of the film deposition system	40
5.4	Substrate temperature versus heater temperature	41
5.5	CAD drawing of the substrate mask	42
5.6	Comparison of film thickness variations	43
5.7	First version of a nitrogen cooling shield	44
5.8	Water operated cooling shield	45
5.9	Final version of the cooling shield	45
5.10	Typical partial pressure scan of the residual gas analyzer	48
6.1	Odd R(T) behavior of two tungsten films	54
6.2	Shadow mask for aluminum pad deposition	54
6.3	Etching rate of tungsten with an argon plasma source	55
6.4	Transition curve of film 140527_0	56
6.5	SEM images of aluminum on top of tungsten	57

7.1	SEM image of a tungsten film	59
7.2	SEM images of a tungsten film with nonuniform T_c	61
7.3	Geometry of EBSD analysis	62
7.4	EBSD map of a tungsten film surface	63
7.5	EDX spectrum of a tungsten film	65
7.6	FIB treated tungsten film	66
7.7	Correlation between surface and microstructure of a tungsten film	67
7.8	EBSD maps of FIB treated films	68
7.9	FIB cut into a tungsten film	69
7.10	Transition temperature versus sheet resistance	72
7.11	Specific resistance over temperature curve of a tungsten film	73
7.12	RRR versus Substrate Temperature	75
7.13	XRD	77
7.14	XRD scan of a tungsten film	79
7.15	Illustration of film stress	80
7.16	Geometry for $\sin^2(\psi)$ stress analysis	81
7.17	ϵ_ψ versus $\sin^2(\psi)$	82
7.18	XRD defocus	83
7.19	ψ dependent error on 2θ	84
7.20	Corrected ϵ_ψ versus $\sin^2(\psi)$	85
7.21	ϵ_x versus T_s	86
7.22	Cold deposited films, annealed at $\sim 800^\circ\text{C}$	88

List of Tables

7.1	Resistivity values of a tungsten film batch	74
7.2	Resistivity values of the tungsten films with superconductive transition	75
7.3	T _c and resistance gradient	76
7.4	XRD peaks of α and β -tungsten	78
7.5	Uncorrected ϵ_x and ν values	82
7.6	Corrected ϵ_x and ν values	84
7.7	Resistance change due to annealing in vacuum	87
7.8	Resistance change due to annealing in vacuum	87

Bibliography

- [1] Zwicky, F. Die Rotverschiebung von extragalaktischen Nebeln. *Helvetica Physica Acta*, 6:110127, 1933.
- [2] Faber S. M. and Gallagher J. S. Masses and mass-to-light ratios of galaxies. *Annual Reviews, Inc.*, 1979, 1979.
- [3] Ostriker J. P., Peebles P. J. E. and Yahil A. The Size and Mass of Galaxies, and the Mass of the Universe. *The Astrophysical Journal*, 193: L1-L4, 1974.
- [4] Roberts M. S. and Whitehurst R. N. The Rotation Curve and Geometry of M31 at Large Galactocentric Distances. *The Astrophysical Journal* 1975 vol. 201 p. 327, 1975.
- [5] Babcock, H. W. The Rotation of the Andromeda Nebula. *Lick Observatory Bulletin*, 19, pages 41–51, 1939.
- [6] Begeman K. G., Broeils A. H. and Sanders R. H. Extended rotation curves of spiral galaxies - Dark haloes and modified dynamics. *Monthly Notices of the Royal Astronomical Society (ISSN 0035-8711)*, vol. 249, April 1, 1991, p. 523-537., 1991.
- [7] Milgrom M. A modification of the Newtonian dynamics as a possible alternative to the hidden mass hypothesis. *Astrophysical Journal, Part 1 (ISSN 0004-637X)*, vol. 270, 1983.
- [8] Clowe D., Bradac M., Gonzalez A. H. et al. A Direct Empirical Proof of the Existence of Dark Matter. *The Astrophysical Journal Letters*, 648(2) L109, 2006.
- [9] Penzias A.A. and Wilson R. W. A Measurement of Excess Antenna Temperature at 4080 Mc/s. *Astrophysical Journal*, vol. 142, p.419-421, 1965.
- [10] Fixsen D. J. The Temperature of the Cosmic Microwave Background. *The Astrophysical Journal*, 707(2):916, 2009.
- [11] Planck Collaboration. Planck 2013 results. XVI. Cosmological parameters. *arXiv e-prints*, <http://arxiv.org/pdf/1303.5076v3.pdf>, 2013.
- [12] Ade, P. A. R. et al. (Planck Collaboration). Planck 2015 results. I. Overview of products and scientific results. 2015.

- [13] Bovy J. and Tremaine S. On the Local Dark Matter Density. *The Astrophysical Journal*, 756(1):89, 2012.
- [14] Lynden-Bell, D. Statistical mechanics of violent relaxation in stellar systems. *Monthly Notices of the Royal Astronomical Society*, Vol. 136, p.101, 1967.
- [15] Amr El-Zant, Isaac Shlosman and Yehuda Hoffman. Dark Halos: The Flattening of the Density Cusp by Dynamical Friction. *The Astrophysical Journal*, 560(2):636, 2001.
- [16] Christof Sailer. *Investigation of New Target Materials for Direct Dark Matter Detectors*. PhD thesis, 2014.
- [17] Markus Knapp. *Design, Simulation und Aufbau des GERDA-Myonvetos*. PhD thesis, 2009.
- [18] Angloher G., Bauer M., Bavykina I. et al. Commissioning run of the CRESST-II dark matter search. *Astroparticle Physics*, 31(4):270 – 276, 2009.
- [19] Angloher G., Bauer M., Bavykina I. et al. Results from 730 kgdays of the CRESST-II Dark Matter search. *The European Physical Journal C*, 72(4), 2012.
- [20] Pröbst F., Frank M., Cooper S. et al. Model for cryogenic particle detectors with superconducting phase transition thermometers. *Journal of Low Temperature Physics*, 100(1-2):69–104, 1995.
- [21] Raimund Strauß. *Energy-Dependent Quenching Factor Measurements of CaWO₄ Crystals at mK Temperatures and Detector Prototypes for Direct Dark Matter Search with CRESST*. PhD thesis, Max Planck Institute Munich, 2013.
- [22] Gluyas, M., Hughes F. D. and James, B. W. The elastic constants of calcium tungstate, 42-300 k. *Journal of Physics D: Applied Physics*, 6(17):2025, 1973.
- [23] Angloher G., Bento A., Bucci C. et al. Results on low mass WIMPs using an upgraded CRESST-II detector. *The European Physical Journal C*, 74(12), 2014.
- [24] Billard J. and Figueroa-Feliciano E. Implication of neutrino backgrounds on the reach of next generation dark matter direct detection experiments. *ArXiv e-prints*, arXiv:1307.5458, 2013.
- [25] Kuzniak M., Boulay M. G. and Pollmann T. Surface roughness interpretation of 730kg days CRESST-II results. *Astroparticle Physics*, 36(1):77 – 82, 2012.
- [26] Angloher G., Bento B., Bucci C. et al. Probing low WIMP masses with the next generation of CRESST detectors. *arXiv:1503.08065v1*, 2015.

Bibliography

- [27] Irwin K. D. *Phonon-Mediated Particle Detection Using Superconducting Tungsten Transition-Edge Sensors*. PhD thesis, Department of Physics, Stanford University, 1995.
- [28] Irwin K. D. An application of electrothermal feedback for high resolution cryogenic particle detection. *Applied Physics Letters*, 66(15), 1995.
- [29] Balakishiyeva D. et al. title= Brink P. L., Anderson A. J.
- [30] Jastram A. *CDMS Detector Fabrication Improvements And Low Energy Nuclear Recoil Measurements In Germanium*. PhD thesis, Department of Physics, Texas A and M University, 2015.
- [31] Yen J. *Phonon Sensor Dynamics For Cryogenic Dark Matter Search Experiment: A Study Of Quasiparticle Transport In Aluminum Coupled To Tungsten Transition Edge Sensors*. PhD thesis, Department of Physics, Stanford University, 2015.
- [32] Hammond, C. R. *The Elements*. 2004.
- [33] Waite T. R., Craig R. S. and Wallace W. E. Heat Capacity of Tungsten between 4 and 15 K. *Phys. Rev.*, 104:1240–1241, Dec 1956.
- [34] Rayne J. Specific Heats of Metals Below One Degree Absolute. *Phys. Rev.*, 95:1428–1434, Sep 1954.
- [35] Phillips N. E. Heat Capacity of Aluminum between 0.1 K and 4.0 K. *Phys. Rev.*, 114:676–685, May 1959.
- [36] Worthing A. G. The Thermal Expansion of Tungsten at Incan-Descent Temperatures. *Phys. Rev.*, 10:638–641, Dec 1917.
- [37] Lyon K. G., Salinger G. L., Swenson C. A. and White G. K. Linear thermal expansion measurements on silicon from 6 to 340 K. *Journal of Applied Physics*, 48(3), 1977.
- [38] Okada Y. and Tokumaru Y. Precise determination of lattice parameter and thermal expansion coefficient of silicon between 300 and 1500 K. *Journal of Applied Physics*, 56(2), 1984.
- [39] Corruccini R. J. and Gniewek J. J. Thermal Expansion of Technical Solids at Low Temperatures. *NBS Monograph 29*, 1961.
- [40] Lassner E. and Schubert W.-D. Tungsten - Properties, Chemistry, Technology of the Element, Alloys, and Chemical Compounds. 1999.
- [41] Bean, H. Material Properties and Analysis Techniques for Tungsten Thin Films. 1998.

- [42] Petroff P., Sheng T. T., Sinha A. K. et al. Microstructure, growth, resistivity, and stresses in thin tungsten films deposited by rf sputtering. *Journal of Applied Physics*, 44(6), 1973.
- [43] Rossnagel S. M., Noyan I. C. and Cabral C. Phase transformation of thin sputter-deposited tungsten films at room temperature. *Journal of Vacuum Science and Technology B*, 20(5), 2002.
- [44] Learn A. J. and Foster D. W. Resistivity, grain size, and impurity effects in chemically vapordeposited tungsten films. *Journal of Applied Physics*, 58(5), 1985.
- [45] Choi Dooho, Kim Chang Soo, Naveh Doron et al. Electron mean free path of tungsten and the electrical resistivity of epitaxial (110) tungsten films. *Phys. Rev. B*, 86:045432, Jul 2012.
- [46] Shen Y. G., Mai Y. W., Zhang Q. C. et al. Residual stress, microstructure, and structure of tungsten thin films deposited by magnetron sputtering. *Journal of Applied Physics*, 87(1), 2000.
- [47] Basavaiah S. and Pollack S. R. SUPERCONDUCTIVITY IN EVAPORATED TUNGSTEN FILMS. *Applied Physics Letters*, 12(8), 1968.
- [48] Shen Y. G., Mai Y. W. and McBride W. E. et al. Oxygen-induced amorphous structure of tungsten thin films. *Applied Physics Letters*, 75(15), 1999.
- [49] Weerasekera I. A., Shah S. I., Baxter D. V. and Unruh K. M. Structure and stability of sputter deposited betatungsten thin films. *Applied Physics Letters*, 64(24), 1994.
- [50] Moss R. L. and Woodward I. The structure of evaporated tungsten films. *Acta Crystallographica*, 12(3):255–256, Mar 1959.
- [51] Lita, A.E., Rosenberg, D., Nam, S. et al. Tuning of tungsten thin film superconducting transition temperature for fabrication of photon number resolving detectors. *Applied Superconductivity, IEEE Transactions on*, 15(2):3528–3531, June 2005.
- [52] Chopra, K. L., Randlett, M. R. and Duff, R. H. FACECENTEREDCUBIC TUNGSTEN FILMS OBTAINED BY. *Applied Physics Letters*, 9(11), 1966.
- [53] Chopra, K.L., Randlett, M.R. and Duff, R.H. FACE-CENTRED CUBIC MODIFICATION IN SPUTTERED FILMS OF TANTALUM, MOLYBDENUM, TUNGSTEN, RHENIUM, HAFNIUM, AND ZIRCONIUM. Jan 1967.
- [54] Basavaiah S. and Pollack S. R. Superconductivity in Tungsten Films. *Journal of Applied Physics*, 39(12), 1968.

Bibliography

- [55] Young B. A., Saab T., Cabrera B., Cross J. J. and Abusaidi, R. A. Tc tuning of tungsten transition edge sensors using iron implantation. *Nuclear Instruments and Methods in Physics Research Section A: Accelerators, Spectrometers, Detectors and Associated Equipment*, 444(12):296 – 299, 2000.
- [56] Young B. A., Saab T., Cabrera B., Cross J. J., Clarke R. M. and Abusaidi R. A. Measurement of Tc suppression in tungsten using magnetic impurities. *Journal of Applied Physics*, 86(12), 1999.
- [57] Kondo, Seiichi. Superconducting characteristics and the thermal stability of tungsten-based amorphous thin films. *Journal of Materials Research*, 7:853–860, 1992.
- [58] Chopra K. L. Enhancement of superconductivity in tungsten films. *Physics Letters A*, 25(6):451 – 452, 1967.
- [59] Lorenz, B. and Chu, C.W. In AnantV. Narlikar, editor, *Frontiers in Superconducting Materials*, pages 459–497. Springer Berlin Heidelberg, 2005.
- [60] Colling P., Nucciotti A., Seidel W. et al. Superconducting tungsten films for use as phase transition thermometers for calorimetric detectors. *Journal of Low Temperature Physics*, 93(3-4):549–554, 1993.
- [61] Mueller P., Ustinov A. V., Schmidt V. V. and Grigorjeva I. V. The Physics of Superconductors. *Springer*, 1997.
- [62] Kollar, J. Calculation of the Fermi velocity in tungsten. *Solid State Communications*, 27(12):1313 – 1316, 1978.
- [63] Maissel L. I. and Schaible P. M. Thin Films Deposited by Bias Sputtering. *Journal of Applied Physics*, 36(1), 1965.
- [64] W. Seidel. Superconducting Thin Film Thermometers For Calorimetric Particle Detectors. *12th International Vacuum Congress*, 1992.
- [65] Buckel W. and Kleiner R. *Superconductivity: Fundamentals and Applications*. Wiley, 2nd revised and enlarged edition edition, 2004.
- [66] Noyan I.C. and Shaw T.M. Inhomogeneous strain states in sputter deposited tungsten thin films. *Journal of Applied Physics*, 82(9), Nov 1997.
- [67] HaghiriGosnet A. M., Ladan F. R. and Mayeux C. et al. Stress and microstructure in tungsten sputtered thin films. *Journal of Vacuum Science and Technology A*, 7(4), 1989.
- [68] Barna P. B. and Adamik M. Fundamental structure forming phenomena of polycrystalline films and the structure zone models. *Thin Solid Films*, 317(12):27 – 33, 1998.

- [69] Petrov I., Barna P. B., Hultman L. and Greene J. E. Microstructural evolution during film growth. *Journal of Vacuum Science and Technology A*, 21(5), 2003.
- [70] Matthews J. W. Epitaxial Growth, Part B. *Materials Science Series*, 1975.
- [71] Thornton J. A. The microstructure of sputterdeposited coatings. *Journal of Vacuum Science and Technology A*, 4(6), 1986.
- [72] Marc Wüstrich. private communications.
- [73] Maille L., Sant C., Le Paven-Thivet C. et al. Structure and morphological study of nanometer W and {W₃O} thin films. *Thin Solid Films*, 428(12):237 – 241, 2003. Proceedings of Symposium J on Growth and Evolution of Ultrathin Films: Surface and Interface Geometric and Electronic Structure, of the E-MRS Spring Conference.
- [74] Arita M. and Nishida I. Tungsten Films with the A15 Structure. *Japanese Journal of Applied Physics*, 32:1759, April 1993.
- [75] *Handbook of Chemistry and Physics*. CRC Press Inc., 69th edition edition, 1988-1989.
- [76] Lu Chih-Shun and Lewis, Owen. Investigation of filmthickness determination by oscillating quartz resonators with large mass load. *Journal of Applied Physics*, 43(11), 1972.
- [77] Miller J. G. and Bolef D. I. Acoustic Wave Analysis of the Operation of QuartzCrystal FilmThickness Monitors. *Journal of Applied Physics*, 39(12), 1968.
- [78] Mueller R. M. and White W. Areal Densities of Stress Producing Films Measured by Quartz Crystal Microbalance. *Review of Scientific Instruments*, 40(12), 1969.
- [79] Igor Usherov. . PhD thesis, University of Tübingen, to be published.
- [80] Potts P. J. *A Handbook of Silicate Rock Analysis*. Blackie, 1992.
- [81] Maille L., Sant C. and Garnier P. A nanometer scale surface morphology study of W thin films. *Materials Science and Engineering: C* , 23(68):913 – 918, 2003. Current Trends in Nanoscience - From Materials to Application Proceedings of Symposium A, E-MRS Spring Meeting 2003,.
- [82] Xu H Y., Luo G. N. and Schut H. et al. Enhanced modification of tungsten surface by nanostructure formation during high flux deuterium plasma exposure. *Journal of Nuclear Materials*, 447(13):22 – 27, 2014.
- [83] Robinson Mark T. and Oen O. S. Computer Studies of the Slowing Down of Energetic Atoms in Crystals. *Phys. Rev.*, 132:2385–2398, Dec 1963.

-
- [84] Sondheimer E. H. The Mean Free Path of Electrons in Metals. *Advances in Physics*, vol. 1 No. 1, 1952.
 - [85] Mayadas A. F. and Shatzkes M. Electrical-Resistivity Model for Polycrystalline Films: the Case of Arbitrary Reflection at External Surfaces. *Phys. Rev. B*, 1:1382–1389, Feb 1970.
 - [86] Baruch Feldman, Seongjun Park, Michael Haverty et al. Simulation of grain boundary effects on electronic transport in metals, and detailed causes of scattering. *physica status solidi (b)*, 247, 2010.
 - [87] van der Pauw L. J. A method of measuring specific resistivity and hall effect of discs of arbitrary shape. *Philips Technical Review*, 20:220–224, 1958.
 - [88] Lisa Tomm. Studien an dünnen Filmen aus Germanium und Wolfram. Master's thesis, University of Tübingen, 2016.
 - [89] Spiess L., Teichert G., Schwarzer R. et al. *Moderne Röntgenbeugung: Röntgendiffraktometrie für Materialwissenschaftler, Physiker und Chemiker*. 2 edition, 2009.
 - [90] Renault P.-O., Badawi K. F., Bimbault L. et al. Poissons ratio measurement in tungsten thin films combining an x-ray diffractometer with in situ tensile tester. *Applied Physics Letters*, 73(14), 1998.
 - [91] Okada Y. and Tokumaru Y. Precise determination of lattice parameter and thermal expansion coefficient of silicon between 300 and 1500 K. *Journal of Applied Physics*, 56(2), 1984.

Danke!

Am Ende möchte ich mich noch bei den zahlreichen Unterstützern bedanken, die zu Gelingen dieser Arbeit beigetragen haben. Zuallererst ist dabei mein Doktorvater Professor Josef Jochum zu nennen, der mir diese Arbeit an diesem interessanten Projekt überhaupt erst ermöglicht hat. Ihm verdanke ich vor allem ausgezeichnete Arbeitsbedingungen in einem tollen Arbeitsumfeld, viel Freiheit in der Umsetzung der Ziele und immer ein offenes Ohr, wenn es um schwierige Entscheidungen oder schlicht eine zweite Meinung ging. Zweite Meinungen und ein offenes Ohr habe ich auch immer bei Markus Turad gefunden. Durch seine Erfahrung mit Vakuumtechnik und dünnen Filmen habe ich viel gelernt und seine Vorarbeit zur Vakuumanlage weiß ich sehr zu schätzen. Bedanken möchte ich mich auch bei der Feinmechanikerwerkstatt, die hier namentlich durch Norbert Stockmaier vertreten sein soll. Die lösungsorientierte und ideenreiche Zusammenarbeit war eine große Hilfe! Des Weiteren gehen Dank an Lisa Tomm für ihre Arbeit, Ronny Löffler und Christoph Back für ihre Hilfsbereitschaft, meine Tübinger CRESST-crew: Martin, Igor, Christian und Christoph für die Beantwortung von Fragen und fruchtbare Diskussionen. Die Arbeit wäre nicht möglich gewesen ohne einen großen Umfang an technischem Gerät. Hier bedanke ich mich bei allen Mitwirkenden des Lisa+ Centers und bei Professor Schreiber für die Zurverfügungstellung des XRDs. Gaby Behring, die mich stets gut gelaunt durch einen bürokratischen Hindernisparcour hindurch zu manövrieren wusste, Danke auch an Dich. Die Arbeit wurde vom BMBF finanziert denen ebenfalls Dank gebührt, wie auch dem DAAD für die Ermöglichung meines Stanford Aufenthalts. And last but not least, Thanks to the SuperCDMS members at Stanford University and SLAC for the opportunity to work with them and gain valuable experiences.